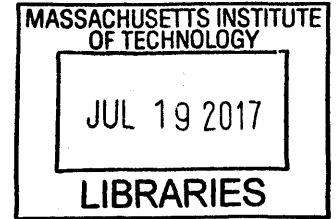


# Quantifying the Adhesion of Noble Metal Foulants on Structural Materials in a Molten Salt Reactor

by

Reid S. Tanaka

A.B. Biochemistry, 1981  
University of California, Berkeley



SUBMITTED TO THE DEPARTMENT OF NUCLEAR SCIENCE  
AND ENGINEERING  
IN PARTIAL FULFILLMENT OF THE REQUIREMENTS FOR THE DEGREE OF  
MASTER OF SCIENCE IN NUCLEAR SCIENCE AND ENGINEERING  
AT THE  
MASSACHUSETTS INSTITUTE OF TECHNOLOGY

ARCHIVES

FEBRUARY 2017

© 2017 Massachusetts Institute of Technology. All rights reserved

**Signature redacted**

Signature of the Author: \_\_\_\_\_

Reid S. Tanaka  
Department of Nuclear Science and Engineering  
January 17, 2017

**Signature redacted**

Certified by: \_\_\_\_\_

Michael P. Short  
Assistant Professor of Nuclear Science and Engineering  
Thesis Supervisor

**Signature redacted**

Certified by: \_\_\_\_\_

Michael R. Ames  
Research Scientist, MIT Nuclear Reactor Laboratory  
Thesis Reader

**Signature redacted**

Accepted by: \_\_\_\_\_

Ju Li  
Battelle Energy Alliance Professor of Nuclear Science and Engineering  
Professor of Materials Science and Engineering  
Chairman, Department Committee on Graduate Students

THIS PAGE INTENTIONALLY LEFT BLANK

# Quantifying the Adhesion of Noble Metal Foulants on Structural Materials in a Molten Salt Reactor

by

Reid S. Tanaka

Submitted to the Department of Nuclear Science and Engineering  
on January 17, 2017 in Partial Fulfillment of the  
requirements for the Degree of Master of Science in Nuclear Science and Engineering

## ABSTRACT

As discovered during the Molten Salt Reactor (MSR) Experiment (MSRE), selected fission products deposited on the wetted surfaces throughout the reactor. Fission products such as molybdenum and ruthenium are noble with respect to the electrochemical potential of the fluoride fuel salt and therefore remain insoluble in their elemental forms rather than becoming ionic salts. Coalescing in the primary fluid, these noble metals then migrate and eventually deposit on internal reactor surfaces. Since the bulk of these noble metal fission products are also energetically unstable they bring not only physical fouling, but heat and radiation from decay as well.

The adherence forces of five of the seven principal radioactive foulants discovered during the MSRE were measured on six different potential structural materials by atomic force microscope force spectroscopy (AFM-FS). The noble metals studied were niobium, molybdenum, ruthenium, antimony and tellurium. Structural materials measured were Hastelloy-N, the primary structural metal of the MSRE; two steels, SS316L and F91; commercially pure nickel and molybdenum; and silicon carbide. MSRs operate with surfaces free of passivating corrosion layers, so the measurements were conducted on bare metal surfaces. An argon ion gun chamber was constructed for removal of the oxide layers from mechanically polished substrate metals by sputtering. A combination vacuum chamber/glove box was crafted to accept the sputter polished substrates into a dry, inert environment where the force adhesion measurements were made.

Data acquired in the last phase of the study partially demonstrated the concept. The measured particle-to-substrate attractive forces found antimony and tellurium to be generally more adherent to the bare metals than niobium or molybdenum. The finding is consistent with the fouling examined in the MSRE. If held, this correlation of laboratory measurement to actual fouling may aid the reactor designer in anticipating fouling to plan for the effects. Such knowledge would inform selection of plant materials, both for operating components such as flow detectors and heat exchangers, where fission product deposition would be undesired, and for processing components such as filters and metal collection systems, where adhesion would be preferred.

Thesis Supervisor: Michael P. Short

Title: Assistant Professor of Nuclear Science and Engineering

THIS PAGE INTENTIONALLY LEFT BLANK

## Acknowledgments

This work was supported in full by a grant by Transatomic Power, Inc.

I am deeply indebted to Professor Mike Short who, with tremendous leadership, guided me through this fascinating new adventure. With incredible patience, he granted me a great degree of freedom in my studies, while always being available as a source of knowledge and needed direction.

I am particularly grateful to Dr. Michael Ames for being so gracious as to take on this academically needy student from outside of his department and grant his indispensable guidance and insight.

I would also like to thank my lab mates in the Mesoscale Nuclear Materials lab, still affectionately known as the Blue Lab. The youthful exuberance, energy and brilliance of Dr. Pengui Cao, Sara Ferry, Andrew Dykhuis, MiaoMiao Jin, Cody Dennett, Weiyue Zhou, Max Carlson, Sam McAlpine, Charlie Hirst, Rachel Connick and Natasha Skowronski made my return journey to academia a delightful experience and reinstilled my optimism for the future. I'd like to particularly recognize two of these lab mates: Weiyue Zhou for his on-going late-night philosophical, scientific and technical debates which kept me challenged and grounded; and Max Carlson for his intrepid work and wizardry with electronics and machine tools. Plainly speaking, without Weiyue's and Max's help, my experiment would not ever have been designed and assembled.

Special thanks must go to Professor Yota Takamura, an Assistant Professor from Tokyo Institute of Technology who is visiting the Moodera Research Group at MIT. At the sacrifice of time for his own work during the holidays, he responded to my request for help and made the three final sets of cantilever tips for me. Without his assistance, I would not have been able to take the critical data for this thesis.

I would also be remiss if I didn't recognize the continued sacrifice by my loving wife Mari. Without her extreme patience and unconditional support, I would not have been able to have experienced this intriguing and challenging journey at MIT.

THIS PAGE INTENTIONALLY LEFT BLANK

# Contents

<b>1</b>	<b>Motivation and Introduction</b>	<b>13</b>
<b>2</b>	<b>The Pathway to Fouling</b>	<b>19</b>
2.1	Fouling in Reactors . . . . .	19
2.1.1	Fouling in LWRs . . . . .	19
2.1.2	Fouling in an MSR . . . . .	20
2.2	Foulant Drivers . . . . .	23
2.2.1	Bubbles and Mist and Liquid-Gas Surface Transport . . . . .	23
2.2.2	Electrochemistry and Mass Transfer . . . . .	25
2.2.3	Observations on Noble Metals of Interest . . . . .	28
2.2.4	Dual Nature of Niobium . . . . .	30
2.3	Particle to Surface Forces . . . . .	31
2.3.1	Van der Waals Force at the Atomic/Molecular Level . . . . .	31
2.3.2	Quantum Electrodynamics Approach . . . . .	33
<b>3</b>	<b>Decay Heat and Mass - Impact of MSR Fouling</b>	<b>39</b>
3.1	Decay Heat Over Time . . . . .	40
3.2	Fission Products . . . . .	41
3.2.1	Noble Metal Fission Products . . . . .	42
3.3	Mass of Noble Metal Fission Products . . . . .	47
3.3.1	Fission Product Mass Estimates . . . . .	49
<b>4</b>	<b>Material Selection and Sample Preparation</b>	<b>53</b>
4.1	Selection of Materials for the Study . . . . .	53
4.1.1	Foulants - AFM Cantilever Tips . . . . .	53
4.1.2	Structural Material - AFM Substrates . . . . .	54
4.2	Cantilever Tip Preparation . . . . .	55
4.2.1	Specific AFM Cantilever Information . . . . .	56
<b>5</b>	<b>Experimental Setup</b>	<b>59</b>
5.1	Atomic Force Microscope (AFM) . . . . .	59
5.1.1	Basic AFM Operations - Force Measurement . . . . .	60
5.2	Initial Atomic Force Microscope (AFM) . . . . .	62
5.3	Design of a New Machine . . . . .	63
5.4	Main Chamber and the AFM . . . . .	64

5.4.1	Glove Operations and Vacuum . . . . .	65
5.5	Argon Ion Gun Chamber . . . . .	68
5.6	Gas Management . . . . .	70
5.7	Specific Additional Equipment of Note . . . . .	70
5.8	Operations . . . . .	71
5.9	ezAFM AQUA . . . . .	73
<b>6</b>	<b>Experimental Results and Conclusions</b>	<b>77</b>
6.1	Preliminary Measurements . . . . .	77
6.2	Chamber Data Collection and Results . . . . .	85
6.2.1	AFM Data . . . . .	86
6.2.2	Observations . . . . .	87
6.3	Individual Plots by noble metal tip type . . . . .	92
<b>7</b>	<b>Final Thoughts</b>	<b>99</b>
7.1	Future Investigations . . . . .	100
7.2	Future Use of the Chamber . . . . .	101
7.3	Positive Impacts of Noble Metal Fouling? . . . . .	101
7.4	Final Words . . . . .	102
<b>A</b>	<b>Molten Salt Reactor</b>	<b>103</b>
A.1	The Molten Salt Reactor Experiment . . . . .	103
A.1.1	Key Aspects of an MSR . . . . .	104
A.1.2	Physical Layout . . . . .	105
A.1.3	Gas Management . . . . .	107
A.2	Molten Salt . . . . .	107
A.2.1	Melting Point – Illustrative of Selection Criteria . . . . .	108
A.2.2	Typical Salt Elements . . . . .	109
A.2.3	Molten Salt Properties . . . . .	112
A.3	Molten Salt Sampling in the MSRE . . . . .	113
<b>B</b>	<b>Electrochemistry in an MSR</b>	<b>115</b>
B.1	Gibbs Free Energy of Fluoride Salts . . . . .	115
B.1.1	Gibbs Free Energy of Fluoride Salt Formation - Standard State	115
B.1.2	Gibbs Free Energy - Reactant Limited Condition . . . . .	116
B.1.3	FLiBe and UF <sub>4</sub> . . . . .	118
<b>C</b>	<b>Decay Heat Calculations</b>	<b>121</b>
C.1	Decay Heat Calculations at Power from a Clean Core Startup . . . . .	124
C.2	Decay Heat Following Shutdown . . . . .	129
C.3	Calculations for the Mass of Fission Products . . . . .	132
<b>D</b>	<b>Materials Under Study</b>	<b>135</b>
D.1	Fission Products and Structural Materials . . . . .	135
D.1.1	Niobium . . . . .	136
D.1.2	Molybdenum . . . . .	136



D.1.3	Ruthenium	136
D.1.4	Rhodium	137
D.1.5	Antimony (Sb)	137
D.1.6	Tellurium - Atomic Number 52	137
D.2	Material Data Sheets for Noble Metal Targets	138
D.3	Substrate Composition	139

# List of Figures

2.1	Gibbs free energy of formation of fluoride salts . . . . .	26
2.2	Temperature effects on equilibrium in a $UF_4/UF_3$ buffer . . . . .	28
2.3	Effect on force between particles due to coating . . . . .	36
3.1	Radioactivity of spent nuclear fuel . . . . .	41
3.2	Thermal Fission Yields . . . . .	42
3.3	Typical decay chain of fission products - $^{99}Sr$ to $^{99}Ru$ . . . . .	43
3.4	Decay heat from noble metals . . . . .	45
3.5	Decay heat from noble metals by beta particles . . . . .	46
3.6	Decay heat (beta) from noble metals following shutdown. . . . .	47
3.7	Mass build up of a radioactive isotope vs stable isotope . . . . .	49
3.8	Mass buildup of molybdenum . . . . .	49
4.1	Pre-sputtered AFM cantilever with 4 $\mu m$ diameter $SiO_2$ sphere attached. . . . .	57
4.2	A close-up view of a silica sphere mounted on a cantilever. . . . .	57
5.1	The basic AFM measurement concept . . . . .	60
5.2	Typical force curve from an AFM . . . . .	61
5.3	Typical force curve from the ezAFM . . . . .	62
5.4	An AFM alignment chip and the backside of a cantilever chip . . . . .	63
5.5	Photograph of the vacuum chamber in its as-found condition . . . . .	64
5.6	Photograph of the fit of the ezAFM in the vacuum chamber . . . . .	64
5.7	Cutaway view of the glove port . . . . .	66
5.8	Photograph of the finished glove port configuration. . . . .	67
5.9	Drawing of the main vacuum chamber / glove box . . . . .	67
5.10	Drawing of the argon ion chamber . . . . .	68
5.11	Photograph of the argon ion gun chamber . . . . .	69
5.12	A coupon and sputtered test sample on the AFM stage. . . . .	70
5.13	Photograph of pre- and post-sputtered F91 samples . . . . .	73
5.14	Multiple force curves . . . . .	76
6.1	Summary of Preliminary Data . . . . .	79
6.2	Two different cantilever ranges . . . . .	80
6.3	Dwell time influence on adhesion force. . . . .	81
6.4	Pre-sputtered (0.1 N/m) silicon nitride AFM cantilever with and without the molybdenum particle attached. . . . .	82

6.5	Graphic summary of the final data . . . . .	86
6.6	Histogram of a typical comparison of the original data and the data after removal of outliers . . . . .	87
6.7	Removal of outlier data skewed high and skewed low . . . . .	88
6.8	ezAFM screen shot of an unstable probe. . . . .	89
6.9	Exploratory runs: ruthenium tips on four substrates . . . . .	93
6.10	Exploratory runs: niobium tips on substrates . . . . .	94
6.11	Chamber runs: niobium tips on six substrates . . . . .	94
6.12	Exploratory runs: molybdenum tips on three substrates . . . . .	95
6.13	Chamber runs: molybdenum tips on six substrates . . . . .	95
6.14	Exploratory runs: tellurium tips on four substrates . . . . .	96
6.15	Chamber runs: tellurium tips on six substrates . . . . .	96
6.16	Chamber runs: antimony tips on six substrates . . . . .	97
6.17	Chamber runs: combined view of antimony and tellurium on six sub- strates . . . . .	98
A.1	The MSRE Layout . . . . .	104
A.2	MSRE cutaway view of the reactor cell and pump. . . . .	106
A.3	The phase diagram for LiF and BeF <sub>2</sub> . . . . .	108
A.4	Melting point diagram for the ternary mixture of LiF, BeF <sub>2</sub> and UF <sub>4</sub> . . . . .	109

# List of Tables

2.1	Distribution of fission products in molten salt reactors . . . . .	30
3.1	Mass of Fission Products per 1000 kg of $^{235}\text{U}$ . . . . .	51
4.1	Summary of noble metal cantilever tip preparation . . . . .	58
6.1	Mean and standard deviation for the preliminary phase with the MFP-3D AFM. . . . .	84
6.2	Mean and standard deviation for AFM measurements in the chamber.	92
A.1	The Mixture of Fuel Salt in the First MSRE Run . . . . .	111
B.1	Gibbs free energy of fluoride formation . . . . .	120
C.1	Noble Metal Half-Lives and Thermal Neutron Absorption Cross Sections	133
D.1	Important Isotopes of Key Fission Products and Structural Elements	135

# Part 1

## Motivation

The world's court of public opinion recoiled from nuclear power due to the tsunami driven reactor accident of 2011, just as the scientists studying the impact of atmospheric carbon were winning their hard fought case in the court of the same. Advocates of nuclear power point to the proven capability of high density electrical power with a minimal footprint in the fight against global warming. Opponents, taking advantage of the general public fear of nuclear, continue to push (and win) their case citing the exorbitant construction costs and the uncertainty of long-term waste storage. However, according to advocates of advanced nuclear reactor designs such as the molten salt reactor (MSR), this division need not exist. The MSR they say, is radically different because the fuel is a liquid molten salt and the meltdowns and hydrogen explosions vividly etched in our minds are not possible.<sup>1</sup> Such a reactor has had growing interest of late with new companies forging ahead with the concept and an acknowledgement by many central governments of an intent to move forward in developing the MSR.<sup>2</sup>

Despite the touted safety advantages, the MSR has its own set of challenges and issues to be addressed. Processing the fuel salt to maintain the appropriate fuel mixture and to remove fission products is a necessary function requiring an additional engineered system (or separate processing plant). Advantageous from the standpoint of better fuel consumption, such a system will have its own radioactive chemical waste streams. While major releases from the reactor might be directly avoided, critics point to the added risk of smaller yet consequential radioactive releases from processing. Tritium, a radioactive isotope of hydrogen formed as an undesirable byproduct from the activation of salt components such as lithium fluoride, is particularly difficult to contain. Capturing tritium to limit releases to within governmental regulations poses

---

<sup>1</sup>The concept of the MSR was developed at Oak Ridge National Laboratory in Oak Ridge, TN in the 1950s and 1960s, culminating in two actual test reactors built and operated. The advantages of the MSR are more fully explained in part A.

<sup>2</sup>Reactor start-up companies have been established in the US, Canada, the Czech Republic and Japan, and new governmental efforts have been started in China, Russia and in the European Union. The MSR was given a boost and positive attention when it was adopted as one of the six advanced technologies selected by the Generation IV International Forum (GIF) in December 2002 [1].

yet another processing hurdle.

Some of the issues are ones of executability. An example is that of temperature. To keep the salt in a liquid form, operations are conducted in the 600 to 700°C range, much higher than the 300 to 350°C temperatures of the current generation of reactors. While most reactors are concerned about losing coolant from boiling, the MSR must consider freezing as a type of loss of coolant from the blockage of flow. Moreover, operating at higher temperatures with a mix of fission products in a bath of salts requires sustainable materials in these inhospitable conditions. Another example is that of fouling. In an MSR, fission products adhere to internal structural surfaces, plating components with radioactivity and heat from the decay of those fission products. The added heat and radioactivity would impact shutdown operations and maintenance.

Proponents counter that none of these challenges are insurmountable. Like all reactors, MSRs will require sound technical and engineering footing to maintain safe, continuous power. Material selection (or development in the absence of an adequate selection) is one of the most important aspects in this foundation. To be considered, the materials must have the appropriate strength, toughness, corrosion resistance, thermal conductivity and radiation tolerance. In evaluating longer term performance and maintenance concerns, one often overlooked aspect is the potential of the material for fouling. Fouling is the deposition and attachment of foreign material, such as corrosion products, on the surfaces exposed to coolant in a reactor. This foreign material layer commonly degrades the performance of heat exchangers and can be of sufficient magnitude to clog coolant passages and piping. An examination of the causes of fouling and better understanding of material susceptibility would be of value to reactor designers. In support of this view, this study was started. In particular, this study looked at fouling in an MSR by measuring adhesion forces of foulants.

## Introduction

In the Molten Salt Reactor Experiment (MSRE) run by the Oak Ridge National Laboratory (ORNL), metals born from fission were discovered to foul surfaces throughout the reactor [2]. Most of these fission product metals are radioactively unstable and upon decay release both radiation and heat.<sup>3</sup> Unlike a light water reactor (LWR), where fission products are produced and retained in the fuel rods, the MSR fission products intermix, flowing freely throughout the primary coolant and over the wetted surfaces. As a result, fouling in an MSR creates radioactive and thermally active hot spots in piping and components, which are not normally affected in an LWR.

---

<sup>3</sup>As will be explored in detail in part 3, the heat from radioactive decay has a strongly local effect. Up to a third of the decay energy (or more) comes in the form of particle kinetic energy such as beta particles, which give up their energy through short-range ( $\mu\text{m}$  scale) interactions with the electrons of the surrounding matter.

Such heat sources would be particularly problematic on components not designed to take such thermal loads or on replaceable components, which would complicate exchange and disposal. Moreover, high radiation from the buildup of this activity preclude normally afforded access for inspection and repairs during shutdown maintenance periods.

The study begins with a look at the key differences between an LWR and an MSR from the perspective of fouling. Both systems are negatively affected by fouling but in quite different ways. The foulants in the LWR's aqueous system come largely from the corrosion products of structural materials. The primary problem is a loss of heat conduction and the acceleration of corrosion [3]. For the MSR, fission produces a relatively large mass of material, as a kilogram of fuel fissioned results in approximately kilogram<sup>4</sup> of fission products, which are mostly radioactive. Some of the fission products are gases that are stripped away. Some form ionic salts and remain dissolved in the salt. However, those that are more chemically noble remain in their metallic forms and are the foulants in an MSR. The primary concerns with these foulants are the additional heat and radioactivity they bear.

The journey of foulants in the two reactor systems is similar. Already known is the birth source: corrosion in an LWR and fission in an MSR. Also known is the major transport mechanism: the flow of the coolant to the vicinity (within a few microns or less) near the surface of the fouling. Part 2 will examine the forces at play in taking a foulant from the salt to the surface proximity. Bubbles and mist play a role in the MSR, as noble metals appear to concentrate on the gas-liquid interfaces [2][4]. Electrochemical potential is the second key force [5]. Reversible reactions, such as changes of an element's form between its metal and ionic state, impact the element's propensity to foul. Furthermore, temperature differences or changes in local chemical equilibrium can cause changes in solubility. As a result, a foulant could be driven from the salt to precipitate on a surface [6]. In the final section of part 2, the forces of the last hundred nanometers of the journey are explored. As a collective of atoms, colloid foulants obtain bulk properties with van der Waals forces that extend out to this range. While such distances appear to be tiny, they are orders of magnitude greater than the tens of angstroms separations associated with pair potentials between individual molecules.

Moving from the physicality of foulants to the impact of foulants is the focus of part 3. Decay heat in a reactor is a tremendous source of energy in the seconds, days and centuries following the shutdown of fission in a reactor. It was the source of heat that caused the meltdowns at Three Mile Island and Fukushima and is the source of heat of continuing concern for spent fuel. Decay heat is formed from an amalgam of radioactive fission products, fuel and actinides. For an MSR, the noble metal foulants have both stable and radioactive isotopes. The radioactive foulants bring the decay

---

<sup>4</sup>approximately 0.1% of the mass is converted to energy during fission, which is about a fifth of the mass of a neutron.

heat to surfaces and components that may or may not be designed to carry the additional heat load. Additionally, the stable fission products will grow in mass with time. Excess mass will exacerbate solubility related problems and has the potential for other detrimental effects such as the acceleration of corrosion mechanisms similar to that seen in an LWR.

The primary concept of this work is to further the understanding of the propensity for adhesion of these fission products on reactor materials and would serve to aid the reactor designer in anticipating these fouling effects. Such knowledge would inform selection of plant materials, both for operating components such as pumps, flow detectors and heat exchangers, where fission product deposition would be undesired, and for processing components such as filters and fission product collection systems, where adhesion would be preferred.

## Objectives and Scope

The adhesion forces of five of the seven principal radioactive foulants discovered during the MSRE were obtained on six different potential structural materials by AFM-FS adhesion measurements. As will be explained in part 4, the foulants examined were niobium (Nb), molybdenum (Mo), ruthenium (Ru), antimony (Sb) and tellurium (Te) and the potential substrates examined were Hastelloy-N<sup>5</sup>, stainless steel 316L, ferritic/martensitic steel F91, commercially pure nickel (Ni-201), commercially pure molybdenum and silicon carbide (SiC). Hastelloy-N was a known fouled surface in the MSRE and served as a comparative reference source in this work.

To make these measurements, specially crafted and prepared AFM cantilever tips and substrates were prepared. The process and preparation are outlined in part 4. A combination vacuum chamber and glove box, with a sample cleaning argon sputtering gun, was designed and crafted to provide the desired inert environment in which an AFM was emplaced for taking these measurements. The construction and experimental processes are reported in part 5.

## Findings

The findings discussed in part 6 provide another piece in the larger question posed at the start. The relative adhesion stickiness between the chosen noble metal foulants and the potential substrates at room temperature in dry nitrogen were evaluated.

---

<sup>5</sup>Hastelloy-N is the trademark name by Haynes International who co-developed the Ni-Mo-Cr-Fe (Bal/16.91/6.96/4.24) alloy with ORNL specifically to resist corrosion in a molten fluoride salt in an MSR [7]. The alloy was initially called INOR-8 in early MSRE reports. Essentially all of the salt-facing metal components were made with Hastelloy-N in the MSRE.



The adhesion data widely varied between combinations but one key generalization was observed. Antimony, and to a lesser extent tellurium, were found more strongly adherent to Hastelloy-N than were niobium and molybdenum. This finding is encouraging because it is consistent with the fouling results of the MSRE [8]. Looking specifically at antimony and tellurium together, SiC demonstrated the least adherence; the other metals were comparable with Hastelloy-N. More data needs to be collected, but if a trend or correlation can be established, then continuing use of this study's experimental concept and design would be validated.

THIS PAGE INTENTIONALLY LEFT BLANK

## Part 2

# The Pathway to Fouling

**Fouling** Fouling has negatively affected nuclear power plants since their inception. As a thermal energy source, optimizing heat movement is essential in terms of both the efficiency (cost) of the power plant and in improving the lifetime of plant materials by reducing thermal stresses. Fouling disrupts both normal coolant flow and heat transfer. Furthermore, fouling can exacerbate corrosion by inducing increases in temperature and detrimental changes in chemical environment within pockets formed by the fouling deposit. Although the foulants in a molten salt are far different from the foulants in water, the impact of fouling is well illuminated by the common issues that plague an LWR. In section 2.1, the topic of fouling in an MSR is explored.

**Source and Transport** Foulants of reactors are born from corrosion products in LWRs and primarily from fission products in an MSR. The foulants are then carried by the liquid coolant to locations typically far away from their birthplace. Local environmental conditions may cause the foulant to precipitate or otherwise leave the fluid to land on a nearby surface. Such local conditions driven by surface effects and electrochemistry are discussed in section 2.2.

**Adhesion Forces** In a particulate model of fouling, the foulants form colloids while in the salt driven by interatomic forces and the complex thermodynamics of solubility equilibrium. As a collective of atoms, these colloids obtain bulk properties with forces that extend out to the range of hundreds of nanometers. In section 2.3, some of the concepts which will drive the materials to their last stop are examined. Indeed, the focus of this work is to explore by measurement the force of attraction in the final few nanometers of that journey.

## 2.1 Fouling in Reactors

### 2.1.1 Fouling in LWRs

In LWRs, fouling has been particularly costly in the secondary steam side of steam generators. Stress corrosion cracking enabled by fouling has caused primary-

to-secondary system leaks and steam generator tube failure necessitating expensive steam generator replacement [9], [10]. Moreover, mechanical deposition and biofouling [11] on the tertiary cooling water side of condenser tubes lead to losses in turbine efficiency and continuing costs for maintenance [12]. Fouling has even been shown to have caused mechanical degradation of non-heat exchanger components, such as pumps and valves.<sup>1</sup>

In modern LWRs, primary-side water fouling problems lie largely in the formation of crud on reactor fuel surfaces. Crud is a term coined by the nuclear industry for this persistent fouling of core surfaces. The precise mechanisms of crud formation are not fully understood, however the commonly held theory involves the coalescence of colloidal metals and their corrosion products during sub-cooled nucleate boiling on fuel cladding surfaces [14]. Physisorption onto the cladding surface by capillary and van der Waals forces provides an anchor, from which a crud layer forms. Still further adsorption on that first crud layer results in thicker and thicker crud. In the high neutron flux present in the core, crud becomes activated, and subsequently particles of crud break free and re-enter the coolant stream. Once mobile, the crud will deposit in low flow areas, causing localized high radiation fields far from the core [15]. The formation, activation time, and release of crud are dictated by the strength of adhesion forces, or ‘stickiness’ of the crud to reactor surfaces.

### 2.1.2 Fouling in an MSR

Similarly, in the high temperature salt environment in an MSR, the migration and adhesion of impurities create problems far removed from the core. However, unlike the aqueous environment of the LWR, for the MSR:<sup>2</sup>

1. The fuel is a liquid and constitutes part of the coolant. There is no fuel cladding surface to foul and no primary boiling. However, the fission products are not contained in a neatly packed fuel rod, and therefore form the bulk of the foulants of concern. Moreover, as with many fission products, the foulants are radioactive and bring with them a considerable decay heat load [4].<sup>3</sup>
2. The normally passivating thin oxide layer—chromium oxide on steel in an aqueous environment—is not a chemically stable protective layer in a molten fluoride salt [16]. Structural materials are stripped of this oxide and exposed. As such,

---

<sup>1</sup>One such problem is the mechanical seal leakage of reactor coolant pumps, where hematite originating from corrosion fouled the alumina seals in pressurized water reactors in France [13]

<sup>2</sup>A reader who is familiar with an LWR or in systems in water may not immediately recognize the remarkable differences in an MSR or conditions within a molten salt. A brief discussion on an MSR and its molten salts may be found in appendix A.

<sup>3</sup>For example, in a 1-GWe reactor running at 40% efficiency, 26 kg of niobium-95 (<sup>95</sup>Nb) is produced as a fission product in one year. <sup>95</sup>Nb decays with a half-life of 35 days. After one year of operation, the heat produced by the decay of <sup>95</sup>Nb, if entirely left on reactor surfaces, would be on the order of 750 kW. The amount of decay heat is more fully explored in part 3.

adhesion of any foulants would occur on bare metal surfaces as opposed to oxide layers in an LWR.

3. Corrosion of structural materials such as chromium, iron, and nickel was much different in the MSRE compared to that in a typical LWR. In an LWR, the structural metals are oxidized by water and these metal oxides then migrate into the circulating fluid. In the clean water environment of an LWR, the corrosion products are the main foulants and constitute the bulk of crud.<sup>4</sup> In the MSRE, nickel and iron were quite stable and experienced little corrosion. Chromium, however, is electrochemically more active than nickel and iron in a fluoride salt and as a result, was found to be the key source of any structural corrosion/depletion [17]. Moreover, as will be discussed in section 2.2.2 and appendix B, chromium showed potential for fouling facilitated by mass transfer over a temperature gradient.
4. The fluoride fuel salt is the solvent. Elements in their ionic fluoride forms, such as cesium fluoride or uranium fluoride, tend to have good solubility; while in their metallic forms, exhibit poor solubility. From this simple condition, the fission products that are quite electrochemically active, such as rubidium and strontium, are prevalently found in their salt forms and remain soluble in the salt. Whereas, fission products that are more noble, such as molybdenum and ruthenium, remain in their elemental metallic states and are found to be the foulants of interest. These "noble" metal fission products are the subject of this study. The key to understanding an element's metallic or ionic condition is its Gibbs free energy of fluoride formation and the existing electrochemical potential of the salt. These subjects are discussed more fully in section 2.2.
5. Some fission products that are produced in quantity, such as the short-lived molybdenum-99 (<sup>99</sup>Mo) isotope used in medical treatment, have high commercial value. Trapped inside a spent fuel rod of an LWR, <sup>99</sup>Mo decays long before it can be extracted for use. However, because the fission products are freely circulating in the coolant in an MSR, an opportunity is created for their selective deposition and extraction during reactor operations.

Even though crud in traditional LWRs exists in a vastly different form, the overarching journey is similar: (1) foulant introduction to the primary fluid system, (2) transport by the fluid system to the vicinity of the fouled surface, and finally (3) closing the gap and adhering to that surface. In both the LWR and the MSR, the first two stages are well understood. It is the final stage—the examination of crud in LWRs for example—which continues to capture the interest and research in the industry. While the examination of fouling in an MSR was primarily limited to the efforts during the MSRE decades ago, the revival of the MSR concept stimulated this new fouling study.

---

<sup>4</sup>Somewhat ironically, water is a highly corrosive impurity if introduced into the salt.

**Fluoride Salt or Metal - MSR Fission Products.** Given an element's inherent chemical potential and driven by the electrochemical potential of fuel salt, fission products are selectively fluorinated (oxidized). The potential of fluorination is graphically displayed in figure 2.1 of section 2.2.2. The MSRE's electrochemical potential was maintained in the region where both uranium (tetravalent) and uranium (trivalent) fluorides ( $UF_4$  and  $UF_3$ ) were stable as fluoride salts. Metals such as chromium and niobium lie near that electrochemical potential. Chromium was found mostly in its fluoride state, while niobium was largely found primarily in its noble metal form.<sup>5</sup> Some fission products such as tellurium with both positive and negative stable valence states are known to exist with other metals such as nickel ( $Ni_3Te_2$ ) and chromium ( $CrTe$ ) and theoretically could form compounds other than binary fluorides. However, the actual state of tellurium was investigated and remains undetermined [18]. The state of fluorination played a key role in solubility in the MSRE, which in turn drove fouling [2].

**The Five Particular Fission Products of this Study.** There are large numbers of fission products isotopes and metastable nuclear isomers, but only seven elements were discovered as foulants of measurable significance<sup>6</sup> in the MSRE [4]. The relatively insoluble noble metals foulants were niobium (Nb), molybdenum (Mo), technetium (Tc), ruthenium (Ru), rhodium (Rh), antimony (Sb) and tellurium (Te). Of these seven, this study will look at five of the elements primarily due to availability. The five elements subject to this study are niobium, molybdenum, ruthenium, antimony and tellurium.

**Fouled Surfaces in the MSRE.** Noble metals had plated out on nearly all surfaces exposed to the fuel salt in the MSRE [2]. The fuel salt-facing surface areas of the MSRE were comprised of essentially two materials. First Hastelloy-N, a nickel-molybdenum-iron-chrome based alloy, was developed exclusively by ORNL for the MSR and was used throughout the reactor. The primary heat-exchanger, the vessel and piping were all made from Hastelloy-N making up approximately one-fourth of the surface area in the reactor. Graphite made up the remaining three-fourths of the surface area and was used as the neutron moderator in the central core area of the vessel. While both materials were found to be fouled with the noble metals on their surface, graphite experienced deposition of other radioisotopes to varying degrees below the surface due to the penetration of radioactive gaseous isotopes such as xenon and krypton.

---

<sup>5</sup>Niobium was also found as a soluble fluoride when the salt's electrochemical potential became excessively oxidizing. In section 2.2.4, the dual nature of niobium in the salt is examined as an indicator of oxidation potential.

<sup>6</sup>The term measurable significance is relative. Fission products such as silver (Ag) and palladium (Pd) are noble as well, but the mass yields are low for any of the isotopes with activity beyond a few seconds. As such, their contributions are relatively insignificant.

In the nearly two years of power operations, the MSRE demonstrated the major disposition of fission products and generated a wealth of information from which other work can spring. In looking at fouling of Hastelloy-N, a natural follow-on question is whether other structural materials might foul to the same, more or lesser extent. As an extension, that question would also apply to the MSR salt processing and filtration systems. In partial answer to these questions, this study will look at the other materials as listed in part 1 and explored in part 4.

## 2.2 Foulant Drivers

In elementary terms, the fission product foulants are transported by the circulating salt. Coming into the vicinity of a surface, the local conditions and forces may exist for the fission product colloid to adhere. As explained by Epstein, the fluid forces can predict how a particle can get to a wall, but adherence is based on the competition between the adhesion force and the hydrodynamic force of the flow [19]. As would then be expected, places of lower flow would result in greater adhesion. This was indeed one of the outcomes in the MSRE heat exchanger. In situ radiographic monitoring and post-MSRE examination of the heat exchanger showed higher deposition rates near baffle plates, where disruption in the flow produced both turbulent regimes and low flow nooks and eddies. In these low flow areas, accumulation of activity primarily involved noble metals or noble metal decay progeny [20].

Beyond the mechanical forces of flow, other local forces such as those that impact solubility, flocculation and crystallization, affect the rates of attachment and the normally much smaller rates of detachment. Although there is no complete understanding of the fouling mechanics in an MSR, much was learned from the MSRE on specific forces at work. In particular, two key pathways are important to this discussion. First, gas transport and the liquid-gas interface were revealed as significant in MSRE fouling and came somewhat as a surprise to the ORNL team. Second, electrochemistry and thermodynamics have a substantial influence in this stage of a foulant's journey of transport to the site of adhesion.

### 2.2.1 Bubbles and Mist and Liquid-Gas Surface Transport

The MSRE had a robust gas management system to remove the fission product gases xenon and krypton but also to sweep out any other entrained gases such as hydrogen or fluorine from the salt [21], [22]. To induce the gas removal, helium was bubbled through the salt and recovered in the MSRE pump bowl, which served as the gas-to-liquid interface.<sup>7</sup> Of consequence, noble metals were discovered in much larger than expected concentrations in the pump bowl, particularly in the misty areas where the salt was atomized and sprayed as a stripping mechanism for the gases. The

---

<sup>7</sup>A cutaway view of the MSRE pump bowl is provided in appendix A figure A.2b.

significant amount found in the pump bowl was a surprise [2], [4].<sup>8</sup>

**Gas Bubble Surfaces** Upon further study, the MSRE team hypothesized noble metals found energetic stability on the surface of gas bubbles and subsequently plated out in areas where the bubbles collapse. Areas of foaming such as those found in the pump bowl were particularly susceptible [4]. The ORNL team found strong evidence of transport of noble metals by bubbles that are then deposited where those surfaces collapse.

**Mist (Liquid) Surfaces in Gas** Furthermore, the researchers postulated the surface of liquid mist in the gas was also a carrier for noble metals. Samples from vacuum dragged capsules lowered into the pump bowl gas volume showed an order of magnitude higher ratio of noble metal to salt-seeking isotopes than the samples taken from the pump bowl liquid. Additional analysis comparing the sprayed salt patterns on the outside of the capsule with the samples on the inside of the capsules found both salt-seeking isotopes and noble metals on the outside of the gas capsules, but very little of the salt-seeking isotopes on the inside. The researchers concluded the mist or liquid vapor in the gas carried noble metals at a greater expected rate on its surface than in the volume of the liquid drop [2].

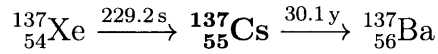
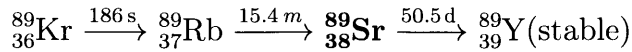
**Graphite and Noble Gas Interactions** Gaseous transport was a factor in the deposition of fission products in graphite. Large wetting contact angles between graphite and salt were experimentally demonstrated [23] and analysis of graphite samples from the MSRE showed the graphite is largely unwetted by the salt. To further reduce any graphite/salt reactions, the graphite used in the MSRE was specifically manufactured to minimize pores and pore sizes. On the surface, graphite was fouled principally by noble metals. However, the graphite's contamination by fission products was not merely a surface fouling effect: noble and non-noble fission products were found at small depths below the surface. The decay chains of many fission products include the gaseous elements of xenon and krypton. Some daughter products such as  $^{89}\text{Sr}$  (from the decay of  $^{89}\text{Kr}$ ) and  $^{140}\text{Ba}$  (from the decay of  $^{140}\text{Xe}$ ) were found below the surface. Moreover, the longer the half-life of the gas, the deeper the penetration into the graphite and the flatter the depth profile of the daughter or granddaughter activity. As examples,  $^{89}\text{Sr}$  and  $^{137}\text{Cs}$  were found deeper into the graphite than  $^{91}\text{Y}$  and  $^{140}\text{Ba}$  as an outcome those gaseous half-lives shown in the beta decay chains below [17].

---

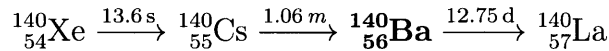
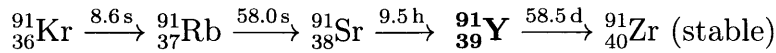
<sup>8</sup>When the fuel was  $^{235}\text{U}$ , 9% of the calculated inventories of noble metals were in the pump bowl. When the fuel was  $^{233}\text{U}$ , 86% of the calculated inventories were in the pump bowl. This discrepancy was due in part to the different methods used in measuring and calculating noble metals between the two different runs, but also the foaming and bubble concentrations differed between the runs. One researcher speculated that the second salt was much more oxidizing and had additional corrosion products and scum in the bowl [4]. Another researcher reported that oil leaking from the pump bearings significantly skewed the analysis [2].



Longer gaseous half-life, deeper fission product:



Shorter gaseous half-life, shallower fission product:



The graphite moderator was inspected and reported as clean, with little or no corrosion or physical damage, proving its short-term suitability in the MSRE [24]. More recent investigations with graphite indicate a beneficial role as it appears to absorb and retain tritium [25]. However, in the longer term, graphite is known to undergo asymmetric dimensional changes (shrink/swell) under neutron irradiation giving pause to its long-term suitability in a reactor [26]. The long-term view would also have to revisit fission product buildup, particularly that of noble gases.

## 2.2.2 Electrochemistry and Mass Transfer

The fouling constituents are those with electrochemical potentials in the salt that leave them in a metallic, less soluble form. The salt potential can also shift and create the thermodynamic condition for metals to leave the salt and crystallize as a solid foulant, such as found in mass transfer to colder surfaces. Although electrochemistry is not the subject of this work nor can it be adequately presented with justice here, some supporting concepts and illustrative examples are relevant to MSR fouling.<sup>9</sup> A more detailed discussion on electrochemistry is provided in appendix B.

### 2.2.2.1 Gibbs Free Energy of Fluoride Salt Formation - Standard State

The Gibbs free energy of fluoride formation described by the general reaction equation 2.1 and represented by figure 2.1 is useful to compare the various metals to understand their behavior in the salt. The more active metals such as cesium will remain primarily as a salt, whereas a more noble metal such as antimony will be found primarily as a metal. The calculations underlying the graph assume molar standard conditions at a given temperature and are provided in appendix B.

---

<sup>9</sup>Electrochemistry was a major area of study in the MSRE and there are numerous detailed reports regarding that 25 year effort. Two excellent open sourced summaries were provided by two of ORNL's leading chemists, Director W.R. Grimes in an article for Nuclear Applications and Technology in 1970 titled "Molten Salt Reactor Chemistry" and C.F. Baes in an article for the Journal of Nuclear Materials in 1974, titled "The Chemistry and Thermodynamics of Molten Salt Reactor Fuels". Grimes and Baes were lead or contributing authors on many of ORNL's MSRE chemistry reports. Their explanations helped solidify much of this researcher's understanding on this topic [5], [27].

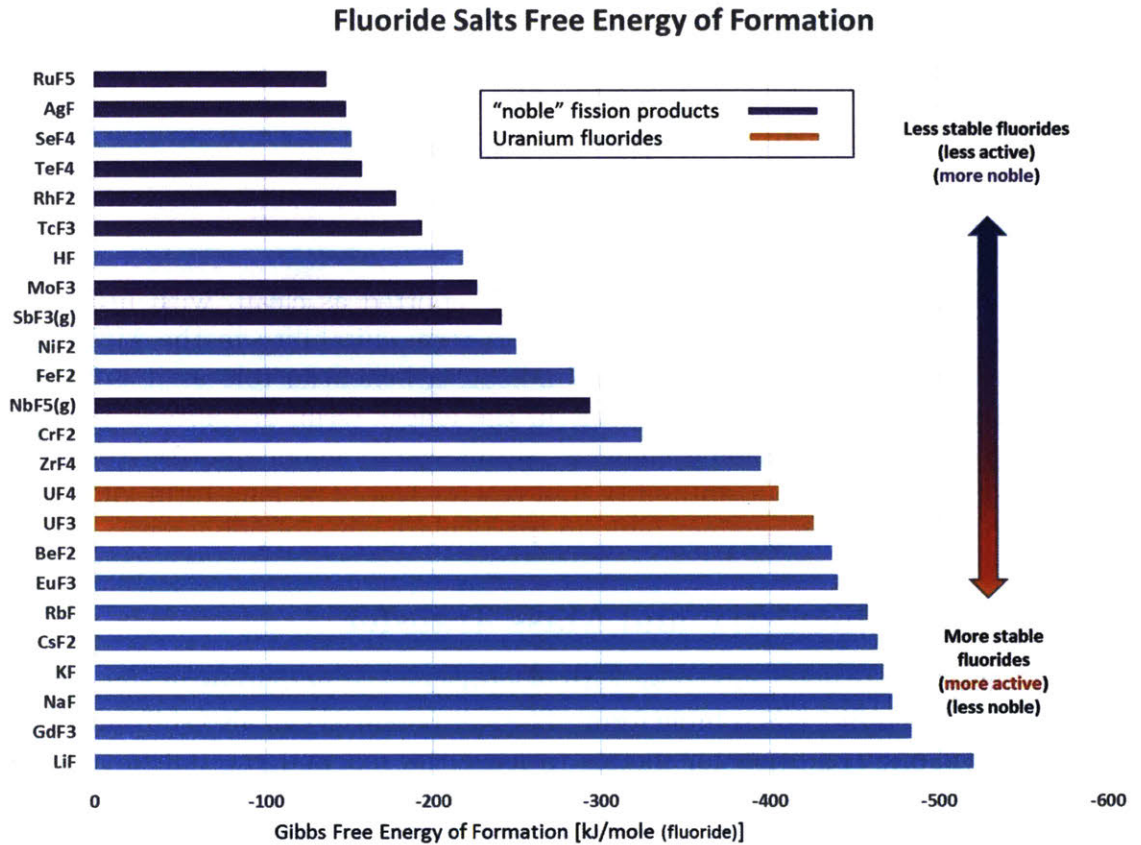
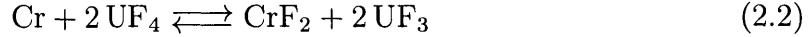


**Figure 2.1:** Gibbs free energy of formation of fluoride salts at 727 °C (1000 K) normalized per fluoride atom. The more negative the value, the higher the stability as a fluoride. Highlighted (in purple) are the noble metals, and (in orange) the stable uranium fluorides in the salt. The electrochemical potential of the MSR can be fixed to keep both UF<sub>3</sub> and UF<sub>4</sub> stable. Data sourced from HSC 6 software by Outokumpu Research Oy [28].

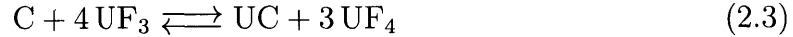
### 2.2.2.2 Gibbs Free Energy - Reactant Limited Condition

Figure 2.1 was calculated assuming chemical standard conditions of the presence of both the metal and fluorine. In the conditions of the MSR, fluorine and active metals such as uranium or lithium are virtually completely consumed so the electrochemical potential then is driven by the resulting ratios of the primary salt constituents. For the MSRE, the major constituent that drove the electrochemical potential in the salt was uranium, specifically in the forms of UF<sub>4</sub> and UF<sub>3</sub>. The reason is two-fold: (1) uranium was a dominant salt component much greater in concentration than any fission product or actinide; and (2) uranium had two stable fluoride states in the salt.

**UF<sub>4</sub> to UF<sub>3</sub> ratio** The ratio between UF<sub>4</sub> and UF<sub>3</sub> is crucial in the salt. If the ratio is too high, the salt is in an oxidizing state where an overabundance of UF<sub>4</sub> can corrode (oxidize) other metals such as chromium. A typical reaction among the metals is given by the chromium reaction.



If the ratio becomes too low and the salt is in a reducing state, the creation (and precipitation of uranium carbide (UC) becomes a problem.



The UF<sub>4</sub>/UF<sub>3</sub> buffer system was a key factor in maintaining the electrochemical potential of the salt in the MSRE [29].

### 2.2.2.3 Mass Transfer

A nine-year thermal convection loop corrosion study on was conducted on Hastelloy-N in a uranium-thorium-zirconium-lithium-beryllium fluoride salt to determine long-term suitability of the alloy for future MSRs. Corrosion rates were low as were found in the MSRE. However, mass transfer was noted in this study that was not directly observed in the shorter-lived MSRE: material migrated from the heated leg (700 °C) of the loop to the cooled leg (560 °C) [6]. The migration was selective only for chromium and was not seen for the other primary alloying metals of molybdenum, iron and nickel. As shown in figure 2.2, changes in temperature or the UF<sub>4</sub>/UF<sub>3</sub> buffer ratio may cause chromium metal to increase beyond its solubility point and crystallize (foul). The more active structural element chromium is shown to be more susceptible to this shift than iron or nickel.

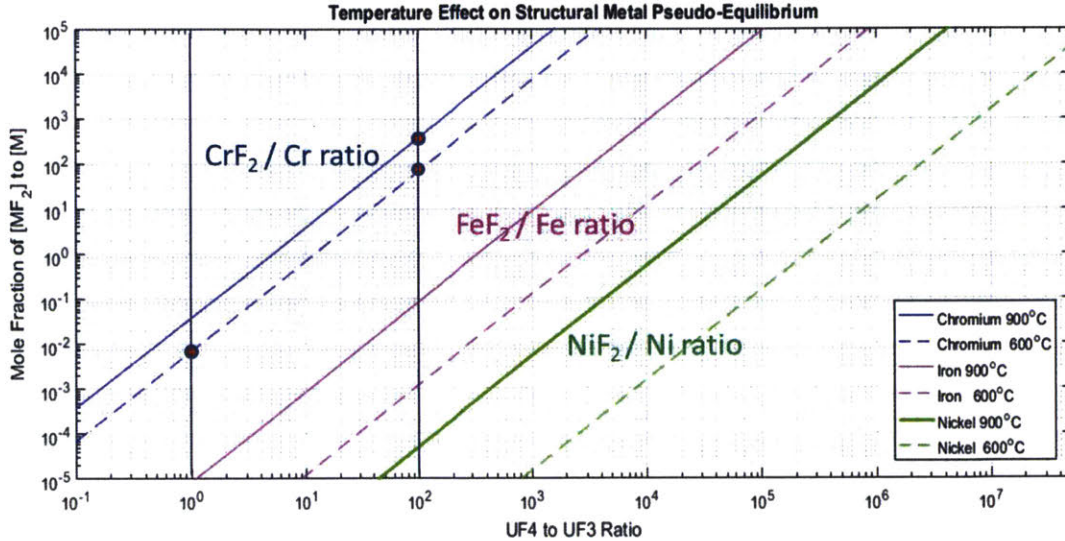


**Figure 2.2:** Equilibrium ratios of the metals chromium, iron and nickel between 900 °C and 600 °C as a function of the UF<sub>4</sub> and UF<sub>3</sub> ratio. A change in temperature affecting the salt-to-metal equilibrium could drive the metal beyond its solubility limit and cause the crystallization of chromium (fouling) as was seen in ORNL’s nine year test loop. Highlighted also are the chromium salt-to-metal ratio changes at 600 °C as the UF<sub>4</sub> to UF<sub>3</sub> ratio moves from 1 to 100. Reaction equations are provided in appendix B. Data sourced from HSC 6 [28].

**Fission Products and Mass Transfer** While the MSRE was highly successful, the low power (8 MWth) and relatively short time (2 years) as compared to a commercial power reactor produced relatively small amounts of fission products. The 3.75 kg of <sup>235</sup>U consumed during the operation of the first batch was less than 1-1/2 days of uranium fissioned in a 1-GWe reactor. The metal-fluoride (MF) to metal (M) ratio depicted in figure 2.2 was not a factor during the operation on the MSRE because of the low amount of fission product mass created. For future MSRs, as fission products build with time, the impact on solubility and recrystallization will need to be addressed.

### 2.2.3 Observations on Noble Metals of Interest

From analysis of measurements taken on reactor surfaces, the ORNL researchers made some specific observations on the noble metals of interest worth highlighting below.

1. Data scatter was substantial regarding the relative strength of affinity to fouling between Hastelloy-N and graphite. While there was no argument that noble metals fouled metal surfaces and graphite, there were points of departure regarding the relative magnitudes. In a semi-annual summary report, Hastelloy-N and graphite were reported to have had similar affinities for fouling with the

possible exception of technetium-99, which was found in greater deposition on metal [30]. However, in a more detailed analysis, one researcher found Hastelloy-N had a much greater concentration than graphite, particularly for antimony and tellurium [2].

2. The noble metals were found throughout the MSRE: in the salt, in the gas, on surfaces and below the surfaces in graphite [8].
3. Samples were normalized by comparing activity to the calculated total inventory of the material over time using decay chain calculations similarly to those discussed in appendix 3. As expected, salt samples showed most salt soluble ("salt-seeking") isotopes were around 100% of the calculated values and the noble metals were on the order of a few percent or less. However, some of the samples from the pump bowl were found to have 10 to 90% of the calculated value of noble metals. Also of interest, those high values tended to have a consistency in proportions of noble metals to each other [17]. The proportionality among metals despite varying half-lives suggested a type of equilibrium of total inventory of the metals in solution with their production rates [2].
4. Antimony deposited in all locations—stronger on metal than graphite. Tellurium, which is a daughter product of antimony, had a similar distribution [24].
5. Salt soluble ("salt-seeking") isotopes were found in negligible quantities on the surface of the graphite, but were found at small depths because of penetration by precursor gaseous isotopes [17].

A summary of their general findings is listed in table 2.1.

**Table 2.1:** Distribution of fission products in molten salt reactors <sup>1</sup>

Fission Product Group	Example Isotopes	Distribution (%)			
		In Salt	Metal	Graphite	Off-Gas
Stable Salt Seekers	<sup>95</sup> Zr, <sup>144</sup> Ce, <sup>147</sup> Nd	99	a	<1	a
Stable Salt Seekers <sup>2</sup>	<sup>89</sup> Sr, <sup>137</sup> Cs, <sup>140</sup> Ba, <sup>91</sup> Y	b	a	low	b
Noble Gases	<sup>89</sup> Kr, <sup>91</sup> Kr, <sup>135</sup> Xe, <sup>137</sup> Xe	Low	a	low	high
Noble Metals <sup>3</sup>	<sup>95</sup> Nb, <sup>99</sup> Mo, <sup>106</sup> Ru, <sup>111</sup> Ag	1-20	5-30	5-30	a
Sb and Te	<sup>125</sup> Sb, <sup>129</sup> Te, <sup>127</sup> Te	1-20	20-90	5-30	a
Iodine	<sup>131</sup> I, <sup>135</sup> I	50-75	<1	<1	a

<sup>1</sup> This table is reproduced from table 12.3 of ORNL Report ORNL-4865, *Fission Product Behavior in the MSRE* by E.L. Compere. [2]

<sup>2</sup> Stable salt seeker with noble gas precursors

<sup>3</sup> Noble metals excluding antimony and tellurium

<sup>a</sup> Negligible amounts measured

<sup>b</sup> driven mainly by half-life of the gas

## 2.2.4 Dual Nature of Niobium

Niobium has defining decay and electrochemical properties that can be exploited as indicators in an MSR. <sup>95</sup>Nb has a cumulative yield of 6.5% and a 39.2 day half-life. Its precursor, <sup>95</sup>Zr has a 64 day half-life and forms salt soluble fluoride complexes.

1. Decay Fingerprint. Having both elements in quantity in a reactor provides a radiographic indicator as the relationship (ratio) between the two elements can give researchers clues regarding pathways of fouling: Zr is normally a fluoride and Nb is normally a metal in the salt. One researcher used this ratio to postulate that <sup>95</sup>Nb had a higher concentration on the surface than in the bulk of the salt when analyzing the isotopic profile of the drain tank [20].
2. Electrochemical Indicator. The premise that niobium would be found in its metallic state and would be treated as a noble metal was not necessarily true under all circumstances. In the first batch of the MSRE, 32% enriched <sup>235</sup>U was used with the remainder being <sup>238</sup>U. The total uranium made up 0.9 mole% of the salt. This amount was sufficient to allow the control of electrochemistry by managing the buffering UF<sub>4</sub>/UF<sub>3</sub> ratio to roughly about the value of 100. In this batch, niobium (of which there is essentially only one isotope (<sup>95</sup>Nb)) remained noble. However, in the second batch using 90% <sup>233</sup>U, only 0.15 mole% of uranium was needed and the reduction of the buffer led to a wider electrochemical range in the salt. In particular, the salt was more oxidizing; <sup>95</sup>Nb was found (fluorinated) in salt samples and a greater corrosion of iron and nickel

were noted. Niobium, it seems, would be a good indicator of the electrochemical potential and health of the salt [17].

## 2.3 Particle to Surface Forces

In the last section, key macroscopic mechanisms that serve as transport to various destinations in the plant were highlighted. Visualizing the prevailing LWR crud concept as a model, the noble metals coalesce in an MSR, finding it energetically favorable to form insoluble colloids within its incompatible solvent salt. As a collective of atoms, these colloids obtain bulk properties with attractive forces that extend out far greater than the effective force associated between individual atoms or molecules. In this section, some of concepts that will drive the materials to their final destination are examined.

The physical attractive (and repulsive) forces between materials immersed in a gas or liquid are largely driven by dipolar interactions created by each particle's geometry and fluctuations of its electron cloud. These forces are known as van der Waals forces. There are three major categories of these two-body van der Waals forces: (1) Keesom forces generated by permanent dipole-permanent dipole interactions; (2) Debye forces generated by permanent dipole-induced dipole interactions; and (3) London or dispersion forces generated by induced dipole-induced dipole interactions. The dispersion forces are much more complex where perturbations of the electron clouds in non-polar atoms or particles create momentary electric fields, which induce similar time-varying polarity in neighboring atoms or particles. The time-varying electromagnetic fields when added, are standing fields which have the appearance of fixed photons. While not actually exchanged photons, they have a similar effect and are called virtual photons. These short-range dispersion forces are further complicated by the quantum fluctuations and retardation on the virtual photons exchanged in multi-body interactions. This additional effect is known as the Casimir effect and the force is known as the Casimir force.

### 2.3.1 Van der Waals Force at the Atomic/Molecular Level

Van der Waals forces are most clearly expressed between two atoms or molecules without interference of other bodies and it is at the atomistic/molecular level where this discussion will start.<sup>10</sup>

**Keesom and Debye Potential Energy and Force** Treatment of coulombic interactions using classical physics by Keesom and Debye showed the pair potential

---

<sup>10</sup>The following discussion and this researcher's understanding of the subject follows largely from two excellent textbooks on surface and intermolecular forces. The first by J. Israelachvili titled, *Intermolecular and Surface Forces, 2011* [31] and the second by H.J. Butt and M. Kappl titled, *Surface and Interfacial Forces, 2010* [32].

energy of these first two molecular van der Waals interactions to have an inverse sixth power relationship with distance of separation ( $1/r^6$ ) between the molecules.

$$V_{Keesom}(r) = -\frac{\mu_1^2\mu_2^2}{3(4\pi\epsilon_o)^2k_bT r^6} \quad \text{and} \quad V_{Debye}(r) = -\frac{\mu_1^2\alpha}{(4\pi\epsilon_o)^2 r^6} \quad [J]$$

where  $V(r)$  is the pair potential energy [J],  $\mu$  is the dipole moment of molecule 1 and 2 respectively [C-m],  $\alpha$  is the polarizability of a molecule [ $C^2 m^2 J^{-1}$ ],  $\epsilon_o$  is vacuum permittivity [F/m],  $k_b$  is Boltzmann's constant [J/K],  $T$  is temperature [K], and  $r$  is the separation distance [m].

If we set  $C_{Keesom} = -\frac{\mu_1^2\mu_2^2}{3(4\pi\epsilon_o)^2k_bT}$  [J-m<sup>6</sup>] and  $C_{Debye} = -\frac{\mu_1^2\alpha}{(4\pi\epsilon_o)^2}$  [J-m<sup>6</sup>], then for a given temperature, the first two parts of the van der Waals potential energy becomes:

$$V(r) = \frac{C_{Keesom} + C_{Debye}}{r^6} \quad [J]$$

Since force is the derivative of potential energy with respect to separation distance, the van der Waals force has a  $1/r^7$  relationship:

$$F(r) = \frac{C_{Keesom} + C_{Debye}}{r^7} \quad [N]$$

**London (Dispersion) Potential Energy and Force** Classical physics could not explain the dispersion forces of non-polar materials. London used quantum mechanics to model the pair potential as a pair of oscillators with each having a time varying state of polarization. London further expressed the forces in terms of each molecule's polarizability and the inherent frequency of its oscillator. This potential energy was also found to have a  $1/r^6$  relationship with the dominant term expressed as follows:

$$V_{London}(r) = -\frac{3}{2} \frac{\alpha_1\alpha_2}{(4\pi\epsilon_o)^2 r^6} \frac{h\nu_1\nu_2}{(\nu_1 + \nu_2)} \quad [J]$$

where (the additional terms),  $h$  is Planck's constant [ $m^2 kg/s$ ],  $\nu$  are the excitation frequencies of the respective molecules of the modeled harmonic oscillator [ $s^{-1}$ ].<sup>11</sup> Given the dominant frequencies and the polarizability of the two materials, the term can be written in a  $C/r^6$  relationship.

If we set  $C_{London}(r) = -\frac{3}{2} \frac{\alpha_1\alpha_2}{(4\pi\epsilon_o)^2} \frac{h\nu_1\nu_2}{(\nu_1 + \nu_2)}$  [J-m<sup>6</sup>] then the dispersion potential energy and force become:

$$V_{London}(r) = \frac{C_{London}}{r^6} \quad [J] \quad \text{and} \quad F_{London}(r) = \frac{C_{London}}{r^7} \quad [N]$$

---

<sup>11</sup>Later theories will expand on the notion of a single pair of oscillator frequencies to the infinite number of quantum frequencies associated with the molecules' structure. Those frequencies that affect dispersion forces are those that are absorbed and transmitted by a molecule.



**Keesom, Debye and London Combined** All three van der Waals energy components at the atomistic level demonstrated a  $1/r^6$  relationship and forces in a  $1/r^7$  relationship. In total, the van der Waals potential and forces are the summation where,

$$C_{total} = C_{Keesom} + C_{Debye} + C_{London} \quad (2.4)$$

so,

$$V_{VDW}(r) = \frac{C_{total}}{r^6} \quad [\text{J}] \quad F_{VDW}(r) = \frac{C_{total}}{r^7} \quad [\text{N}] \quad (2.5)$$

### 2.3.2 Quantum Electrodynamics Approach

Treatment using classical mechanics gives good approximations but does not capture the complete nature of dispersion forces. In making a more accurate model, the treatment using quantum electrodynamics by Casimir in 1948 and by Lifshitz in the early 1950s brought forward important developments.

**Casimir-Polder and the Effect of Electrodynamical Retardation** Actual experimental measurements consistently demonstrated a deviation from the  $1/r^7$  relationship in equation (2.5) where at some distance, nominally greater than 5-10 nm, the nature of the force decreased more rapidly than  $1/r^7$ . In 1948, Casimir and Polder presented a mathematical model that explained the deviation in van der Waals force involving the (virtual) photons exchanged between the electrons of both particles. In the classical formulation, the van der Waals induced dipoles are considered instantaneous, but as inter-particle distances increase, the transit time and interference of the reflected/exchanged wavelengths of the photons become important. The delay of the induced action is called retardation. Using quantum electrodynamics, the pair modeled the effect of retardation of two perfectly reflecting metal plates (i.e. perfect mirrors) on van der Waals forces [33]. Geometrically, the van der Waals forces for two parallel plates has a  $1/r^3$  relationship [31]. Casimir further calculated the force-distance relationship (in simplified form) drops off in a  $1/r^4$  relationship [34]. This is known today as the Casimir-Polder force (or effect) and also as simply the Casimir force (or effect).

$$F_{casimir} = \frac{hc\pi^2}{240d^4} \times A \quad [\text{N}]$$

where,  $hc$  is planck's constant times the speed of light [J-m],  $d$  is the separation distance of the two metal plates and  $A$  is the area of the plates [35].

As Israelachvili points out, the retardation effect is particularly strong in a fluid where the slower speed of light causes the reduction of force at distances of much less than 5 nm. The net result of the retarded van der Waals forces at the atomistic level is the change of dependency of the overall force with distance:  $1/r^7 \rightarrow 1/r^8 \rightarrow 1/r^7$  [36]. Moreover, actual materials are far from perfect reflectors so the forces on actual materials would tend to be much smaller. For example, metals with large coefficients of reflectivity have the strongest Casimir effect and Lambrecht reported the strength

to be about half that of the theoretically predicted value [35].

**Van der Waals Force – Macro and Bulk Affects** The atomistic models discussed above work well in dilute gases where the interactions are primarily one-to-one. Third body interactions are more complex and as such, the van der Waals energy and forces in solids and liquids require additional treatment.

### 2.3.2.1 Geometric and Simple Additive Approach

In crafting solid-to-solid models, the first attempts—which still offer valid estimations—assumed additive forces of individual atoms. In treating a solid as a summed collection of atoms whereupon energy and total force could also be summed by geometric integration, Hamaker developed a van der Waals relationship between two spheres [37]. Following upon his work, numerous other combinations such as plate-to-plate, sphere-to-sphere and sphere-to-plate geometries were calculated using similar methodology. In this study, the sphere-to-plate model is envisioned: the colloidal metallic fission product as a sphere and the structural material as a plate. For a condition where the radius of the sphere is much larger than the distance to plate, the van der Waals pair potential and force energy and force are:

$$V(r) = -\frac{A_H R_p}{6r} \quad [\text{J}] \quad \text{and} \quad F(r) = -\frac{A_H R_p}{6r^2} \quad [\text{N}] \quad (2.6)$$

where  $R_p$  is the radius of the sphere [m] and  $A_H$  is a constant named the Hamaker constant. Using this classical derivation, the Hamaker constant is defined as:

$$A_H = \pi^2 C_{total} \varrho_A \varrho_B$$

where  $\varrho_A$  and  $\varrho_B$  are the electron densities of material A and B respectively and  $C_{total}$  is shown in the derivation of equation (2.5) above. The difference in the effect on range between the atomistic force ( $1/r^7$ ) and this condensed phase bulk force ( $1/r$ ) is substantial and the implications should not escape notice. For spherical particles (and the colloids of interest in this work), van der Waals forces are powerful forces with relatively long range.

However, it isn't that simple. Hamaker and others recognized the limitations in the assumption of additivity. In condensed phases, interactions between atoms and their electrons via exchanged virtual photons and phonons become exceedingly complex. These effects were later addressed in a quantum electrodynamics based models where the geometric calculations (such as sphere-to-sphere, sphere-to-plate, plate-to-plate, etc.) and equations remained valid, but the means of calculating the Hamaker constant,  $A_H$ , changes.

**Optical Properties and Intervening Medium** Lifshitz followed to provide a van der Waals model based in quantum electrodynamics that evaluated a material's

bulk properties [31], [32]. This model does not look at the individual atoms, but rather uses the material properties as a continuum. As such, the model by its nature avoids the question of additivity in Hamaker's derivation.

The key determination was the optical properties of refraction and absorption were directly linked to van der Waals forces. Other researchers followed, demonstrating van der Waals forces could be calculated using dielectric properties of materials. In this treatment, equation (2.6) remains valid; however, the Hamaker coefficient calculations take on a different approach. The intuition behind Lifshitz' theory is the time variance of electron clouds and fields between materials create an exchange of virtual photons (at complex frequencies) that are directly related to the dielectric properties of the materials. The exchange of these virtual photons create the force which we witness as the van der Waals dispersion force. For a system where "a" is one solid, "b" is the second solid and "f" is the intervening fluid (or vacuum), the Hamaker constant takes the form dependent on the imaginary frequency components ( $i\omega_n$ ) of a complex frequencies ( $\omega_n + i\omega_n$ ) at which virtual photons are reflected and exchanged:

$$A_{Ham} = \frac{3}{2}k_bT \sum_{n=0}^{\infty} R_n(r)\Delta_{af}(i\omega_n)\Delta_{fb}(i\omega_n) \quad (2.7)$$

where  $k_b$  is Boltzmann's constant [ev/K], T is temperature [K],  $R_n(r)$  is the optical retardation length and  $\Delta_{af}$  is the difference in dielectric response between material "a" or "b" and intervening fluid "f" at  $i\omega_n$ . where,

$$\omega_n = \frac{2\pi n k_b T}{\hbar} \quad \text{with } n=1,2,3, \dots$$

and  $\Delta_{ab}$ , the difference in dielectric response is:

$$\Delta_{ab} = \frac{\varepsilon_a(i\omega) - \varepsilon_b(i\omega)}{\varepsilon_a(i\omega) + \varepsilon_b(i\omega)}$$

The imaginary frequency dielectric response function  $\varepsilon(i\omega_n)$  is related to the real frequency dielectric response  $\varepsilon(\omega_n)$  by:

$$\varepsilon(\omega_n) = \varepsilon'(\omega_n) + i\varepsilon''(\omega_n)$$

The  $n=0$  state or zero frequency relates to the electrostatic forces of permanent dipoles (the combination of Keesom and Debye forces) and the dispersion forces are described by the infinite sum (equation 2.7). In practice, the significant values lie within about the first 1000 terms and for most materials the impact falls in the range from infrared to ultraviolet. Regardless of this simplification, calculating the Hamaker constant in this method is challenging primarily because of the limited amount of spectral data for any two given materials and their intervening fluid.

**The Forces on Particles in Solution** The role of an intervening medium or fluid is crucial in the fouling model as it directly influences the van der Waals forces between the foulant and the fouled surfaces. The dielectric response of a material in a vacuum is at its maximum. Examination of equation 2.7 then suggests if the intervening medium is a vacuum, then the Hamaker constant would be at a maximum. In contrast, if the fluid had the same dielectric response as one of the solid materials, the differences  $\Delta_{af}$  as the foulant or  $\Delta_{fb}$  of the surface would tend to zero making the Hamaker constant (and the van der Waals force) vanishingly small. The forces in LWRs with water as the medium and in MSRs with salt as the medium, fall somewhere in between.<sup>12</sup> In the work of this thesis, the intervening fluid was nitrogen at room temperature, which has nearly the same dielectric response as a vacuum with a relative permittivity ( $\epsilon_r$ ) of 1.0005474 [38].<sup>13</sup> A complete study of adhesion in an MSR would need to factor in the effect of the salt on the noble metal foulants. High melting point coupled with high temperature kinetics present a formidable experimental challenge.

**Oxide Layers - Another Intervening Medium** Surface layers can affect the van der Waals forces when the distance of separation is of the same order of magnitude as the layer itself. As the space narrows and the separation distance shortens, Visser points out the closer material experiences a greater share of the force and if thick enough can effectively screen the forces experienced by the bulk material [19]. Taking a similar approach of macroscopic bodies in a dielectric medium as Lifshitz, Langbein calculated the effect of small adsorbed layers on two spheres and concluded the dominant force is by the adsorbed layer with separation distances less than the adsorbed layer. The dominant force is from the bulk at distances greater than the thickness of the adsorbed layer [39]. The geometry is illustrated by figure 2.3.

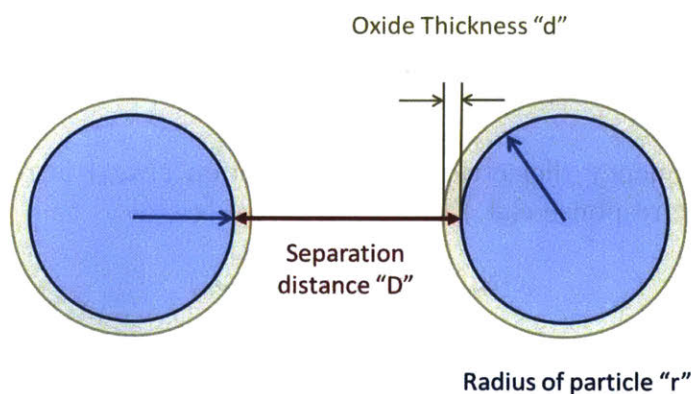


**Figure 2.3:** As the separation distance "D" between two particles shortens, the impact of the outer layer "d" becomes more important. When  $d \approx D$ , the material of the layer dominates the force.

<sup>12</sup>Intuitively, based on the optical properties in the visible range, the intervening fluid would have a much different dielectric response than either the foulant or fouled surfaces. This particular effort is the focus of study of two fellow student researchers.

<sup>13</sup>A material's dielectric constant is the same as relative permittivity. To obtain a material's permittivity  $\epsilon_s$  [F/m]:  $\epsilon_s = \epsilon_o \epsilon_r$  where  $\epsilon_o$  is vacuum permittivity.

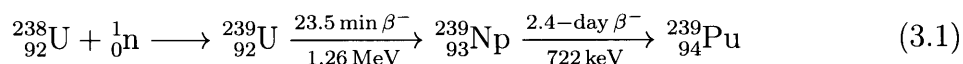
Langbein's conclusion had two important implications in this study's experimental setup described in sections 4 and 5. First, 4  $\mu\text{m}$  diameter spheres of silica were coated with 30-100 nm of the noble metals of interest. To obtain the measurement of forces between the noble metal and surface meant that the separation distance is required to be less than the thickness of the coating. This was accomplished through adhesion measurements made with direct contact of the two materials of interest. Second, the oxide layers formed on the substrates on the order of tens of nanometers could interfere with the actual contact and measurement being sought. As such, the experiment was designed to remove the oxide film on the structural materials of interest prior to making the measurements.

THIS PAGE INTENTIONALLY LEFT BLANK

## Part 3

# Decay Heat and Mass - Impact of MSR Fouling

Continuous power from a one gigawatt (GWe) commercial reactor plant involves the destruction of enormous numbers of fissile uranium or plutonium atoms—on the order of  $10^{20}$  per second. Maintaining such power requires sustainment of a high-density neutron flux field—on the order of  $10^{12}$  to  $10^{15}$  neutrons per  $\text{cm}^2/\text{sec}$ . As a result, fission products are born from the splitting of the heavy fuel elements, and still other isotopes are transformed as they also interact with the neutron flux. Most notable of these transformations take place in the actinides of the periodic table. Uranium-238<sup>1</sup>, a rather benign isotope that makes up for >90% of the uranium in a typical reactor, will absorb a neutron to become uranium-239 from which a series of decays and additional neutron absorptions will create a series of heavier elements. The main heavy elements of import are uranium, neptunium, plutonium,<sup>2</sup> americium and curium.<sup>3</sup> An example of activation is illustrated in equation 3.1. In this discussion, these heavy elements will be referred as actinides.



The decay of the radioactive isotopes in this elemental stew comprised of fuel, actinides and fission products is the source of decay heat. Each isotope releases the amount of energy between its activated state and its ground state in a probabilistic time (half-life) of decay. A fraction of this decay energy is in the form of kinetically propelled particles such as an electron/anti-neutrino pair in a beta decay or an  $\alpha$

---

<sup>1</sup>Uranium-238 is comprises 99.3% of natural uranium and the bulk of the uranium in enriched reactor fuel. For the enrichment to be 5% uranium-235, it is still 95% uranium-238. Uranium-238 is also fissionable in a high energy, or fast neutron flux and meaningfully contributes to power in a fast reactor.

<sup>2</sup>The buildup of plutonium-239 is advantageous in a reactor because it is also a fuel. At the end of the life for a spent fuel rod in an LWR, roughly 20-40% of the power is coming from the bred plutonium.

<sup>3</sup>In a thorium series reactor where fissile uranium-233 is bred from thorium-232, the actinide creation would also include thorium and protactinium.

particle (helium nucleus) in an alpha decay, as well as the recoil of the daughter nucleus. These particles travel quite short distances and release their kinetic energy in a localized region in the form of heat. Most of the remaining energy comes as a cascade of gamma and x-rays, as the excited state of the newly formed daughter isotope transitions to a final stable ground state.<sup>4</sup> In a large reactor, much of this energy is also turned into heat as the photons are absorbed in surrounding materials. This energy tends to be remote from the source and contributes to the overall heating of the structure and environment.

As the discussion pertains to fouling, the localized heat generated by the particle interactions is of main interest. Beta decay dominate the noble metal fission products' decay chains.<sup>5</sup> Typically, 10-30 percent or more of the total decay energy is carried by the  $\beta$  particle or electron.<sup>6</sup> This energy, if derived from a foulant, directly deposits on the fouled material. A graph of this potential heat will be presented in section 3.2.1

### 3.1 Decay Heat Over Time

Decay heat spreads out over a long period of time. Many of the actinides have decay half-lives in the million or billions of years (or more) time frame. They are of principle concern in the long-term storage of spent fuel. Most of the fission products (numbering in the thousands of isotopes and nuclear isomers) are radioactive and will decay virtually instantaneously. Several hundred of the remaining will decay in less than a day. Based on a review of the ENDF-VI nuclear database, there are over 60 that are stable and only a dozen or so with half-lives between a year and a century [40].<sup>7</sup> Cesium-137 (30.2 years) and strontium-90 (28.1 years) are commonly discussed because they are produced in some quantity and have half-lives that will have a meaningful impact for decades. Moreover, most daughters of fission product decays are they themselves radioactive. The chains can be many generations in length. As a result, heat generation continues from fission products long after a reactor shuts down. Figure 3.1 illustrates the radioactivity which creates decay heat over logarithmic time. The short-lived isotopes contribute about seven percent of reactor power at the moment fission stops, to about half of a percent at the end of one day. For a 40% efficient reactor producing 1 GWe of electrical power, the thermal power of the

---

<sup>4</sup>The description is a simple one-isotope decay. Fission products are normally part of a long series or chain of decays where daughter isotopes also experience decays.

<sup>5</sup>Alpha decays are predominantly found in the decay chains of the heavy elements such as the actinides. While they are not a factor in the specific noble metal foulants of this study, the MSR must still contend with this type of decay energy in the salt.

<sup>6</sup>Internal conversions (IC) are frequent means of a metastable isotope releasing its energy to form its ground-state counterpart. An electron is the primary particle which carries away the IC energy, often with more energy than an average  $\beta$  particle. The electron from IC is also a local heat generator.

<sup>7</sup>Technetium-99 is a major exception with a half-life of 211,000 years. It is one of the few fission products of decay concern beyond 300-500 years.



reactor needed would be 2.5 GWth. Decay heat amounts to a staggering 175 MW of thermal heat after the fission stops and 12 MW after one day. The high heat after shutdown and the indefinite continuing heat generation is a principle reason for the concern for fouling in the MSR.

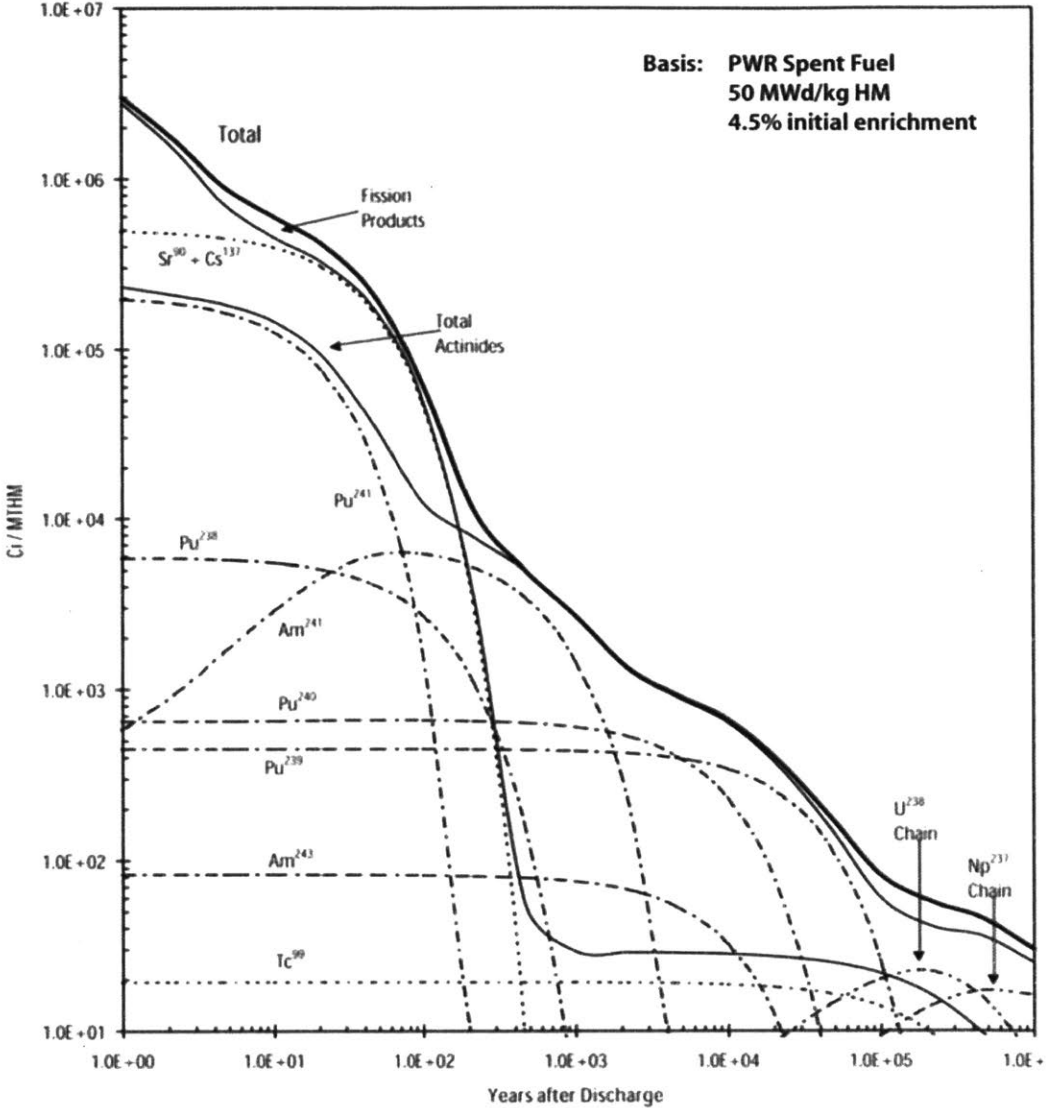


**Figure 3.1:** The long-term decay heat of spent nuclear fuel for a typical LWR is generated by the activity illustrated. The activity is dominated by fission products in the first ~200 years, after which the actinide activity dominates. Figure taken from the MIT *Future of Nuclear Power* study of 2003 [41].

### 3.2 Fission Products

In addition to the two to three neutrons released, each fission normally produces two new asymmetrically sized elements in a probabilistic fashion with a lighter element

such as  $^{95}\text{Sr}$  or  $^{90}\text{Kr}$  and a heavier element such as  $^{134}\text{Te}$  or  $^{138}\text{Xe}$ . With the exception of the three isotopes of hydrogen with atomic weights from 1 to 3, and helium with atomic weight of 4, the majority of the hundreds of different fission product isotopes have atomic weights between 68 and 164. The distribution of these fission fragments follows a yield curve based on the fissioned isotope and the energy of the absorbed neutron. 1000 kg of uranium or other fuel, which is fissioned, yields approximately 1000 kg of fission products. The mass buildup of fission products will be discussed later in this section. Figure 3.2 graphically depicts the average fission product yields from a thermal fission with the fuel used in thermal spectrum reactors:  $^{235}\text{U}$ ,  $^{233}\text{U}$  and  $^{239}\text{Pu}$ .

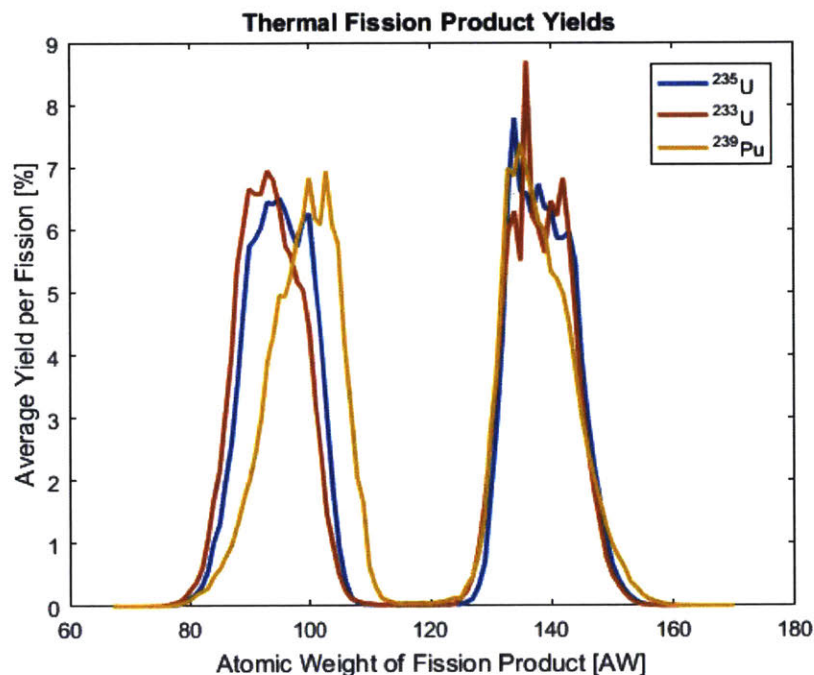


**Figure 3.2:** Thermal Fission Yield. Data from JEFF-3.1<sup>8</sup> and the IAEA Handbook of Nuclear Data for Safeguards [42]

### 3.2.1 Noble Metal Fission Products

What first makes the noble metals of our study of interest is because they are produced in some abundance as they fall under one of the two peaks in figure 3.2.<sup>9</sup> The second factor is they are all radioactive or fall within a radioactive decay chain and therefore contribute decay heat at a rate based on the half-lives of the noble metal isotope and its radioactive progeny. In the MSRE, the fission product noble

<sup>8</sup>JEFF-3.1 is the acronym for the Joint Evaluated Fission and Fusion File, Nuclear Data Library maintained by the Organization for Economic Co-Operation and Development (OECD)'s Nuclear Energy Agency (NEA).

<sup>9</sup>In table D.1 of appendix D, these noble metal isotopes fall in the atomic weight range of 95-105 and 121-132.

metals with sufficient decay activity to be notable were niobium (Nb), molybdenum (Mo), technetium (Tc), ruthenium (Ru), rhodium (Rh), tellurium (Te) and antimony (Sb). They are relatively insoluble in the salt and tend to come out of solution on adsorbing surfaces. A good illustration of the decay chain involving four of the noble metals is shown in figure 3.3.

The Fission Product Decay Chain(s) Leading to  $^{99m}\text{Tc}$  and  $^{99}\text{Tc}$

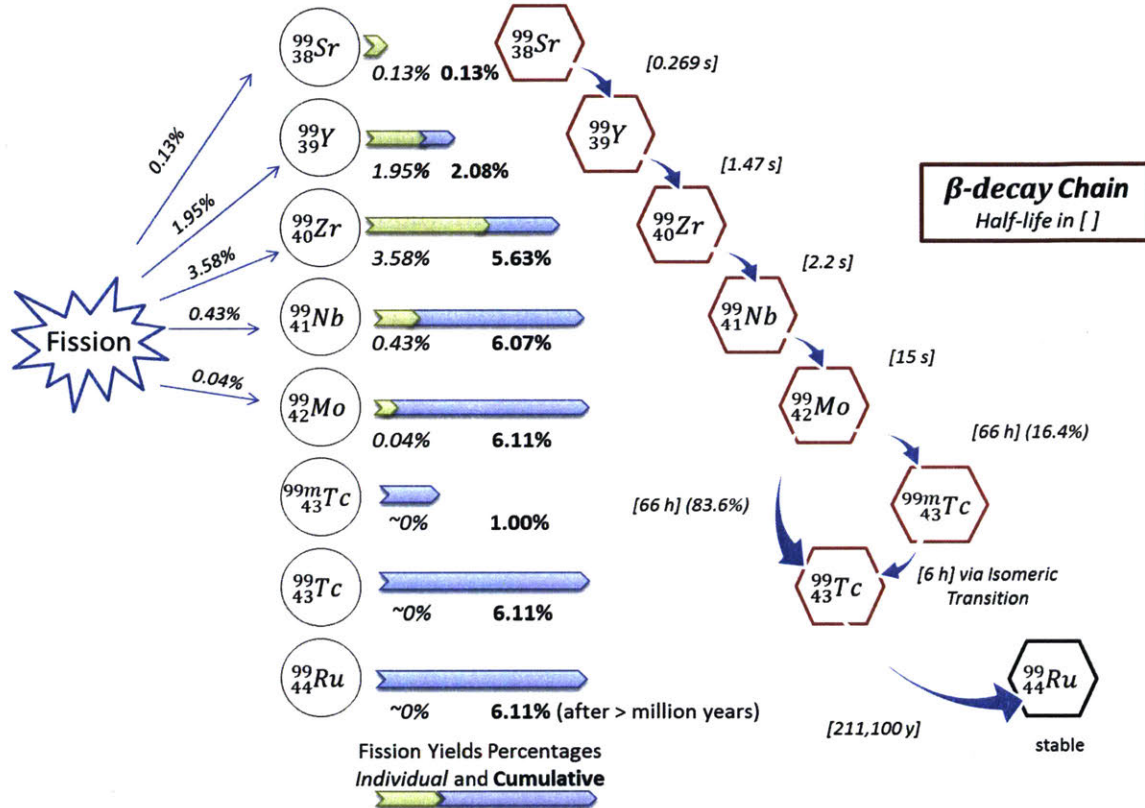


**Figure 3.3:** A typical decay chain from thermal fission of  $^{235}\text{U}$  that also highlights two important technetium isotopes. Approximately 6.11% of fissions have products that pass through  $^{99}\text{Mo}$ , which in turns decays. Approximately 16.4% of  $^{99}\text{Mo}$  decays to  $^{99m}\text{Tc}$ , a metastable isotope of technetium, which is one of the most important of today’s medical radioisotopes. With a 6 hour half-life,  $^{99m}\text{Tc}$  releases a gamma used in medical imaging as it transitions to its more stable isotopic form of  $^{99}\text{Tc}$ . Approximately 83.6% of  $^{99}\text{Mo}$  decays directly to  $^{99}\text{Tc}$ . This isotope of technetium is the main contributing fission product after a few centuries. The remainder of the fission products either have decayed away with shorter half-lives, or are of such low yield to have no significant contribution. Data from the National Nuclear Data Center, Brookhaven National Laboratory using ENDF-B-VII data)[43]

Noble metal deposition could create problems with (1) heat generation, (2) localized high radiation, and (3) corrosion. For the MSRE, it was only the latter that caused problems. Tellurium was found to cause cracking of the Hastelloy-N used for the vessel and most of the major components [18]. Because of the relatively short time frame and low power, the first two issues did not manifest themselves in the

MSRE. However, any reactor designer of future MSRs must plan for these issues.

**Activity and Heat Generation of Noble Metals** With the exception of  $^{99}\text{Tc}$  with a 211,000-year half-life, the noble metal decay chains are driven by half-lives measured in years and decades. The consequence of half-lives in this range is their most significant impact occurs in this period. In a continuous operation of reactor, most of the noble metals will build to a plateau within about 1000 days as shown in figure 3.4. The plot, logarithmic in time, shows the shorter-lived isotopes, such as  $^{99}\text{Mo}$  reaching equilibrium quickly, while the longer-lived isotopes such as  $^{106}\text{Rh}$  with a 371-day half-life building at a slower rate and not reaching equilibrium in the time scale of the plot.<sup>10</sup> Similarly, upon shutdown the impact of the noble metals are on the order of years as well as shown in figure 3.6. Methodology and calculations are provided in appendix C.

---

<sup>10</sup>Activity buildup takes approximately 7 half-lives to reach 99 percent of the equilibrium value. For  $^{99}\text{Mo}$  with a half-life of about 2-1/2 days (66 hours), the plateau is reached in less than 3 weeks. For  $^{106}\text{Rh}$  with a half-life of about 1 year (371 days), the plateau would be reached in about 7 years.

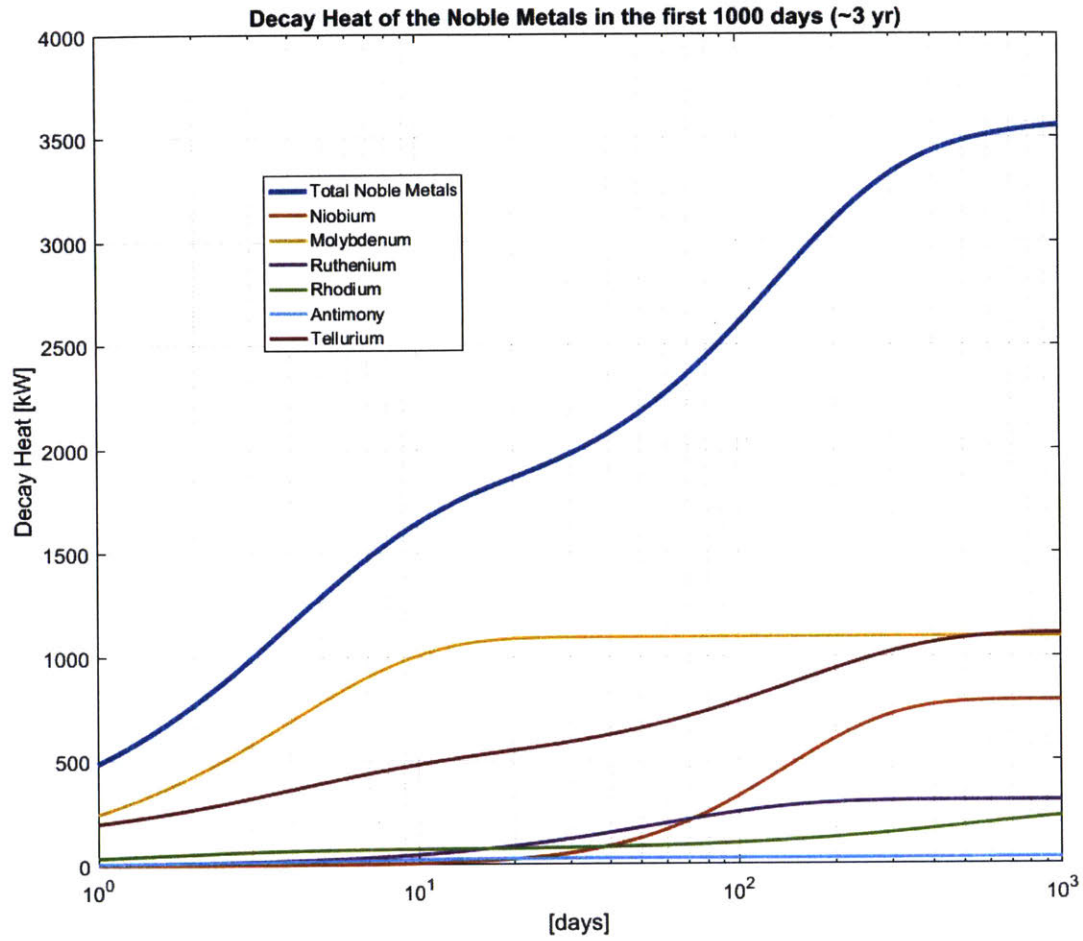


**Figure 3.4:** Based on continuous operations at 100% power for three years for a 1-GWe MSR, the decay heat from the noble metal foulants is represented. The graph is for the entire inventory and the amount which will foul onto surfaces would be less. Visualization is clearer with a logarithmic scale on the time axis. Assumptions and equations for calculations are presented in appendix C.

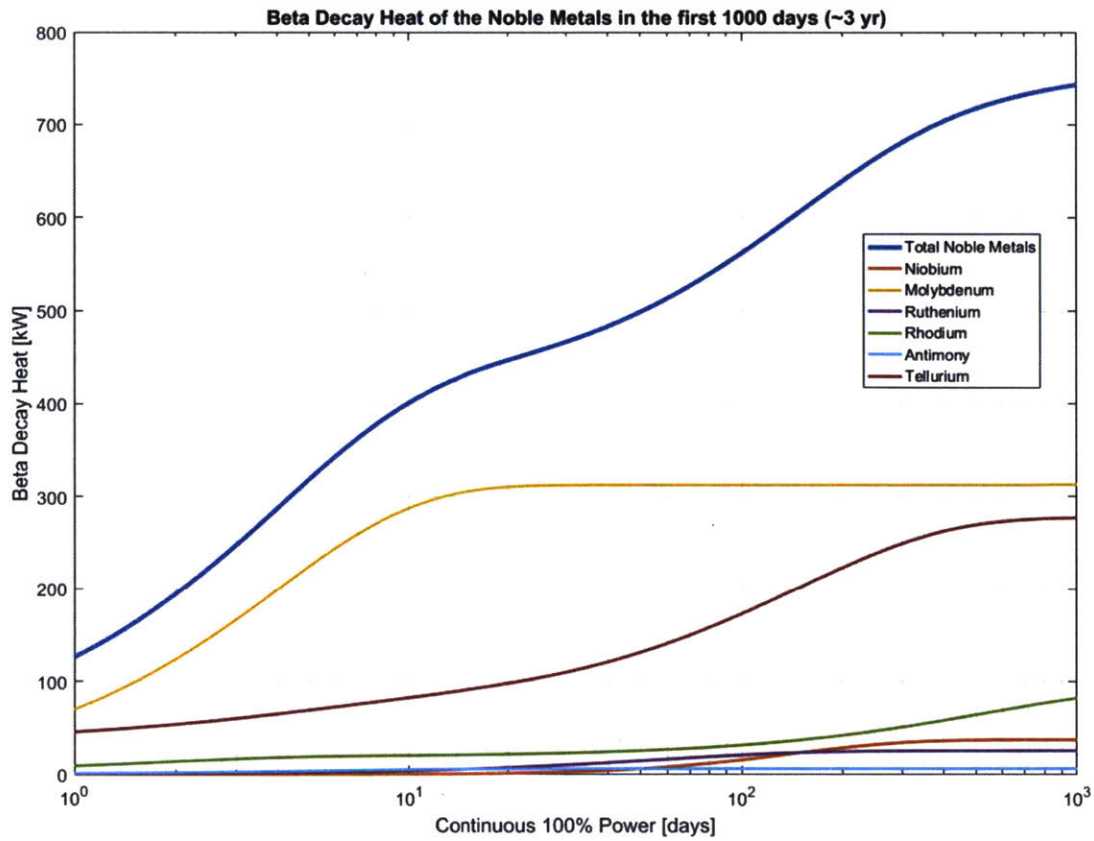


**Figure 3.5:** The direct energy imparted on the fouled surface is better reflected by the kinetic energy of the average beta particle in the decay of the noble metals as represented on this plot. Assumptions and equations for calculations are presented in appendix C.

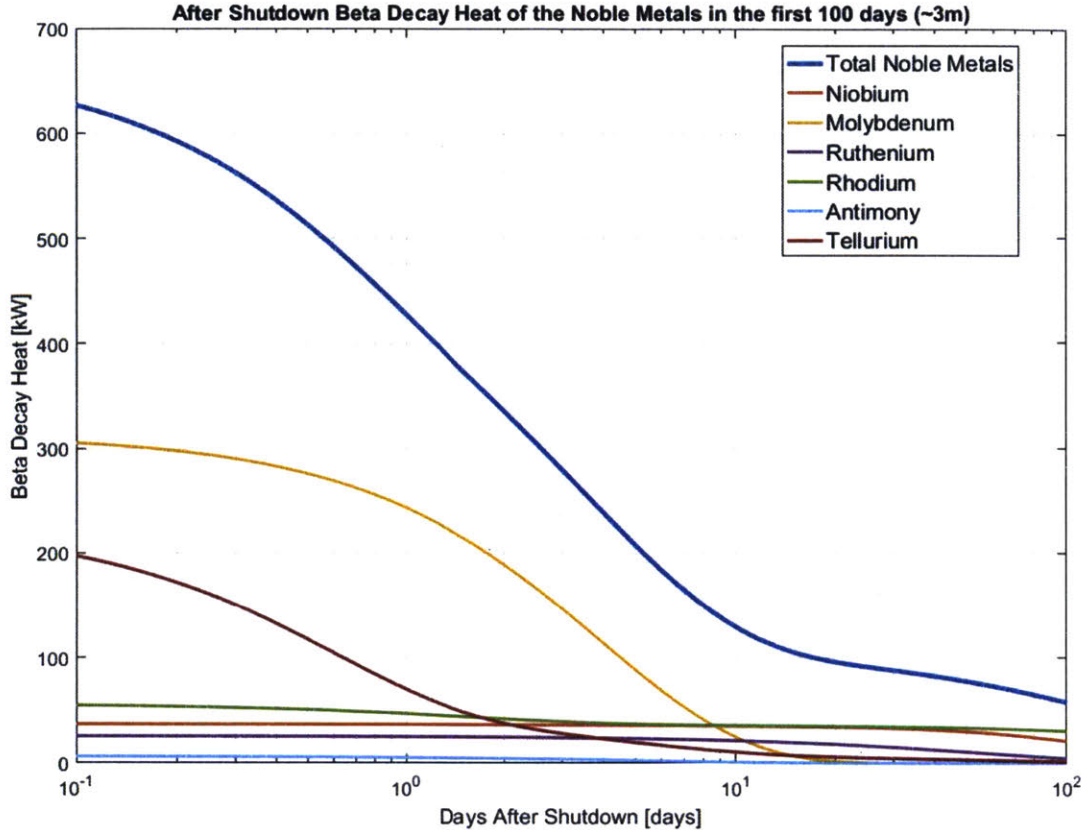


**Figure 3.6:** The localized decay heat from beta decay after shutdown remains significant. The starting assumption was a clean 1-GWe reactor operating for one year at 100% power prior to shutdown. In a logarithmic time scale, this plot shows the first 100 days following shutdown where the first third of the plot is the first day. Assumptions and equations for calculations are presented in appendix C.

### 3.3 Mass of Noble Metal Fission Products

Thus far, the focus on noble metal fouling has looked at the ramifications of the radioactive isotopes and the decay heat (and radiation) they produce. From the family of isotopes for any given element, the mass buildup is dominated by the stable isotopes. Molybdenum has four major stable fission product isotopes, which together result in the accumulation of approximately 100 kg for every 1000 kg of fuel fissioned.<sup>11</sup> The 100 kg of the stable <sup>95</sup>Mo, <sup>97</sup>Mo, <sup>98</sup>Mo and <sup>100</sup>Mo isotopes far exceed the buildup of 0.28 kg of the radioactive <sup>99</sup>Mo isotope.

The explanation is simple to rationalize with the most basic of fission product

<sup>11</sup>Similar to decay heat calculations, simplifying assumptions are made for the mass calculations herein. Table 3.1 presents results of these calculations using one year of operations from the same 1-GWe MSR from the previous section (section 3.2.1) on decay heat. The assumptions are provided in appendix C.

models where an isotope's sole production source comes directly from fission and is lost only by its own decay.

1. Assuming a cumulative yield fraction of  $\gamma$ , a constant fission rate of  $f$  atoms per second, and a half-life of  $t_{1/2}$ , an isotope  $N$ 's, rate of change is given by:

$$\frac{dN}{dt} = \gamma F - \lambda N \quad (3.2)$$

- $\frac{dN}{dt}$  Rate of change of isotope  $N$  [atoms/s].  
 $\gamma$  Yield fraction of isotope  $N$  [unitless].  
 $F$  Fission rate. Assumption of constant power yields a constant fission rate [atoms/s].  
 $\lambda$  decay constant is a function of half-life.  $\lambda = \ln(2)/t_{1/2}$  [s<sup>-1</sup>].

For a **stable isotope**,  $\lambda=0$ , and the differential equation simplifies to:

$$\frac{dN}{dt} = \gamma_1 F \text{ (a constant)} \quad (3.3)$$

2. **N number of atoms.** Assuming there were none of the isotopes of interest at the start of the reactor operation, the solutions to equations 3.2 and 3.3 are:

For a **radioactive isotope**:

$$N = \frac{\gamma F(1 - e^{-\lambda t})}{\lambda} \quad (3.4)$$

and for a **stable isotope**:

$$N = \gamma F \times t \quad (3.5)$$

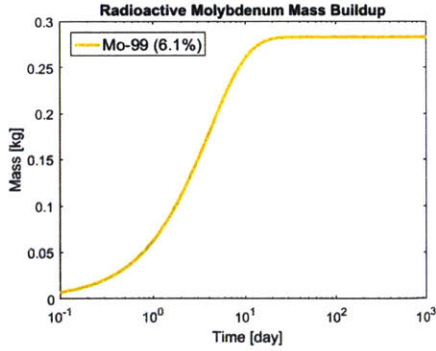
3. **Mass.** The mass in kilograms is calculated from numbers of atoms:

$$\text{Mass}(N) = N \times A_w \times N_{AV} \times 10^{-3}[\text{kg}] \quad (3.6)$$

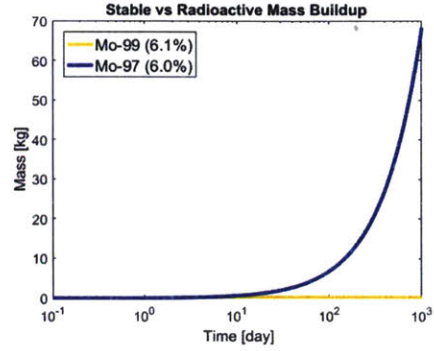
- $A_w$  Atomic weight [g/mole]  
 $N_{AV}$  Avogadro's number  $6.02 \times 10^{23}$  [atoms/mole]  
 $10^{-3}$  [kg/g]

From equation 3.2, an equilibrium occurs when the production rate by fission equals the removal rate of decay for the radioactive isotope. For a constant fission rate, the result will be a plateau in numbers (and mass) of that isotope. Stable isotopes however, will just build linearly with a constant fission rate as shown in equation 3.5. This effect is illustrated in figures 3.7 through 3.8, by the growth of molybdenum, where the isotope <sup>99</sup>Mo is radioactive and <sup>95</sup>Mo, <sup>97</sup>Mo, <sup>98</sup>Mo and <sup>100</sup>Mo are stable.





(a) Mo-99 equilibrium mass



(b) Mass of Mo-99 and Mo-97

**Figure 3.7:** Although both  $^{99}\text{Mo}$  which is radioactive with a half-life of 66 hours, and  $^{97}\text{Mo}$  both have cumulative yields of approximately 6% from fission, the mass build up is substantially different. The plot is provided on a logarithmic time scale to be able to show the buildup of  $^{99}\text{Mo}$  and then to directly compare that to  $^{97}\text{Mo}$  which is on the same logarithmic time axis.

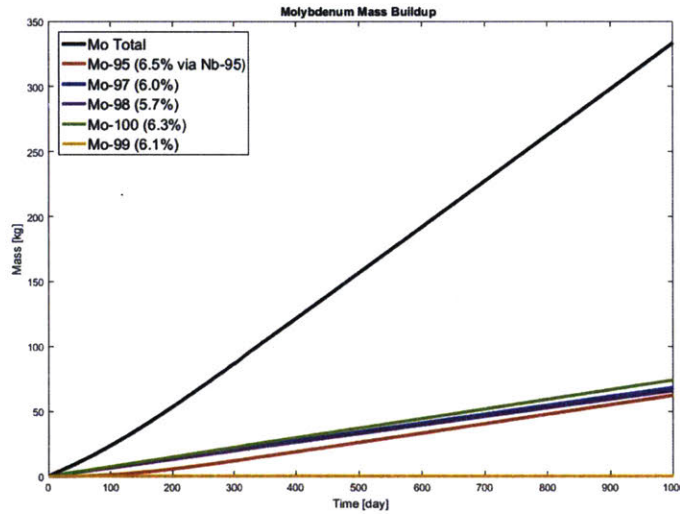


**Figure 3.8:** With four stable isotopes each with a yield of approximately 6%, the mass of molybdenum grows quickly.  $^{99}\text{Mo}$ , the one radioactive isotope of molybdenum of significance yield (also approximately 6%) is inconsequential when it comes to mass build up. This graph is presented on a linear time plot to better distinguish the differences in mass.

### 3.3.1 Fission Product Mass Estimates

Using a few reasonable additional assumptions from those used in providing the decay heat curves, the amount of fission product mass generated in a 1-GWe MSR

in one year can be estimated. These additional assumptions are listed below. Other assumptions and calculations are provided in appendix C.

1. Gases of half-lives greater than one hour are swept out. Removal of the gases in an MSR is an objective in most designs. Xenon is a neutron poison and its removal improves neutron economy. Moreover, since gases are poorly soluble in the salt and pressure is maintained at nearly atmospheric pressure, a gas management plan/system is required.
2. Fission products with half-lives on the order of six weeks or less have decayed. Looking at a one-year time frame allows this assumption. There will be fission products of these half-lives remaining that were born toward the end of the year and their radioactivity may be a measurable short-term contributor to decay heat. However, because of their relatively short half-lives, their mass will not build to any appreciable level and their activity would quickly decay.

Niobium is an example of such an element. As a fission product, there are no stable isotopes of sufficient yield to build up to any level significance, as there are with molybdenum. The only isotope of niobium with sufficient yield and half-life to be a measurable decay heat contributor is  $^{95}\text{Nb}$ , with a cumulative yield of 6.5% and a 39.2-day half-life. The fission yield indicates approximately 26 kg of  $^{95}\text{Nb}$  is produced from the 1000 kg of fuel; and the short half-life indicates it decays within a few months of production. Much like  $^{99}\text{Mo}$ , mass builds to some small equilibrium value and decays away upon shutdown. So for the mass calculations,  $^{95}\text{Nb}$  is just considered the parent of  $^{95}\text{Mo}$  which is stable. Similarly, in the tally of mass,  $^{99}\text{Mo}$  is not included in the molybdenum totals, but shows up as the majority parent of  $^{99}\text{Tc}$ .

3.  $^{235}\text{U}$  is the only fuel. Although other actinides will fission, the contribution in the first year would be small. The major additional contributor after a longer period of reactor operation would be  $^{239}\text{Pu}$ . However, since the fission yield curves are similar enough with  $^{235}\text{U}$  as shown in figure 3.2, using a  $^{235}\text{U}$ -only set of curves is reasonable.<sup>12</sup>

The major fission product masses are provided in table 3.1.

---

<sup>12</sup>There are a few isotopes with significant yield differences between  $^{235}\text{U}$  and  $^{239}\text{Pu}$ .  $^{106}\text{Rh}$  has a 0.4% yield in  $^{235}\text{U}$  and a 4.0% yield in  $^{239}\text{Pu}$ . A more accurate estimate of the fission products with significant differences in yield would have to consider the change in fuel mixture.

**Table 3.1:** Mass of Fission Products per 1000 kg of  $^{235}\text{U}$ 

Assumes (a) burn-out and activation of fission products are negligible, (b) one year of continuous operations, and (c) the short-lived fission products have all decayed to insignificant levels. Values calculated using data from ENDF/B-VI database as compiled by T.R. England and B.F.Rider, Los Alamos National Laboratory, 1993 [40]

Element	Atomic Number & Symbol	Cumulative Yield [%] <sup>1</sup>	Cumulative Mass [kg]	Notes
Xenon	(54) Xe	32.20	183.2	20% Xe-135 (9.1 h) and 21% Xe-131 (5.24 d)
Neodymium	(60) Nd	20.74	127.7	
Zirconium	(40) Zr	30.66	121.6	
Molybdenum	(42) Mo	24.56	101.9	<sup>3</sup>
Cerium	(58) Ce	12.05	72.3	
Ruthenium	(44) Ru	11.75	51.5	3% Ru-106 (372 d)
Barium	(56) Ba	6.76	39.7	
Krypton	(36) Kr	10.68	39.3	33% Kr-88 (2.8 h) 24% Kr-87 (1.3 h) and 12% Kr-85 (10.75 y)
Lanthanum	(57) La	6.47	38.3	
Cesium	(55) Cs	6.34	36.9	99.99% Cs-137 (30.1 y)
Praseodymium	(59) Pr	5.86	35.2	
Technetium	(43) Tc	6.18	26.0	
Strontium	(38) Sr	5.91	22.6	99.6% Sr-90 (28.8 y)
Yttrium	(39) Y	4.75	18.0	
Promethium	(61) Pm	2.25	14.1	100% Pm-147 (2.62 y)
Rhodium	(45) Rh	3.03	13.3	
Tellurium	(52) Te	2.15	11.9	
Samarium	(62) Sm	1.83	11.7	23% Sm-151 (90 y)
Palladium	(46) Pd	1.19	5.3	
Iodine	(53) I	0.69	3.8	
Selenium	(34) Se	0.47	1.6	
Europium	(63) Eu	0.19	1.2	17% Eu-155 (4.71 y)
Tin	(50) Sn	0.10	0.5	
Bromine	(35) Br	0.13	0.4	
Antimony	(51) Sb	0.04	0.2	53% Sb-125 (2.8 y)
Cadmium	(48) Cd	0.04	0.2	
Silver	(47) Ag	0.03	0.1	
Gadolinium	(64) Gd	0.01	0.1	

Table 3.1 cont.

Table 3.1 Mass of Fission Products per 1000 kg of  $^{235}\text{U}$  cont.

Element	Atomic Number & Symbol	Cumulative Yield [%] <sup>1</sup>	Cumulative Mass [kg]	Notes
Indium	(49) In	0.01	<0.1	
Rubidium	(37) Rb	<0.01	<0.1	
Niobium	(41) Nb	<0.01	<0.1	from $^{95}\text{Zr}$ <sup>2</sup>

<sup>1</sup> Cumulative yields, when totaled, would be approximately 200% since the average of two fission products are yielded for each fission. Mass, on the other hand is conserved. Total mass would be approximately 99.9% of the fuel consumed, where approximately 0.1% of the mass is converted to energy.

<sup>2</sup> Even though table 3.1 seems to show Nb as insignificant, it is because of the year horizon built into that table and the tally assumption that all fission products with half-lives less than a year had decayed. Its precursor,  $^{95}\text{Zr}$  has a 64-day half-life. The mass tally for these two elements shows up as stable  $^{95}\text{Mo}$ .

<sup>3</sup> There are four stable isotopes of molybdenum, all of which have approximate cumulative yields of 6%. They are  $^{95}\text{Mo}$ ,  $^{97}\text{Mo}$ ,  $^{98}\text{Mo}$  and  $^{100}\text{Mo}$ . The one molybdenum isotope which is produced with a 6.11% yield is  $^{99}\text{Mo}$ . Its half-life is 66 hours and is not part of this tally. The major source of the long-lived  $^{99}\text{Tc}$  is from  $^{99}\text{Mo}$ .

## Part 4

# Material Selection and Sample Preparation

### 4.1 Selection of Materials for the Study

The foulants and fouled surfaces came naturally from the results of the only MSR to have operated for any length of time—the MSRE.

#### 4.1.1 Foulants - AFM Cantilever Tips

The focus of this work looked first at the seven foulants of significance identified by ORNL: niobium (Nb), molybdenum (Mo), technetium (Tc), ruthenium (Ru), rhodium (Rh), antimony (Sb) and tellurium (Te). They had both sufficient mass (and longevity) and had isotopes of sufficient activity to be identified by their decay spectra. Silver (Ag) and palladium (Pd) are both noble metal fission products, but silver is of low yield and palladium is primarily a stable metal. The mass and yield of fission products are summarized in table 3.1 in part 3. Of these seven, five were obtained for this study: niobium, molybdenum, ruthenium, antimony and tellurium. Technetium is not naturally occurring and is unavailable. Rhodium was not available in the required sputter target configuration needed when the study began. Specific data regarding the obtained elements may be found in appendix D. Preparation of these metals as coatings on AFM cantilever tips will be discussed in section 4.2 below.

The MSRE had a robust salt and materials monitoring program during operations and during shutdown periods between each run. Fission product assessment was included in this monitoring program and the fouling (by these noble metals) was an important subset. It should be noted that all samples were highly radioactive and the typical methods for analysis were severely restricted or complicated by that factor. Some samples could not be evaluated for weeks (or years) to allow sufficient decay of radiation levels to handle for examination. Simple cleaving and inspection by microscope in most laboratories were required to be executed in a shielded glove box. A brief description of the monitoring types and methods important to the determination of fouling is found in appendix A.

### 4.1.2 Structural Material - AFM Substrates

This study was executed in conjunction with the efforts of other students whose work included the study of corrosion and radiation-affected corrosion in molten salt conditions. The substrate materials were chosen as those which were likely to be facing the salt in a future MSR. Hastelloy-N served as the first choice as it was the only structural alloy used in the MSRE and can be used as a point of reference. A literature review quickly suggested stainless steel 316L as a second choice. An additional iron based alloy F91 is being evaluated as potential candidate, so it became the third substrate. Since nickel based alloys have demonstrated the best corrosion resistance in molten fluoride salts, consideration is being given to use commercially pure nickel as a protective bonded layer on a cheaper alloy such as steel. The idea is similar to the use of stainless steel as a protective layer on carbon steel in LWRs today. As a result, Nickel-201 became the fourth structural element for evaluation. With the advent of Hastelloy-N in the 1960s for the MSRE, molybdenum as an alloying metal has shown great promise. Similar to the logic used with nickel, evaluating commercially pure molybdenum as a potential salt-facing material made it the fifth substrate to be evaluated. A sixth substrate was added just before the experimental setup was finished. Silicon carbide (SiC) has had growing interest in the nuclear industry because of its high temperature strength, low neutron cross section, high melting point, and recent manufacturing advances enabling creation of brittle fracture resistant SiC composite structures. All the materials were commercially procured. The specific compositions were pulled from the manufacturer's testing and certification sheets and the pertinent information is included in appendix D.

All the metal substrates were mechanically polished on a Buehler MetaServ 250 with the following routine. Using Buehler's guide, 240 grit paper or the 70  $\mu\text{m}$  polishing mat were used with water until smooth. Normally this would entail 3-20 minutes. The samples were then polished with 400, 800 then 1200 grit paper and water for 3-5 minutes each and inspected at each stage. If large scratches remained visible, a return to lower grit paper was warranted. The next two phases used Buehler MetaDi diamond suspensions: 3  $\mu\text{m}$  then 1  $\mu\text{m}$  suspensions. Similarly to grit paper, these would run from 3-5 minutes with inspections in between. The last polishing stage used Buehler MasterPrep Alumina 0.05  $\mu\text{m}$  suspension for about 5 minutes. Examination under an optical microscope at magnifications of 50-100x was sufficient to inspect the surface. In particular, dark-field reflective optical microscopy readily highlights polishing scratches not immediately obvious in bright-field reflective optical microscopy. Molybdenum and nickel were the most difficult to achieve a smooth surface and at times, those two substrates required additional polishing.

A 40 nm layer of gold was sputtered on top of the newly polished surfaces. The purpose of the gold was two-fold. First it gave a visual clue on where the argon sputtering was conducted as part of the final oxide and contaminant removal prior to measuring on an AFM. In section 5 the details of the argon sputtering will be elaborated. Second, the gold provided a known value for which a baseline for the

argon sputtering could be established. As discussed in section 5, the argon sputtering gun rate could be compared with quantitative argon sputtering on a depth profiler using X-ray Photoelectron Spectroscopy (XPS).

## 4.2 Cantilever Tip Preparation

The concept of the experimental plan was to functionalize AFM cantilever tips with a sphere of the predicted foulant of an MSR and measure the forces of that sphere against a flat structural material. Such a geometry is well characterized in theories of energy and forces between bodies [36]. However, because of the unusual materials for study—MSR noble metal fission products—obtaining cantilevers to conduct measurements on the AFM was challenging.

Accomplishment of this task met with several failed attempts before successfully mounting spheres with noble metal surfaces onto the cantilever tips. The attempts, misses and successes are outlined below. A summary of cantilever types, spring constants, noble metal coating and depth of coating is provide in table 4.1.

1. Limited Selection of AFM Cantilever Force Constants/Spring Constants. Most AFM chips come with a sharp downward pointing probe at the end of the cantilever that is used to scan the surface of the object. This work needed a bare AFM cantilever tip so that a customized sphere could be mounted on the end. Although available, bare cantilever tips are a minority product and the selection of cantilever spring constants are more limited. Since the force values to expect were unknown, a number of probes with different cantilever spring constants were initially purchased to narrow down the range. Further limiting the choices was the later use of a desktop sized AFM, the ezAFM AQUA by NanoMagnetics Instruments, Oxford, UK. This AFM required AFM chips with alignment grooves. Figure 5.4 in part 5 shows a photograph of an alignment chip of the kind in the ezAFM and the backside of an AFM chip with the required alignment grooves. This further narrowed the choices of available cantilever spring constants. The final measurements were made on cantilevers with a nominal 3.3 to 5.1 N/m spring constant. Fortunately, this spring constant proved to be of adequate magnitude.
2. Spheres of the noble metals in the 1-10  $\mu\text{m}$  range were difficult (if not impossible) to find. Finely screened nickel powder and molybdenum powder (chemical reagents) were immediately available. The decision was made to try to sputter coat the other noble metals on either the nickel or the molybdenum particles.
3. The in-house attempt at mounting spheres to cantilevers proved too difficult to mass produce by hand. Therefore, the tipless cantilevers and molybdenum powder were sent to Novascan Technologies, Inc, Ames, IA for professional mounting. First measurements in the AFM were met with inconsistent results. Close examination of the tips in a scanning electron microscope (SEM) revealed

large asperities on the surface of the molybdenum particles. Upon further examination, the nickel particles similarly suffered from severe asperities. Figure 6.4a in part 6 shows an SEM image of a 0.1 N/m cantilever with a molybdenum particle. The roughness of the particle is discernible in the image.

4. Metal particles with good sphericity were not located, but monodispersed silica ( $\text{SiO}_2$ ) particles of 4  $\mu\text{m}$  diameter and  $>99\%$  sphericity were found and purchased from Cospheric LLC, Santa Barbara, CA. These spheres were sent to Novascan for mounting on AFM cantilever tips.
5. Sputtering was conducted by the Moodera Research Group, a condensed matter physics group at MIT, that had recently assembled a large sputtering machine with a focus on refractory metals. Niobium, molybdenum, ruthenium, antimony and tellurium targets were purchased. Technetium has no natural isotopes and was not available. Rhodium sputtering targets were not available in the time frame and the budget for the work.
6. Tellurium and antimony have low melting temperatures and vapor pressures that pose a risk of contaminating low vacuum systems. To avoid the risk, a Denton DV-502A High Vacuum Evaporator was used to coat the tips instead of the sputtering machine. The main drawback was the poor control of coating depth.
7. Although the noble metal tips are noble in a molten salt, when exposed to air or moisture, they will slowly oxidize and the sputter coating will be lost over time. Molybdenum in particular had a noticeable loss when coated cantilever tips of about 6 months in age were examined. To minimize this effect, the cantilevers were used immediately after sputter coating.
8. Sputtered depths were calculated at the Moodera Research Group by using x-ray reflectometry for calibration of their system and target geometry. For the cantilever tips that were evaporator coated, a Bruker DXT Stylus Profilometer measured the depth on glass slides that were simultaneously coated alongside the tips.

#### 4.2.1 Specific AFM Cantilever Information

Two types of AFM cantilevers were used. With the exception of the initial batch with molybdenum particles, all were functionalized with nominally 4.09  $\mu\text{m}$  diameter  $\text{SiO}_2$  spheres in the same manner as described above. The first type was used in the Asylum Research MFP-3D AFM. This set included Bruker (tipless) probes in three nominal cantilever strengths: 0.1 N/m, 0.6 N/m and 8.9N/m. The 0.1 N/m probes were triangular shaped and were made of silicon nitride. These cantilevers were only used in the first batch with molybdenum tips as it was quickly determined that our measurements would need a stiffer cantilever. The other two stiffer cantilevers were straight and made of silicon. The second type of cantilevers were NanoSensors TL-FM tipless silicon straight probes with nominal force constants of 3.3-5.1 N/m. These



types of cantilevers have alignment grooves on the cantilever chip that matched the grooves of the ezAFM. Photographs of functionalized, pre-sputtered cantilever tips are shown in figures 5.4, 6.4 and 4.1. High resolution SEM images like that in figure 4.2, provided visual confidence that the silica spheres were smooth and had good sphericity.

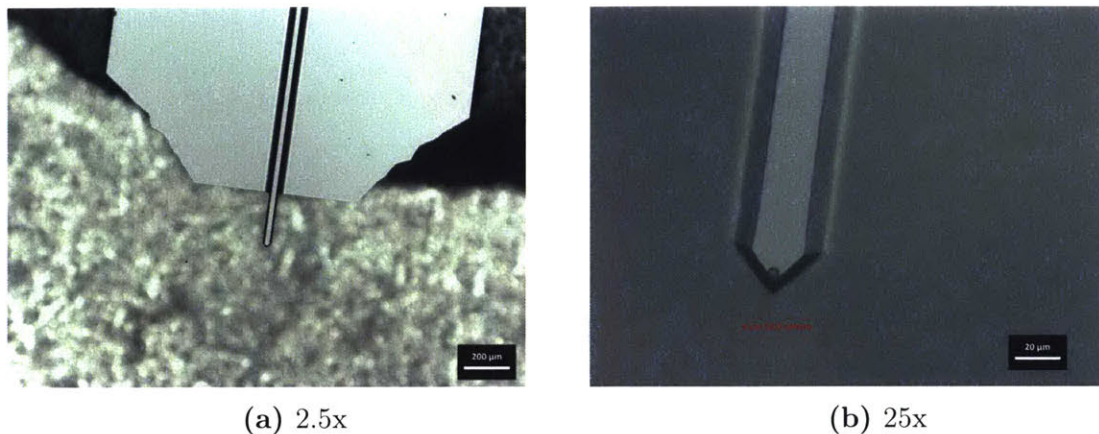


**Figure 4.1:** Pre-sputtered AFM cantilever with 4  $\mu\text{m}$  diameter  $\text{SiO}_2$  sphere attached. Picture (a) is at 2.5x (camera) optical magnification, and (b) is at 25x.

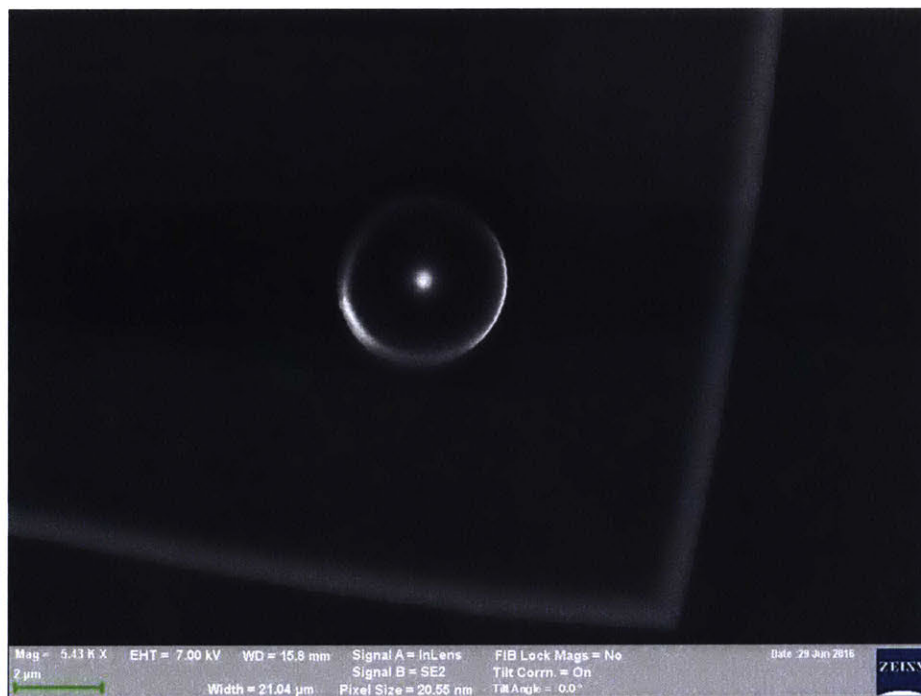


**Figure 4.2:** An SEM picture taken at 5,400X magnification of a silica sphere mounted on a tipless cantilever. The smooth surface and apparently good sphericity was important in AFM force measurements.

**Table 4.1:** Summary of noble metal cantilever tip preparation

Noble Metal	Set Number	Manufacturer and Cantilever Constants [N/m]	Sputter Depth [nm]	Notes
Molybdenum	—	Bruker (0.1, 0.6, 8.9)	N/A	[1]
Niobium	1a,1b	Bruker (0.6)	10 and 30	[2]
	2	Bruker (0.6, 8.9)	30	
	3	Nanosensors (3.3-5.1)	50	
Molybdenum	1a,1b	Bruker (0.6, 8.9)	10 and 30	
	2a,2b	NanoSensors (3.3-5.1)	50 and 100	
	3	NanoSensors (3.3-5.1)	50	[3]
	4	NanoSensors (3.3-5.1)	30	
Ruthenium	1a,1b	Bruker (0.6)	10 and 20	
	2a,2b	NanoSensors (3.3-5.1)	50 and 100	[3]
Antimony	1	NanoSensors (3.3-5.1)	456-469	[4]
Tellurium	1	Bruker (0.6, 8.9)	650-750	[4]
	2	NanoSensors (3.3-5.1)	28-32	[4]

1. These cantilever tips were the first functionalized but surface roughness and particle diameter was inconsistent. The plan shifted to sputter coating silica spheres after this point.

2. These were the first cantilever tips to have silica spheres sputter-coated. Trying to find the right spring constant, the first group of silica spheres purchased were 0.6 N/m.

3. Failed to tune on the ezAFM

4. Objective for evaporator coating was 50-100 nm, but the results were quite far off at first.

## Part 5

# Experimental Setup

The experimental plan centered around the use of an AFM to measure adhesion forces between a noble metal and clean, bare metal surfaces. This entailed construction of a chamber to support an AFM and an argon ion gun. The chamber was built to be evacuated based on the need to protect the ion gun's filament. Moreover, the evacuation was intended to assist in creating a dry nitrogen atmosphere surrounding the AFM. Equipment operation required manipulations of substrates within the environment much like a glove box and so a glove capability was crafted on the chamber. This section describes the equipment used, reports the development of the vacuum-glove-box chamber(s) and outlines the preparations of the materials subject to this study.

### 5.1 Atomic Force Microscope (AFM)

The concept of the AFM is rather simple: using cantilever spring constants and measured displacements, one can calculate force. The AFM operates at a scale with square micron areas, nanometers in vertical ( $z$ ) displacement, and nanonewtons of force. Controlled movements of the cantilever's base chip are conducted by piezoelectric motors. The cantilever's bending moment and tip position are interpreted by a photodiode measuring a reflected light signal from a laser focused on the tip of the cantilever. Electronic feedback adjusts the base height of the cantilever's  $z$ -piezoelectric motor to allow the cantilever height from the surface to change as needed by its function. The basic description of an AFM is provided in figure 5.1.

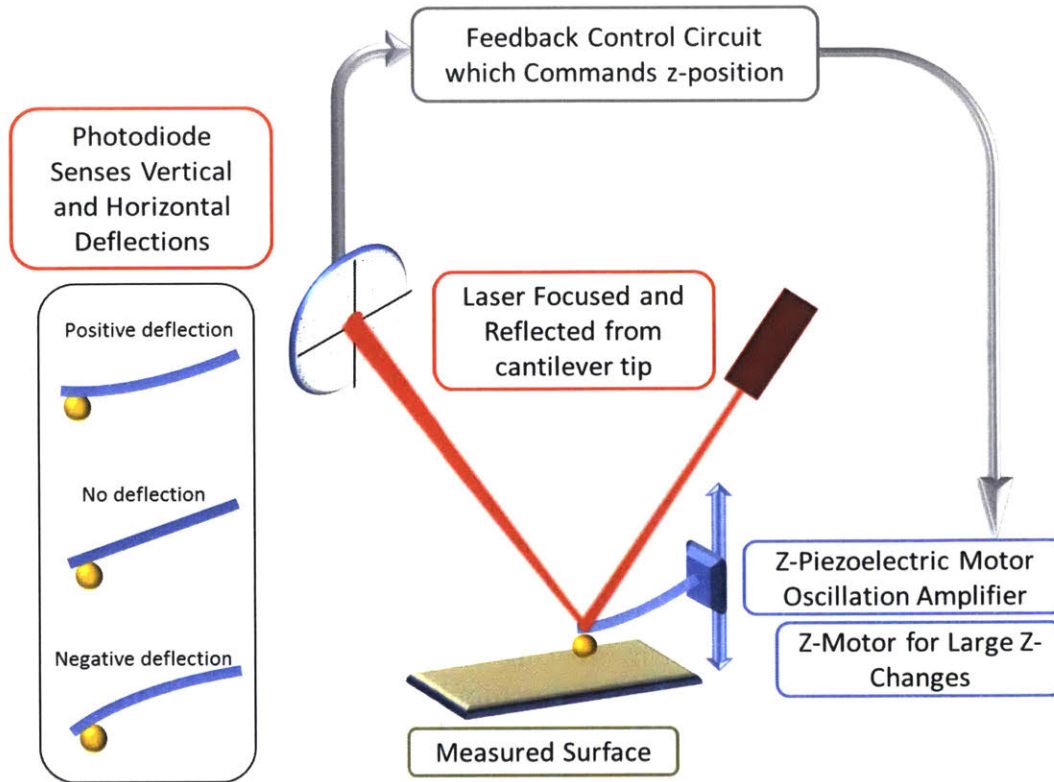


**Figure 5.1:** The basic AFM force measuring concept: (1) a particle attached to a cantilever of known or measured spring constant; (2) piezoelectric control of the z-direction movement of one end of the cantilever; (3) a laser focused on the tip of the cantilever; (4) a quadrant of photodiodes to sense cantilever deflection based on the change of the reflected light source; (5) feedback mechanism and control of the z-piezoelectric motor. The force is measured between the particle and the surface on which the particle makes contact.

### 5.1.1 Basic AFM Operations - Force Measurement

The primary function of an AFM is to measure and map the surface contours or roughness of samples by equipping sharp downward pointed probes on the end of the cantilever. These probe tips can be dragged across a surface using X and Y piezoelectric motors and the contour is measured by the deflection as the tip rides up and down the surface. Large deflections are countered by the z-piezoelectric motor such that contours could be mapped that are much greater than the cantilever's capability of deflection. This is commonly referred to as the "contact" mode. Contact mode can be destructive on soft samples. A second mode eliminates the drag issue by oscillating the cantilever near its resonance frequency and making contact by tapping the surface. The measurement is extracted from this oscillating signal. This mode is called "tapping" or "dynamic" mode.

A small deviation from the mapping function provides tip-to-surface force measurements and is called the force function. The z-piezoelectric motor first moves upward to clear the tip from contact with the surface, then moves downward to ap-

proach the surface. Near the surface, before contact is made, an attractive force would cause a negative deflection (deflection downward) and a repellent force in a positive direction (deflection upward). Once contact is made, the z-piezoelectric motor will continue to press down until a certain (automatic or operator set) upward deflection is reached and then reverse direction until the z-position returns to its normal value. The X and Y piezoelectric motors then move the tip to the next position and the force is measured again. Force measurement can be done in either the contact mode or dynamic mode. The dynamic mode offers greater functionality in conducting multiple measurements over a non-even surface and offers greater protection of the functional particle mounted to the cantilever tip. This work used the dynamic mode.

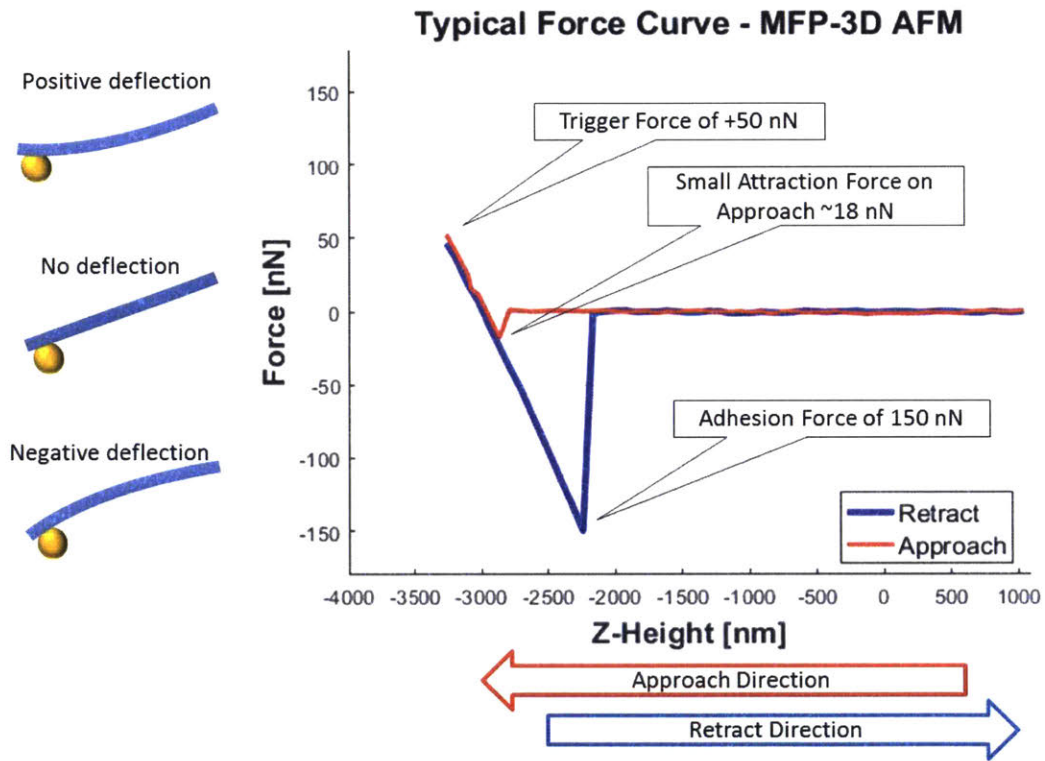


**Figure 5.2:** Depicted is a typical AFM force curve from the Asylum Research MFP-3D AFM. (1) The approach is from the right side of the picture at some positive z-value above the substrate. (2) As the cantilever is moved downward, it may experience a force (normally an attractive force in our study) and the cantilever is deflected downward. This shows up as a negative force. (3) After contact is made, the z-piezoelectric motor continues to move the cantilever downward until a positive force is applied indicated by a positive upward deflection. (4) In the Asylum Research MFP-3D, the positive force can be preset by the operator. In this case, the picture shows it to be +50 nN. (5) The AFM may hold the cantilever at the trigger force value for a predetermined length of time, called dwell time, and then begins the retraction by moving up on the z-piezoelectric motor. (6) Adhesion holds the tip creating the negative deflection noted on the curve. The maximum value achieved is the force adhesion value used in this study.

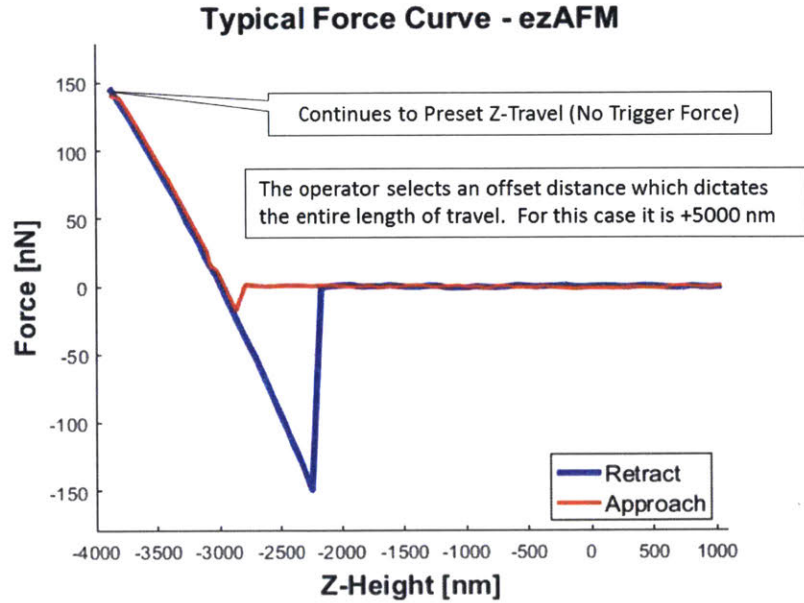


**Figure 5.3:** The NanoMagnetics Instruments ezAFM is similar in function to the Asylum Research MFP-3D AFM with a key difference on the shift from approach to retract. The MFP-3D depicted in figure 5.2 uses an operator selected trigger force and dwell time to stop the downward movement and begin the retraction. The ezAFM uses operator selected "offset" to determine total z-travel for the turning point and limits the applied force by an operator selected value for "setpoint%". Offset: from its starting point, the AFM will retract half the distance of this operator selected offset value, and travel downward to the complete offset distance. Setpoint%: to limit the tapping force, the AFM will tune down the oscillations by the setpoint percentage when contact is made. In the figure, the offset distance is 5000 nm. The setpoint% does not apply to the graph.

For idea of size, the cantilevers used were crafted from silicon chips. The dimensions of the long thin cantilever itself are  $225\ \mu\text{m}$  in length,  $28\ \mu\text{m}$  wide and  $3\ \mu\text{m}$  thick. The spring constants were in the range of 3.3 to  $5.1\ \text{N/m}$ . The silicon chip holder that is used for handling and which is gripped by the AFM is 3.4 mm long, 1.75 mm wide and approximately 0.5 mm deep. The picture of one type of alignment chip and cantilever chip are shown in figure 5.4.

## 5.2 Initial Atomic Force Microscope (AFM)

The initial measurements after preparing the noble metal cantilever tips and substrates were evaluated on an Asylum Research MFP-3D AFM in the NanoMechanical Technology Laboratory in the Department for Materials Science and Engineering at MIT. The MFP-3D AFM is an excellent tool for taking force measurements with modified probes and the results from a previous LWR crud study conducted by fellow students proved its use in the same manner. It is understood that in using this AFM,

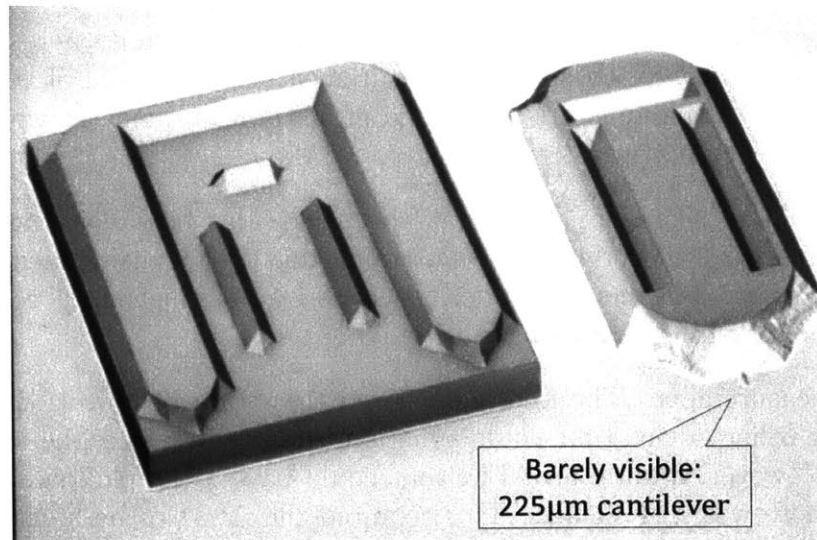


**Figure 5.4:** The glass alignment chip of the type embedded in the ezAFM head is shown on the left in the photograph. The typical backside of an AFM cantilever chip is shown on right. The cantilever is barely visible on the bottom of the chip. Photograph courtesy and permission of NanoSensors.

samples are exposed to normal laboratory air or if desired, measured in water. For the LWR study, the introduction of air (oxygen) and water are part of normal LWR conditions and as such, the corrosion layers on the structural materials after substrate preparation were not only a limiting factor, but rather an expected necessary condition. However, in an MSR, air and water are precluded and the oxide layer on those materials could be sufficiently significant to invalidate measured results. As such, a means for making force measurements upon bare metal surfaces was needed. A machine so equipped was not immediately available, so making one was the path chosen. In the sections below, the description and operations of the chamber as it was used in making measurements are discussed.

### 5.3 Design of a New Machine

The goals of leaving a bare metal surface had to begin with a look at the surface preparation phase and end with making a force measurement on that surface before extended exposure to air or water. This required re-evaluation of the methods of polishing, transport and storage, and finally measurement.

- **Surface Preparation.** Because the available mechanical and electro-polishing equipment involve aqueous processes at room temperature, the introduction of an oxide layer was inherent in this crucial step of surface preparation. Use of an argon ion gun in an inert atmosphere for final surface finishing became an essential piece in the new system. A separate ultra-high vacuum chamber was crafted for the gun's operation and is discussed in section 5.5. One drawback of

an ion sputtering process is the potential loss of uniformity across a large flat surface. However, for these force measurements, the removal of the oxide layer of a few tens of nanometers in an area of 500 mm in diameter would leave the starting surface texture largely intact.

- Transport and storage. Relocating the newly, dry bare metal surface to the AFM presented the additional constraint that the transfer mechanism must also be done in an inert chamber. This was accomplished by co-locating the argon ion polishing chamber with the AFM.
- Force measurement. The final goal posed the strictest limitation. Finding an AFM or other device that could function in an inert atmosphere was not difficult. However, finding an AFM that could have a sample loaded in an inert atmosphere was a challenge. This required the AFM to be located in a glove box or chamber where the sample transfer could occur. The resultant design was a combination glove box and vacuum chamber to house the AFM.

## 5.4 Main Chamber and the AFM

Another co-worker's project obtained a desktop/portable AFM, which was the first of fortunate events. This AFM was the NanoMagnetics Instruments ezAFM. At the same time, a decades-old, discarded vacuum chamber was fortunately made available from its basement confines for this project. The chamber and ezAFM were a near perfect fit.



**Figure 5.5:** The vacuum chamber in as-found condition after moving it from its basement location to the loading dock where it had seen the sun for the first time in over 30 years.



**Figure 5.6:** The initial test fit of the ezAFM in the vacuum chamber after thorough cleaning and inspection. The AFM (red) is sitting on top of a masonry slab and vibration reducer (black).



The chamber's exterior dimensions are 30" w x 24" h x 24" d with access ports on all six sides. The frame of the chamber is 7/8" thick stainless steel with 1/2" thick aluminum panel sides and top. Two elongated sides—called the "front" and the "back"—are hinged and can act as doors. Figure 5.5 shows the back door closed and figure 5.6 shows the front door open. The bottom is equipped with a 20" diameter port with an interconnected gate valve for a 4400 watt diffusion pump that can be seen in figure 5.5. The diffusion pump and gate valve were unused for this study's experiment. One side of the chamber was fitted with a 3" diameter port that was originally designed to have a smaller chamber with an interconnecting gate valve. The gate valve was used to connect the argon ion gun chamber with the main AFM chamber.

Vacuum tests on the chamber proved the integrity was adequate down to 1 mTorr independently on all three components: the main chamber, the diffusion pump casing and the diffusion pump/chamber gate valve.

#### 5.4.1 Glove Operations and Vacuum

During familiarization training with the ezAFM (outside of the chamber), it became apparent how important visual cues are to center the sample under the AFM head. Simple limited movements would be inadequate, so a vacuum capable glove port was chosen as a key enabler. Although vacuum in the main chamber is not required for current operations, at the time of this decision, the ion gun was expected to be operated inside the main chamber. To prevent damage to the ion gun's filament, a minimum vacuum of 1 mTorr was required. Thus to prevent a differential pressure across the glove with a vacuum in the chamber, the glove port required a simultaneous vacuum drawn on both sides of the glove: interior and exterior.

There is an additional benefit to drawing a vacuum on the main chamber. Allowing components to gas off in a vacuum serves to reduce humidity and other volatile contaminants that could affect the AFM force measurements. As a result, the vacuum capable glove port is advantageous.

A second glove port was also crafted for versatility and future use should a second glove be needed. The second glove port was used as a viewport.

Use of off-the-shelf parts was maximized. The KF-Large-Flange, or ISO-KF160 standard vacuum nipple and clamp rings fit the need and size. ISO-KF160 has a 6" diameter opening and a 7" diameter outer ring. One side of the nipple could be clamped down; the other side could serve to seal the glove in the glove port. Using a standard 8" diameter cuffed glove, a successful fit test of the idea was made on an ISO-KF160 tee. Machinists at MIT's Plasma Fusion and Science Center (PSFC) machine shop provided additional ideas as well as the labor in cutting and welding the nipples and rings to meet the design. A new door was machined from aluminum

stock by a local company, Pierce Aluminum of Franklin, MA. The final concept of the glove port is shown in figure 5.7.

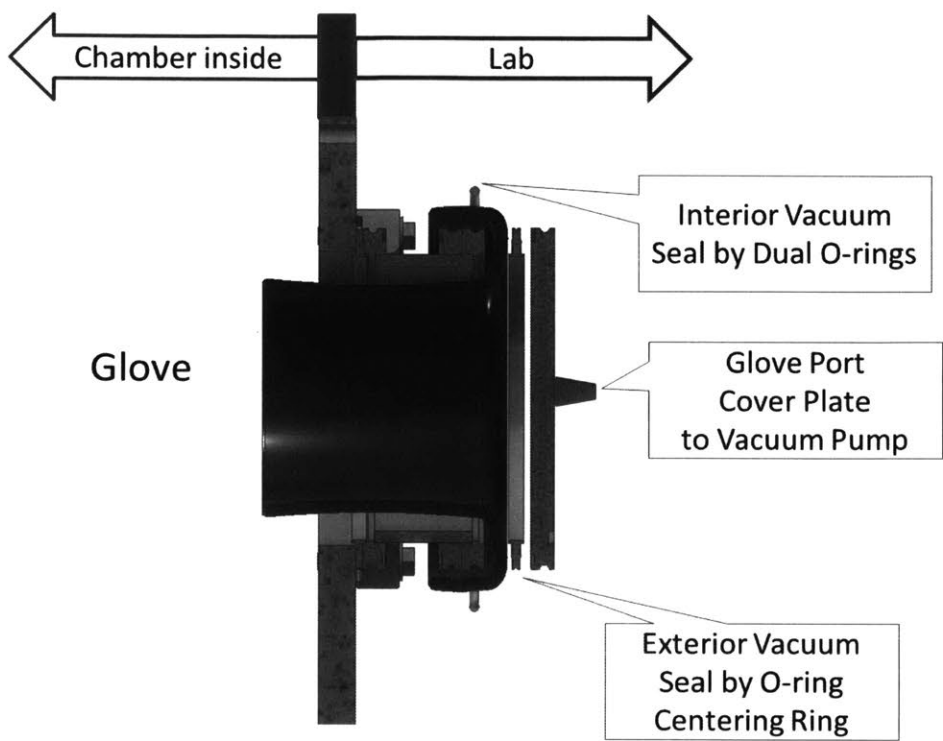


**Figure 5.7:** The glove port that can be sealed from two sides. The seal for the interior of the chamber is achieved by two tightly fitted bands (large O-rings) that go around the glove and land in the glove port's two external grooves. The seal from the lab side (exterior to the chamber) is achieved by a modified ISO-KF-160 centering ring clamped between the glove over the glove port's exterior surface and an ISO-KF-160 port cover. A vacuum pump connection was inserted into the cover to draw a vacuum on the glove prior to drawing a vacuum inside the chamber.

The external cover of the glove port was fitted with a National Pipe Thread (NPT) hose nipple. The hose from the cover went to a tee where one branch was to a small roughing pump and the second branch to equalize with the main chamber. The intent was to draw as much air from the glove before putting the chamber under vacuum. The equalizing valve was to prevent an external leak from inflating the glove once a vacuum was drawn. The system can achieve vacuum levels of approximately 10 mTorr on both the main chamber and the glove port with the main chamber pump running.

Using a 3/4" thick, 10" diameter borosilicate glass disc, a viewport was placed on top of the box. Additionally, the second glove port was fitted with borosilicate glass as a second viewport. The second viewport is seen in figure 5.8.

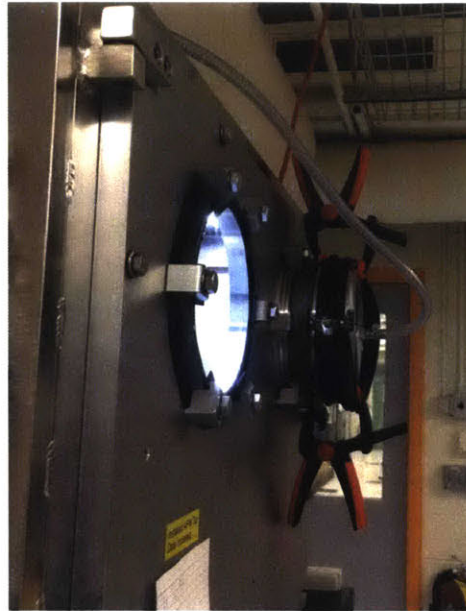


**Figure 5.8:** In the photograph, the glove port is configured with the cover to enable a vacuum to be drawn on the glove (through the cover) while simultaneously drawing a vacuum on the chamber. The viewport in place of the second glove port can also be seen.

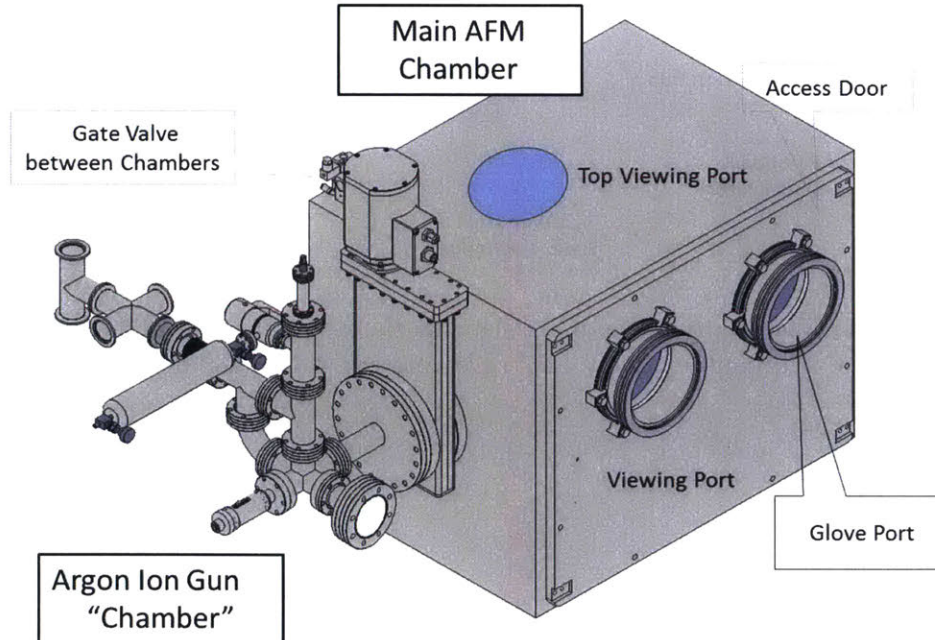


**Figure 5.9:** The main vacuum capable glove box shown with the major connections and components. Not shown: the vacuum pump, the nitrogen supply line, and the vacuum gauge lines on the underside of the chamber.

## 5.5 Argon Ion Gun Chamber

Fitting the argon ion gun in the chamber and developing the correct feed-through ports for the cabling and argon were deemed too risky and so a separate chamber was built alongside the main chamber. The side port could be used to transfer a newly polished substrate into the main chamber. Moving the gun external to the main chamber by using this small port vastly simplified the piping and cable requirements needed for the argon ion gun and significantly improved the access and ability to operate the gun.

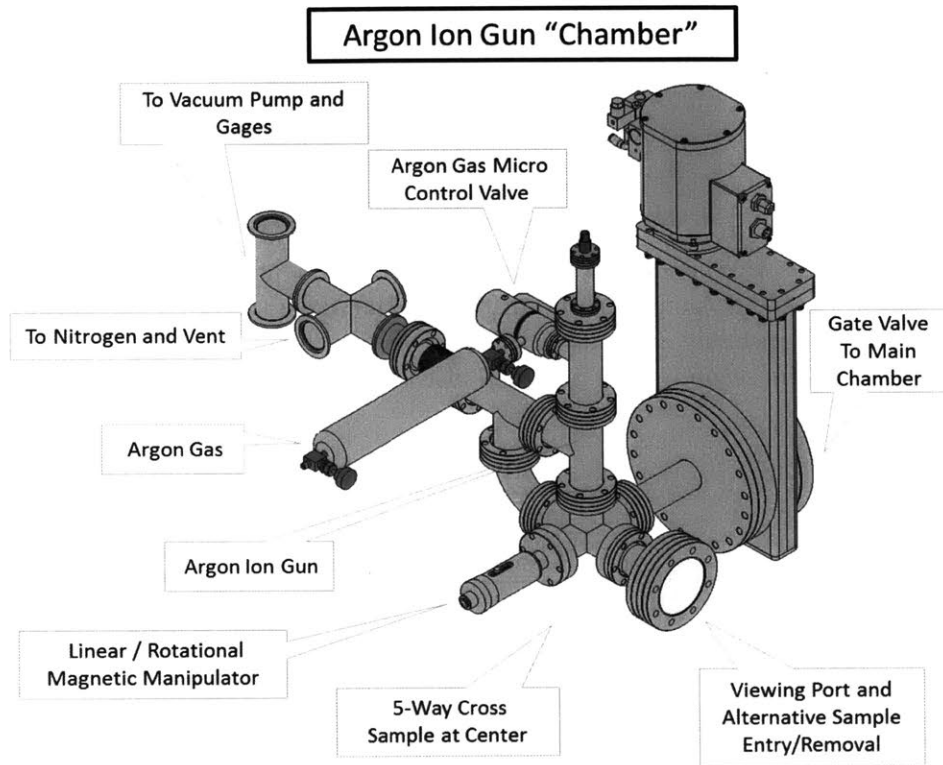


**Figure 5.10:** The argon ion chamber showing the key equipment and connections. The magnetic manipulator has a 12" travel and can rotate 360 degrees.

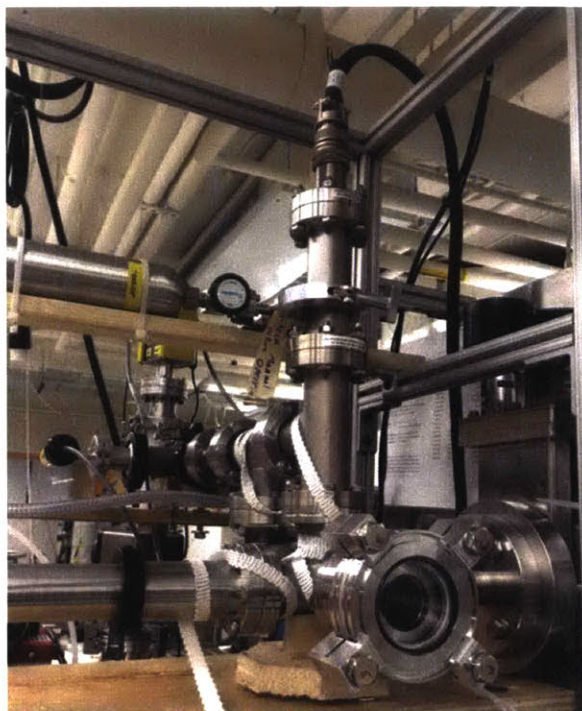


**Figure 5.11:** A photograph of the completed argon gun chamber.

The chamber was essentially a system of 2-3/4" vacuum connectors, tees and crosses. The argon ion gun was situated above and focused downward into a 5-way cross. The center of the five-way cross served effectively as the "chamber" where a substrate would be placed to be sputter polished.

Viewing the cross from the position of the operator, the top was for the argon ion gun; the front was a glass viewing port using an ISO-LF-63 fitting so that it could also be used as a small door if needed. The right side was connected to a gate valve that separated the argon ion gun chamber with that of the main chamber. The left side was the linear-rotational magnetic arm with a 12" travel that could move the substrate from the center of the cross into the main chamber. The back was connected through a series of tees to the vacuum pump, the ion convection gauge, the thermal vacuum gauges and the nitrogen supply.

The model IG70DP-LV1 argon ion gun and its controller were purchased from OCI Vacuum Microengineering, London, Canada. Using the maximum power of the ion gun of 3.0 keV with an emission current of approximately 20 mA worked well in sputter polishing the substrates. The gun is equipped with a small separate argon tank and a sapphire seated micro control valve for precise argon flow. The largest opening of the gun's focusing iris provided a sputter spot size of approximately 0.5 cm diameter on the substrate surface. The gun chamber was equipped with a separate turbo vacuum system enabling operations in its normal range of 1 to 10  $\mu$ Torr on both the gun filament and the sputtering surface.

## 5.6 Gas Management

Dry laboratory pure nitrogen (99.99%) was used as the environmental gas. From a decommissioned glove box, a GE OxyIQ oxygen sensor and a Teledyne 8800T Trace Moisture humidity sensor were obtained and installed to monitor the environment following a vacuum backfill operation. The sensors gave immediate indications if the system experienced leaks or other line up issues in backfill operations.

## 5.7 Specific Additional Equipment of Note

1. Substrates were mounted on stainless steel 304 (SS304) coupons 1" x 2" in size. The ezAFM's sample platform magnetically (firmly) holds samples in place when they are mounted on the steel coupons provided by the AFM's manufacturer. SS304 was selected and used specifically because the normal steel coupons were too strongly adherent to the ezAFM's sample holder and manipulations inside a glove box could not be easily done. SS304 is weakly paramagnetic and the coupons have sufficient magnetic attraction on the circumference that they could be easily moved on the ezAFM stage and could be picked up with a manual magnetic tool staged inside the chamber. Further taking advantage of this property, magnetic mounts were made for the end of the linear/rotational transfer arm. The coupons were easily moved on and off this mount while still sufficiently adherent so they could be rotated while under the argon ion gun without the sample falling off.



**Figure 5.12:** A test sample mounted on an SS304 coupon was placed on the stage where it was lightly held by the stage magnets. Tests were run to verify a rough centering alignment could be performed using a glove and a handheld mirror. The stage center would be moved for a more precise positioning.

2. Numerous pressure gauges were added for monitoring and backup on both chambers. For the argon gun chamber, an InstruTech Hornet IGM401 hot cathode Bayard-Alpert ionization vacuum gauge module coupled with a CVG101 convection Pirani vacuum gauge sensor was used. The argon ion gun chamber could

be monitored in a range from atmospheric pressure to  $1 \times 10^{-9}$  Torr (although the working vacuum was 3 orders of magnitude less at  $1 \times 10^{-6}$  Torr). Two mechanical backup vacuum/pressure gauges and one Teledyne DV-6M thermocouple vacuum gauge were added to monitor roughing pump performance and the vacuum in the glove box port.

3. Besides the AFM and its vibration reducer, the chamber was equipped with
  - (1) A glass vacuum desiccator for holding cleaned samples in dry nitrogen;
  - (2) tethered plastic forceps for handling the coupons with substrates;
  - (3) tethered magnetically tipped tools that could be used to pick up dropped coupons;
  - (4) magnetically tipped stay-put tools with bendable shafts to be used as a hanger/holder of coupons if needed;
  - (5) fixed wedges with magnetic pickups that could be used to push and elevate flat coupons so they could be gripped by the forceps;
  - (6) a handheld mirror; and
  - (7) LED lighting.The main chamber door was opened and exposed to atmosphere as few times as possible, but primarily for the change-out of AFM cantilevers. Following use, the chamber is pumped down and backfilled with dry nitrogen to minimize moisture and atmospheric contaminant adsorption on chamber surfaces and interior equipment.

## 5.8 Operations

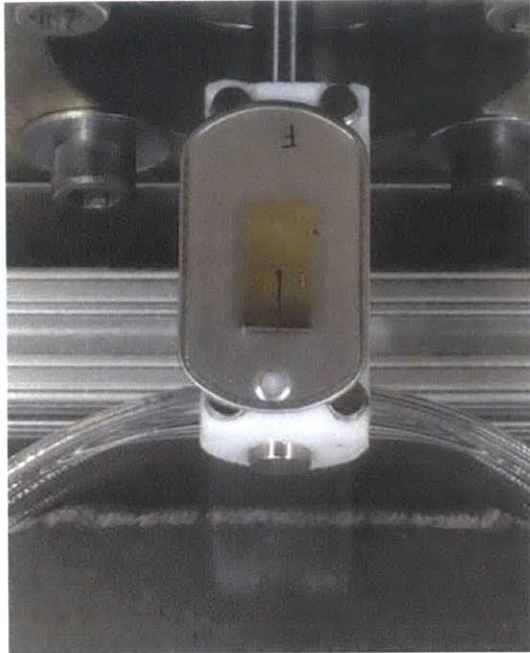
A brief description of the end-to-end operation illustrates how the measurements were normally taken.

**Evacuation and Backfill** The glove port would be evacuated with its own roughing pump to remove as much air/gas from the glove prior to evacuation of the chamber. It was at first expected that the glove port would be less leak tight than the main chamber, but that proved to be untrue. The main chamber would twice be evacuated to approximately 1-7 Torr and filled with dry nitrogen to help purge the chamber. Then the chamber would be evacuated to 10-30 mTorr to evaluate gassing off of any newly added equipment. Normally, that level would be held for approximately 1 hour and then dry nitrogen would be backfilled to slightly above atmospheric pressure so an oxygen and humidity sample could be taken. These values were used not for quantitative purposes but rather to evaluate potential leaks. Following satisfactory results, the glove port cover would be carefully removed mindful that a pressure inside the chamber could blow the glove outward. To balance the pressure on the glove, throttling the cutoff valve connecting the roughing pump and the chamber would slowly pull the pressure inside the chamber to equal that of the lab. Adding nitrogen or drawing a vacuum would be done as necessary to maintain the pressure balance between the main chamber and the lab. This process was particularly useful when small main chamber pressure changes would occur when operating the gate valve for transferring items in and out of the argon ion chamber.

**Sputter Cleaning Substrates** Sample loading and unloading. There were two means of introducing samples under the argon ion gun. The main mechanism was through the side port gate valve in the main chamber. The magnetic linear manipulator would push the sample holder into the main chamber where the sample would be emplaced. The holder, the SS304 coupons and the samples were all conductive so an electrostatic charge would not build on the sample during polishing. The transfer could be conducted with the main chamber open or closed. The glove had sufficient dexterity and reach to be able to conduct the loading and unloading. The sample would be then retracted and situated under the gun. The operator, looking through the ion gun chamber's viewport, would make final adjustments to position (and angle if desired). The second means of loading the sample would be to remove the argon ion gun's viewport and slide the sample directly onto the holder. The sample and holder could also be rotated to face the viewport during sputtering for a visual verification of alignment without having to either unload the sample or even shut down the gun.

Gold sputtering. One additional unusual step was taken of sputtering 40 nm of gold on the samples before mounting on 1"x2" stainless steel 304 coupons. The purpose of the gold was to provide a visual clue to the sputtered area and to help calibrate the sputtering gun. The intent was to examine the substrates on a quantitative argon sputtering depth-profiling machine using X-ray Photoelectron Spectroscopy (XPS). The rate of gold disappearance could be determined on this newly built machine and compared with the gold and oxide film removal quantitatively measured on the XPS machine.





(a) Pre-sputtered F91 sample



(b) Post-sputtered F91 sample

**Figure 5.13:** The left photograph is an F91 sample mounted on an SS304 coupon held magnetically on the holder of magnetic linear-rotational manipulator inside the main chamber. The sample was staged for retraction to the argon ion gun chamber. The right photograph is the same sample after sputtering and being returned to the main chamber. The photographs were taken through the upper viewport

Once sputter cleaned, the argon ion chamber would be backfilled with dry nitrogen. The main chamber would also be under dry nitrogen before the sample was re-introduced. With pressure equalized, the gate valve between both chambers would be opened. Once introduced into the main chamber, the sample would either be placed on the AFM stage or stored in the glass desiccator container in the main chamber.

## 5.9 ezAFM AQUA

The ezAFM is a simple-to-operate AFM that was considered suitable for the use in the chamber. It was the model of the demonstration AFM provided by the manufacturer for use during familiarization, fit up and training. The ezAFM AQUA was the model purchased and was similar in almost all respects to the demonstration model except for modifications to allow the cantilever tip to work in water. One useful modification is the centering ring upon which the AFM head is situated. The ring returns the AFM head to a centered location removing the uncertainty of its x-y (horizontal) position. Without the ring, proper sample alignment would have been exceedingly difficult to achieve using a glove and viewport. On the negative side,

the optics are calibrated for water and experience a loss of signal strength in air. Weakened signal strength of the laser presented a problem with marginal cantilevers. The features and operations of the ezAFM AQUA are highlighted and the optical issue is discussed below.

1. AFM cantilevers with alignment grooves fit into an alignment chip in the AFM head so no further adjustments are deemed necessary. Although, these chips are not as common as others on the market, the NanoSensors TL-FM tipless cantilevers suited this study.
2. A glass microscope slide is cleaned using methanol and is used as the starting substrate for testing the functions of the AFM.
3. The AFM head is centered by fit over a stage equipped with a motorized x-y platform. The platform has permanent magnets that hold substrate coupons in place. From the laptop computer, the stage can be moved in 1 to 1000  $\mu\text{m}$  increments in the x or y directions. For this work, different areas of the substrates were examined by this motorized stage.
4. Once the cantilever is in place and the head centered over the glass slide, all operations are software driven and the chamber door can be closed. The chamber is then evacuated, purged and a dry nitrogen atmosphere is established before turning on the AFM.
5. Optical camera. The AFM has an optical camera focused at the spot where the cantilever is expected (225  $\mu\text{m}$  from the edge of the chip). This camera helps the operator recognize any misalignment (or loss of a cantilever) that may have occurred while loading the cantilever. The laser spot on the cantilever and some of the interference patterns from reflected laser light off of the substrate surface can be seen in the camera's image on the laptop computer. When the cantilever tip is near the surface, the camera can show major defects on the sample. The operator has a limited ability to change the focal length by a few microns with a software slide bar. In air, the surface remains out-of-focus at the maximum focal length of the camera. In water, the surface can be plainly seen. However, the focus is sufficient to see if a scratch or an occlusion is in the vicinity of the tip. If so, the tip can be raised and the substrate moved to a different location.
6. Laser power is operator adjustable. Too much power may cause overloading the photodiode or may cause scattered light to be of sufficient magnitude to affect the photodiode input signal. For these measurements in air, the laser power was normally set between 40 to 70% to optimize the signal.
7. Tuning is automatic. The AFM will scan through a series of frequencies, produce a graph to show the cantilever's harmonic frequency and automatically select the optimal tuning frequency. It is from this frequency that the spring constant is calculated and the optimal tapping frequency in the dynamic mode is chosen. The automatic selection can be overridden by the operator but was

not found to be necessary in this study. Many cantilevers had problems at this particular step. The AFM uses part of the reflected laser signal, called the oscillation amplitude, to determine the oscillations of the tip. In turn, it uses changes in the oscillation to determine proximity to the surface. If the oscillation amplitude is too weak, the oscillation frequency cannot be determined. However, more often during this work, the signal was of sufficient strength to determine the cantilever's harmonic frequency, but too weak to accurately keep track of the tip's position. This is a key internal feedback signal for the AFM. For normal cantilevers, the weakened signal is acceptable in conducting force measurements. However, for cantilevers that have been mechanically altered with the weight of the sphere and the sputter coating of surfaces, the signal was often so tenuous the AFM was unable to achieve adequate signals for tuning and use. In particular, none of the ruthenium coated cantilevers worked in the ezAFM AQUA. Further discussion regarding cantilever problems will be addressed in part 6 on results.

8. The z-piezoelectric motor has a small range (on the order of 6000 nm). To move the cantilever the millimeter distances to get to the surface, a mechanical motor inside the AFM head is used. Landing the tip on the surface uses this motor. In automatic mode the tip is slowly lowered until the oscillation amplitude detects the surface at which time the motor stops. The image from the optical camera also changes as the laser pattern on the back of the cantilever changes when it is flexed on landing.
9. Once landed, AFM measurements can be taken. For this study, all measurements were taken in dynamic mode. If no problems arise, force measurements are obtained with the following sequence of events:
  - (a) The first key operator selected value is offset, which is the length of z-travel imposed by the AFM z-piezoelectric motor. For offset, ranges from 3000 nm to 5000 nm were used. The AFM would start a measurement by moving up by half the offset value and then moving downward the length of the offset before retracting. A short offset would be ideal if the location of the surface at every sample point had the same precise height. Unfortunately, because the samples always experienced some slope (as mounted on the sample coupon and AFM stage), the height difference between measured points on either side of the grid could be 5000 nm or more. As such, when taking a series of samples over a large distance for example, the beginning point might be close the surface and the end point of the grid might start far from the surface. This effect can be seen on an eight-sampling-point graph shown in figure 5.14.
  - (b) The second key operator selected value is setpoint%. Setpoint% determines the tapping force and was set normally to 30%. A lighter tapping force (higher percentage) often resulted in the failure of the AFM to recognize

- the surface due to the already weakened signal. A higher tapping force (lower percentage) risked tip wear or loss of signal fidelity.
- (c) Single force measurement. A single force measurement is taken to verify the tip is in close proximity to the surface and the settings are correct.
  - (d) Surface scan. For the *ezAFM* to conduct a survey of multiple points, a scan of the surface is first required. Typically, a  $15\ \mu\text{m} \times 15\ \mu\text{m}$  scan is used or a  $25\ \mu\text{m} \times 5\ \mu\text{m}$  scan is used if the slope is excessive.
  - (e) Grid scan. One hundred grid points are selected. A  $10 \times 10$  or  $25 \times 4$  grid was used dependent upon the geometry of the previous surface scan.
  - (f) Relocate and repeat the force measurements. The tip is raised and the substrate moved to sample a second area. Normally the movement is on the order of  $250\ \mu\text{m}$  in X, and  $250\ \mu\text{m}$  in Y. The distance is far enough to gain a representative sample yet remain confidently within the sputtered area of the substrate. The optical camera helps verify no major defects exist at the new location.

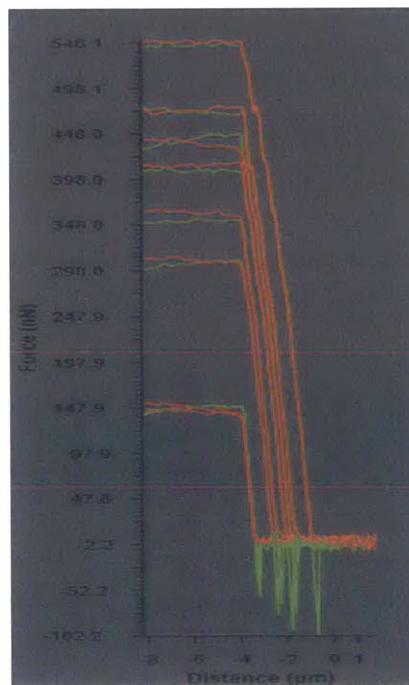


**Figure 5.14:** A measurement taking 8 samples over a  $15\ \mu\text{m} \times 15\ \mu\text{m}$  grid shows how a small change in slope or change in height of the sample changes relative z-height of the start and end of the approach (and retract) curve.

## Part 6

# Experimental Results and Conclusions

Data was collected in two phases. The preliminary phase was intended to verify methodology and to scope out the experimental plan. For example, from previous crud studies for LWRs, the concept of using the AFM for particle-to-substrate force measurements was familiar. For this study, yet unknown was the expected range of adhesion forces in which to choose the AFM cantilevers with appropriate spring constants. The second phase was intended to collect the data with sufficient consistency to make direct comparisons. The original intent was to continue to use the same AFM throughout the study. However, a question regarding the oxidation of the substrate materials and the impact of small but important layers as discussed in section 2.3, changed the direction of the experiment. A second (portable) AFM was used in a vacuum chamber / glove box for the data collection. Although there were significant differences between the manners in which the forces are applied by the two AFMs, some useful inferences in comparing the two sets of data could be made.

### 6.1 Preliminary Measurements

The first series of data was taken on the MFP-3D AFM in an exploratory phase of this work. Not all the noble metals nor the substrates were represented during this phase. Collection was made using niobium, molybdenum, ruthenium and tellurium coated cantilever tips. The substrates evaluated were Hastelloy-N, SS316L, Ni-201 and molybdenum. Selection of these particular materials to measure (or not to measure) was not a deliberate decision. Rather, the selection followed the parallel preparation of cantilever tips and substrates during this period.

The goals of the first measurements were:

1. Seek preliminary values of adhesion forces with available cantilevers and substrates to determine the correct AFM cantilever spring constants to use in data collection.

2. Find appropriate trigger forces to apply. The trigger force is the AFM generated force applied during the approach phase between the cantilever tip and the surface before retraction begins.<sup>1</sup> While a consistent trigger force was desired for data acquisition, a value at the lower end of the range was desired to minimize tip wear and cantilever fatigue.
3. Find an optimal dwell time in measuring the adhesion force. Dwell time is the duration of time the trigger force is applied.<sup>1</sup> For consistency, a standard dwell time like a standard trigger force was desired.
4. Verify the durability of the sputter coated silica spheres for repeated measurements on many substrates.<sup>2</sup>

A summary of the data collected in the preliminary phase is provided in table 6.1 and plotted in figure 6.1.

Goals in this exploratory stage were largely satisfied prior to shifting to a different experimental setup.

1. The initial nominal cantilever spring constants for the molybdenum particles were 0.1 N/m, 0.6 N/m and 8.9 N/m. Although these cantilevers were eventually considered inappropriate for the remainder of the experiment, they served to show that the 0.1 N/m cantilever spring constant was likely to be too weak. The indications on the AFM software were an "input overload" warning and abnormally large oscillations between contact points. When the decision was made to purchase cantilevers for mounting silica spheres, 0.6 N/m cantilevers were first selected for sputtering.

As the initial data of the sputtered cantilevers began to materialize, it became clear that stronger spring constants were needed for at least some of the combinations of materials. For example, 0.6 N/m niobium tipped cantilevers on SS316 exhibited "input overload" and maximum deflection or zero deflection on nearly every measured point. The histogram of figure 6.2a shows the behavior. As a result, some plots could be misleading. In figure 6.1, the data point for niobium on SS316L is shown at about 280 nN after removing all the zero points. The point is really reflective of a "greater-than-280-nN" adhesion force. However, since the cantilever itself was limited, no higher value could be measured (nor could be represented on the plot). Niobium coatings were the first set to be made and at the time, only 0.6 N/m cantilevers were on-hand for sputter coating. The 0.6 N/m ruthenium tipped cantilevers were adequate. The 0.6

---

<sup>1</sup>Trigger force and dwell time are operator entered options on the MFP-3D AFM (the preliminary AFM), but were not options in the ezAFM (the second AFM).

<sup>2</sup>During the training phase, the first tips used were molybdenum particles attached to bare cantilevers. Large inconsistencies were observed on both a polished nickel sample and on a glass slide (calibration reference). Closer examination found poor sphericity and multiple asperities on the particles and a shift to using silica spheres was made.

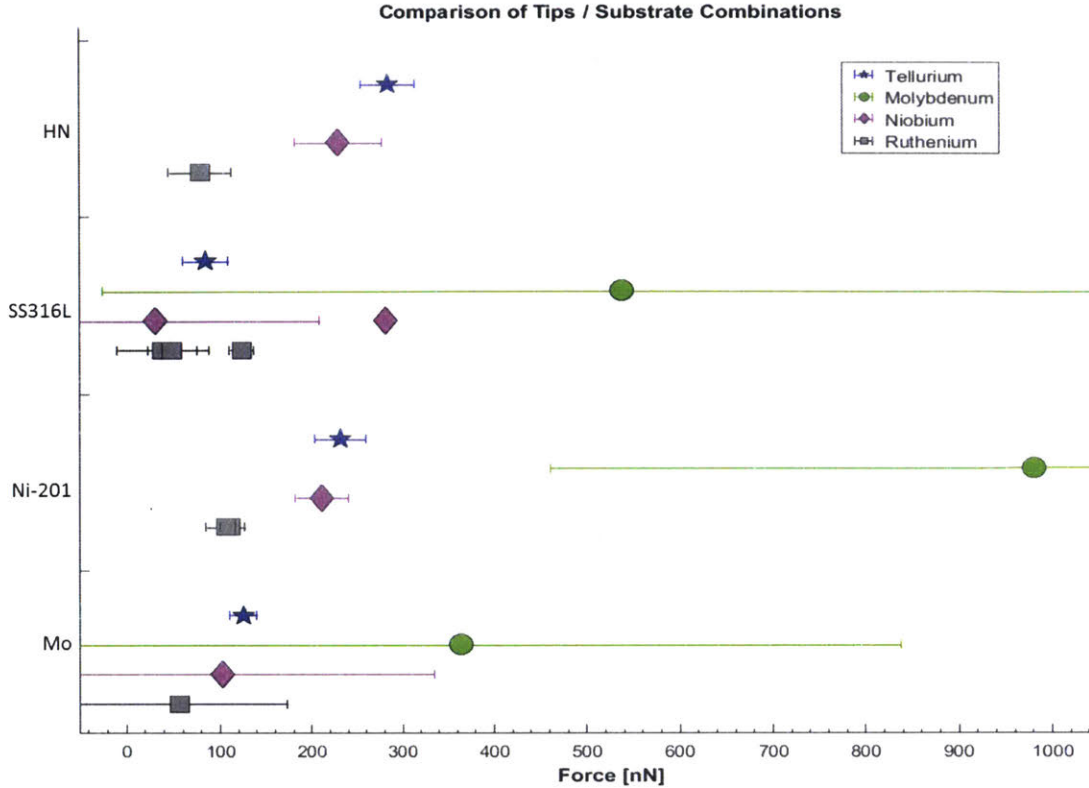


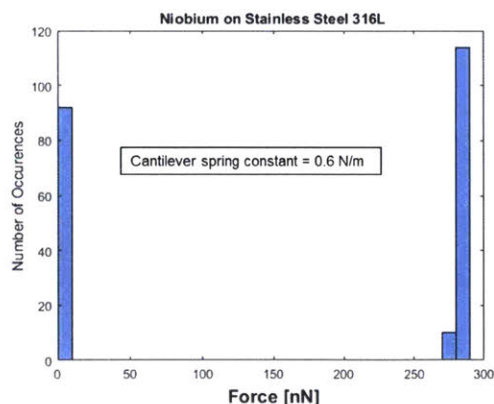
**Figure 6.1:** This figure provides a pictorial summary snapshot of the data collected while scoping the experiment and verifying processes. Hastelloy-N, SS316L, Ni-201 and molybdenum are separated by banded shades of gray. The colored shapes represent the mean of the forces by each tip: niobium - magenta diamonds, molybdenum - green circles, tellurium - blue stars and ruthenium - gray squares. The colored bars represent 2 standard deviations from the mean. Not all substrates nor noble metals were measured during this period. The force measurements were taken in air at room temperatures on the same machine – the MFP-3D AFM. Variations in cantilever force strengths, applied strength and dwell times were evaluated during these measurements.

N/m molybdenum cantilevers were not used.

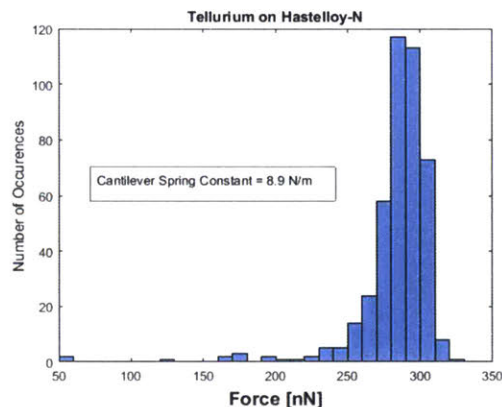
The last sets of cantilevers purchased for this phase of the study had 8.9 N/m spring constants. For the remainder of the study, none of these cantilevers exceeded their input limit.

Based on these preliminary results, the purchase of the cantilevers for the ezAFM were made with nominal cantilever strengths of 3.3 to 5.1 N/m. Those cantilevers proved to be of adequate range.<sup>3</sup>

<sup>3</sup>The ezAFM required cantilevers with alignment grooves and selection of tipless cantilevers with the grooves was limited. Fortunately, the cantilevers were available that met the range of needs for this study.



(a) Understrength cantilever

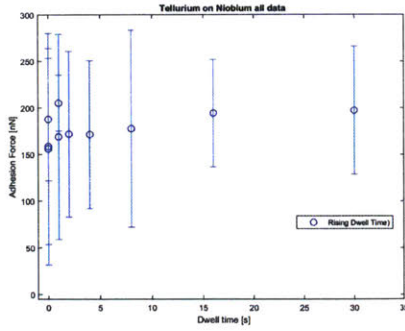


(b) Within cantilever range

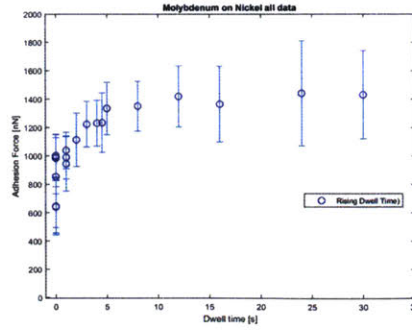
**Figure 6.2:** The histogram on the left shows that the cantilever reached its maximum deflection that could be measured by the AFM (if adhesion was at all measured). In this case, the adhesion force is "greater than" 280 nN. The cantilever spring constant was 0.6 N/m. Results such as these suggested a strong spring constant was warranted. The histogram on the right shows the 8.9 N/m cantilever well within range.

2. The values of trigger forces attempted ranged from 5 to 135 nN. After experimenting, the value of 15 nN appeared normally adequate and achieved the most consistent results. For most of the data, a 15 nN trigger force was used.
3. Dwell times ranging from 0 to 60 seconds were explored. With the exception of molybdenum tips, dwell time did not appear to change the result in any significant way or with any consistency. However, more sampling would be required to better make a statistical determination. An example of a force versus dwell time curve is shown in figure 6.3. Since neither trigger force nor dwell time were options with on the ezAFm this aspect was not further pursued.





(a) Tellurium on Niobium



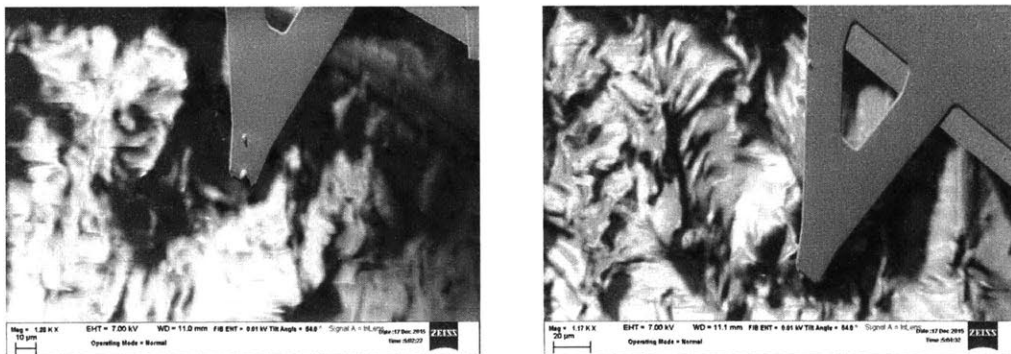
(b) Molybdenum on Nickel

**Figure 6.3:** Dwell time was used on several samples in the preliminary phase. On the left is a typical plot of adhesion force versus dwell time. The tip was tellurium, the substrate niobium. The circles are the mean and error bars plot two standard deviations. From this plot, there is no significant effect on dwell time. The right picture is the same type of plot for a molybdenum tip on nickel. This graph suggests a correlation exists between adhesion force and dwell time of the applied trigger force.

4. The sputter coating of the spheres proved adequate. In the execution of this project, dozens of cantilevers were lost or broken through handling outside of the AFM. During measurements, only one cantilever tip lost an  $\text{SiO}_2$  sphere and only one cantilever tip lost a molybdenum particle. A lost tip manifests by a complete change in force profile, such as suddenly having no adhesion where the previous points demonstrated clear adhesion forces. Following removal from the AFM, the two affected tips were confirmed to have lost their sphere/particle by optical microscope examination. SEM images were taken of an early tip failure shown in figure 6.4 where the molybdenum particle was lost. While sphere and sputter coating adhesion appeared to be durable, some of the cantilevers appeared to have possibly cracked or otherwise worn out as indicated by large changes in deflection oscillations and a subsequent inability to tune/calibrate upon investigation.

**Observations from the Preliminary Measurements** Operator selected inputs were varied during this preliminary phase. Hard conclusions regarding relative force strengths are difficult to make under these statistically poor conditions. However, a number of observations are worth commenting on here.

1. Ruthenium. For this study, the preliminary phase is the only set of data for ruthenium. All the prepared cantilevers with ruthenium for the ezAFM in the final phase failed to tune/calibrate. The reason for the failure appears to be related to a particular way a sputtered metal affects the silicon cantilevers. Some metals, such as ruthenium and molybdenum were particularly troublesome in this way. An observation from this first set of data is likely to be related. Following insertion into the AFM, a number of preliminary steps are conducted



(a) 0.1 N/m cantilever - with sphere      (b) 0.1 N/m cantilever - lost sphere

**Figure 6.4:** Pre-sputtered triangular (0.1 N/m) silicon nitride AFM cantilever with and without the molybdenum particle attached. The 0.1 N/m cantilevers are triangular. The left SEM picture shows a tip with the particle attached. The right picture confirmed a loss of the particle.

which involve aligning the laser on the tip of the back of the cantilever. Proper alignment is indicated by a near zero deflection signal. On the MFP-3D AFM, this alignment is conducted manually. For the ruthenium coated cantilevers, after achieving a zero value, the deflection voltage would not remain steady. Rather, it would drift downward (negative deflection) for up to 30 minutes. This unusual behavior was not seen with non-coated AFM cantilevers and was observed only to a small degree with the other coated cantilevers of our study. Considered was the possibility that ruthenium was causing uneven heating of the cantilever due to the laser. However, the thin (10 and 20 nm) coatings are on the opposite side facing the laser and that reason did not seem plausible. To compensate, a waiting period was invoked to allow cantilever stabilization that appeared to resolve this particular artifact. The ezAFM has no manual control or adjustment for the laser or photodiode and the ruthenium cantilevers would fail to align. To see if a similar stabilization was required, each cantilever was given a warmup time of up to 2 hours. However, all attempts to gain a tuned cantilever failed and as a result, no measurements on the ezAFM were obtained for ruthenium. Two full sets of molybdenum cantilevers had similarly failed to tune on the ezAFM. However, a third (and final) set of molybdenum cantilevers functioned. The issues with molybdenum cantilevers will be addressed in the section discussing the results of the ezAFM.

In general, the ruthenium data was reasonably consistent showing adhesion forces across the four substrates measured during this phase. The adhesion values were lower in general than the cantilever tips with niobium, molybdenum and tellurium. Figure 6.9 at the end of this section illustrates.

2. Molybdenum. The preliminary data showed the 10 nm molybdenum coated can-

tilever tips had strong adherence to the three substrates tested: SS316L, Ni-201 and molybdenum itself. Of all the samples conducted, no other measurements came close to those high values ( $>1000$  nN). These results run counter to the results of the ezAFM samples that showed molybdenum consistently on the low end. The first inclination is to believe some error was made in the set-up of the machine. This is a distinct possibility since all the molybdenum samples were collected in a single day and no other cantilevers were examined. The possibility that a single cantilever was a problem was eliminated as two different cantilevers were used during the measurements. The first cantilever had lost its sphere between substrates and had to be replaced. A second cantilever was used for the final measurement. No other molybdenum samples were taken during this preliminary phase.

3. Tellurium. The adhesion values of tellurium matched well with that taken on the ezAFM. The tellurium tips used during this first phase were made before the evaporator coating process was better controlled. The coating on these tips of 650 to 750 nm were an order of magnitude thicker than the coating thickness intended. Regardless, the cantilever tips were made and so they were used. For the ezAFM cantilevers, 30 nm thickness of tellurium was achieved. The similar results supported the decision to use a 30 nm coat as having sufficient magnitude on a  $4\text{ }\mu\text{m}$  silica sphere to achieve the experimental aim of this work.

**Table 6.1:** Mean and standard deviation for the preliminary phase measurements with the MFP-3D AFM. Tabulated values are in nanonewtons [nN]

[nN]	Niobium		Molybdenum		Ruthenium		Tellurium	
	mean	stdev	mean	stdev	mean	stdev	mean	stdev
Hastelloy-N	229.4	23.8	-	-	79.0	16.9	284.0	14.8
SS 316L								
run 1	31.4	88.8	537.7	281.5	123.7	6.51	85.0	12.1
SS 316L								
run 2	230.7	0.6	-	-	39.2	24.4	-	-
SS 316L								
run 3	-	-	-	-	49.2	13.0	-	-
Ni-201								
run 1	211.0	14.4	980.2	259.7	111.3	5.4	231.1	14.1
Ni-201								
run 2	-	-	-	-	105.9	10.6	-	-
Mo								
	102.4	116.0	364.7	236.4	57.0	58.2	125.2	7.4

1. Columns identify the noble metal tips.
2. The rows identify the substrates: Hastelloy-N, SS316L (3 runs), Ni-201 (2 runs), and molybdenum.

## 6.2 Chamber Data Collection and Results

The move to use a vacuum chamber / glove box for the AFM measurements required a different set of cantilevers to be purchased, functionalized and coated. Since the ezAFM had limited operator selected values and adjustments, standardization of the procedure was simplified. Data collection occurred all in a period of approximately two weeks, which further reduced environmental variables. Moreover, the short time-frame allowed use of the same set of substrate samples throughout. Fortunately, the sputter coating machine from the Moodera Research Group was available for preparing niobium and molybdenum cantilevers in that time-frame so these cantilevers suffered no delays from preparation to measurement. The cantilevers and substrates were prepared similarly as outlined in part 4. To maximize consistency, repeatable procedures and processes were used in the operations of the argon ion gun and the chamber atmosphere conditioning as outlined in part 5.

With the exception of ruthenium for which no data was collected, at least 200 points were measured for each tip and substrate combination. Before discussing the data handling and the detailed results, a summary of the collected data is illustrated in figure 6.5.

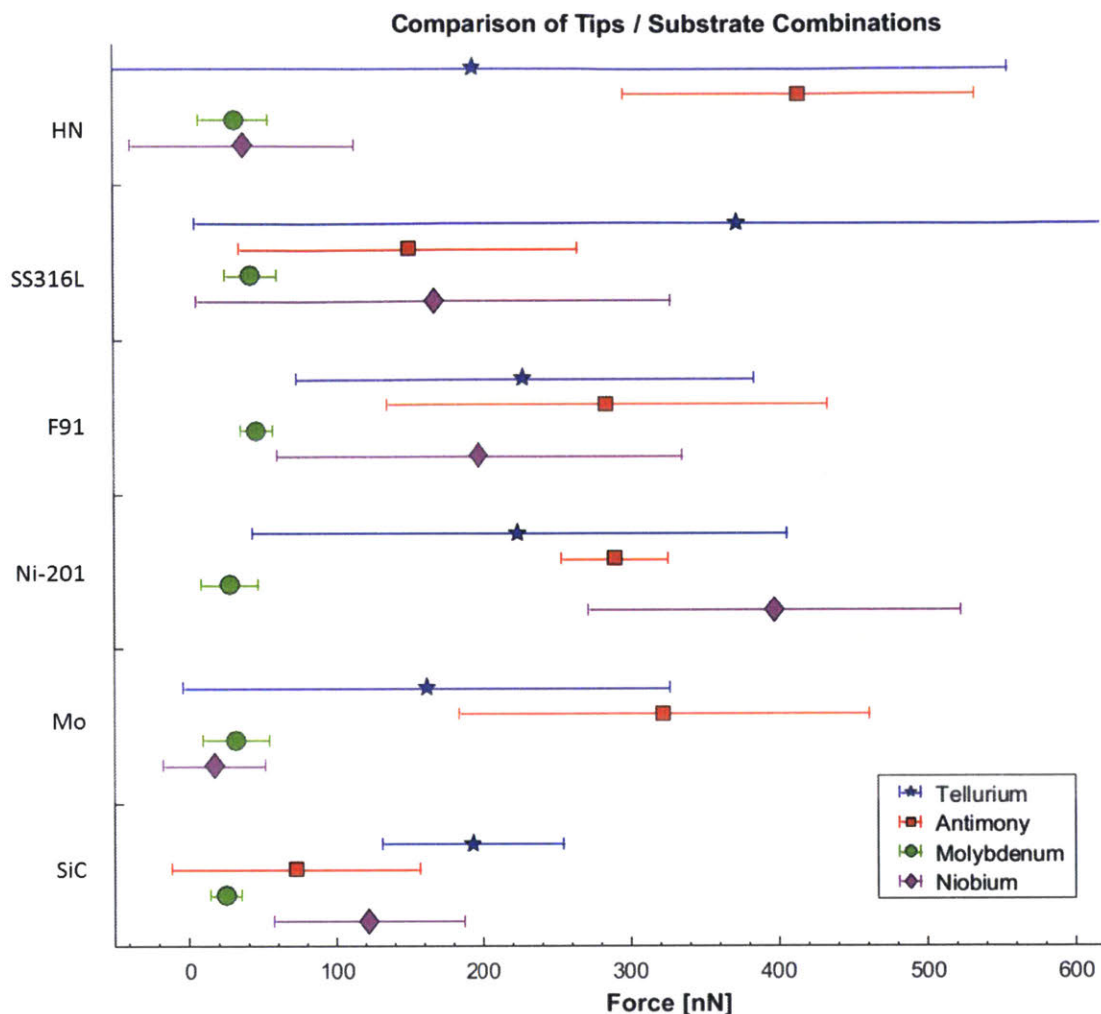


**Figure 6.5:** Summary of Data Collected from the ezAFM in the second phase of the experiment. Hastelloy-N, SS316L, F91, Ni-201, molybdenum and SiC are separated by banded shades of gray. The colored shapes represent the mean of the forces by each tip: niobium - magenta diamonds, molybdenum - green circles, antimony red squares and tellurium blue stars. The colored bars represent two standard deviations from the mean.

### 6.2.1 AFM Data

The ezAFM output is provided in text files that contain the data points for the graphs visually represented on the software screen. Each retract and approach curve consisted of 128 pairs of z-height [nm] and force [nN] values. The data of interest was the maximum negative force of the retract curve and a zero baseline as illustrated in figure 5.2 of part 5. Subtracting the two provided the adhesion force for that data point. A Linux bash script was written to average the last 10 points on the retraction curves as those values returned to toward the system zero value and subtract from the zero the maximum negative force. The script would combine the output of each of the runs in a given text file into a comma-separated value (csv) column of force

adhesion values. For a 100-point grid sample, the csv file would have the adhesion force for the 100 samples.

The next step was to evaluate the data for outliers. A single vector of data was composed for each tip and substrate composition. A mean and the standard deviation were calculated using Matlab 2016b. Data points falling outside of two standard deviations were removed. The resultant mean and two standard deviations are provided in table 6.2 and were plotted. The individual plots are provided at the end of this part.

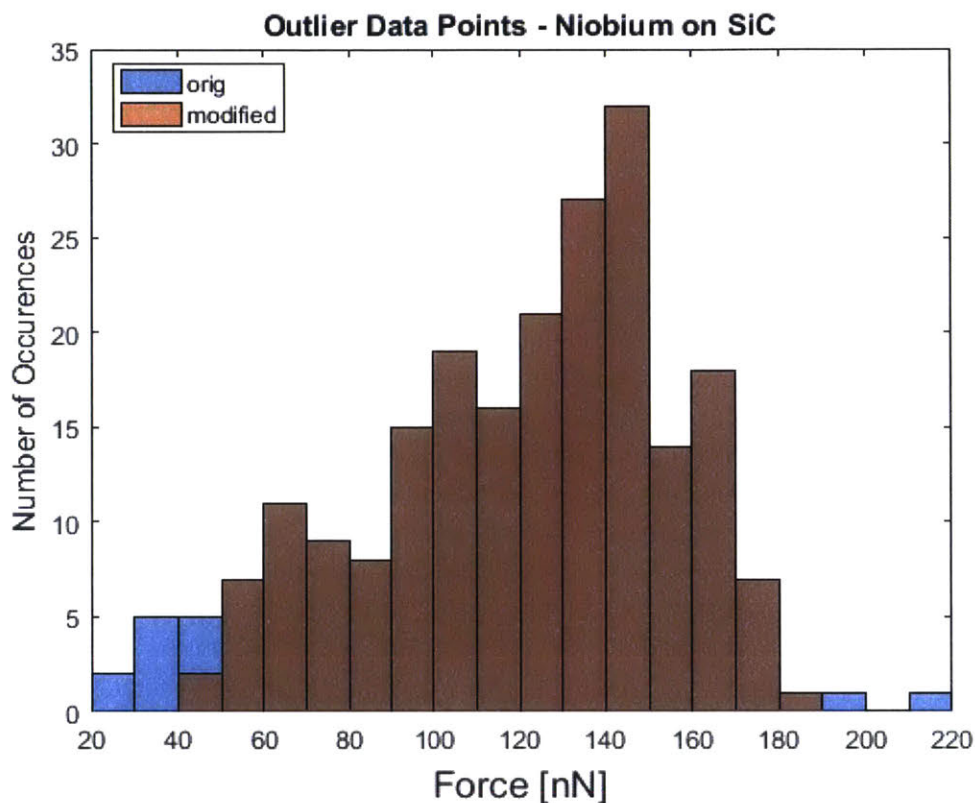


**Figure 6.6:** Niobium on SiC histogram compares the original data with the outliers removed. Original data is in blue. Modified data with outliers removed is in orange. When both are the same, the color is brown. Thus, the blue color shows the outliers removed from the original data.

## 6.2.2 Observations

### 6.2.2.1 Molybdenum

The molybdenum cantilevers were particularly challenging. The first set of cantilevers were coated with thicknesses of 50 nm and 100 nm. One question that was not adequately tested during the preliminary phase effect of coat thickness. Since molybdenum showed the strongest adhesion in the preliminary phase, any change

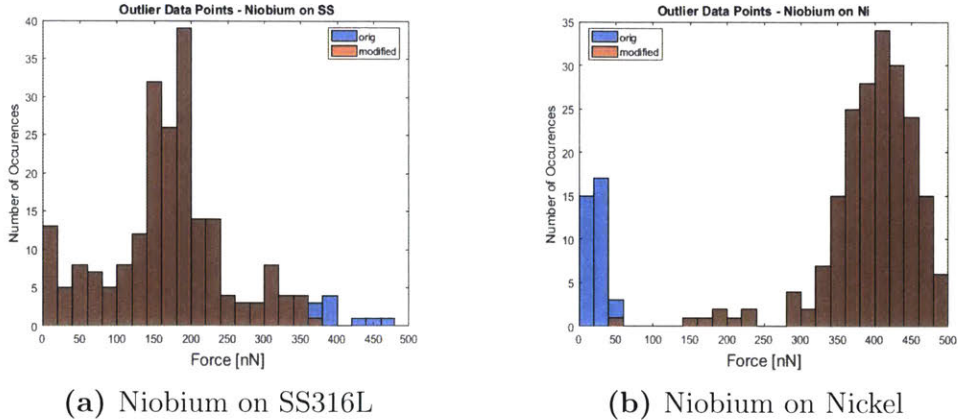


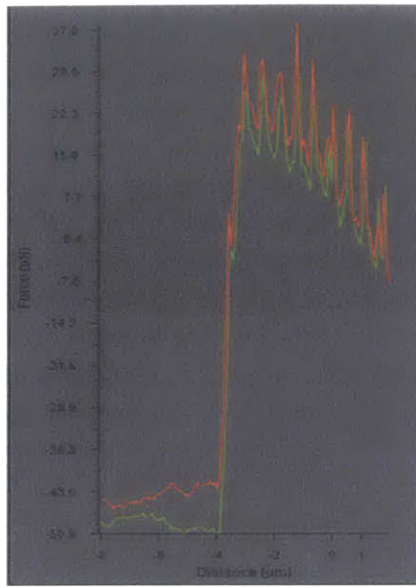
**Figure 6.7:** Two more examples of the removal of outlier data. In the niobium on SS316L case, the high data was removed. In the case of niobium on nickel, the low data was removed. Blue is original; orange is modified; brown is the intersection of original and modified; and the remaining blue region shows the outliers.

during this final phase would likely be more apparent. However, the cantilevers were prepared too early. With the resultant delays in the chamber construction, the cantilevers were left untested in a desiccant container for over 5 months. The shiny chip surface had become dull in appearance as oxidation had occurred. More cantilevers were placed on order and upon receipt were to be given a 50 nm coat. In the meantime, the old cantilevers were placed into the ezAFM and chamber and measurements were attempted nonetheless. All four cantilevers failed to tune. At the time, their failure was attributed to the aging of the coating. However, this reason is not likely. When the new cantilevers were sputter coated, they were immediately placed into the AFM for measurement. All three cantilevers failed to remain in tune or be stable enough to make force measurements. A graph of the force curve for one of the cantilevers is shown in figure 6.8. One possible explanation is post-sputtering shrinkage of the thin film from the inherent stress (normally tensile) following sputtering [44]. If an uneven shrinkage (twist or bend) were applied to the bottom of the cantilever, from either the sputtering stress or thermal expansion differences, the reflected light might be sufficiently affected to put an already weak signal below the minimum threshold required to tune. A third batch was sputtered coated with a layer of 30 nm to reduce any negative effect of sputter thickness. The third set of cantilevers worked sufficiently well to give a full set of stable readings.

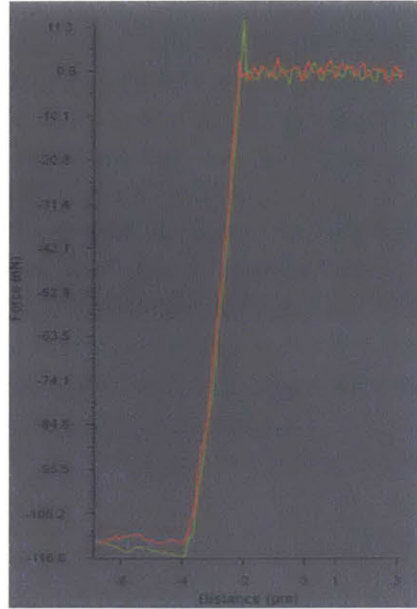
The molybdenum cantilever force values were lower across the six substrates than the other noble metal cantilevers. Moreover, where molybdenum was the strongest during the preliminary phase, it was the weakest in this second phase. The tips in both the preliminary phase and this last phase were taken with a 30 nm coat on silica spheres. Three possible explanations are presented.

1. During the preliminary phase the substrates were allowed to oxidize in normal laboratory conditions. Moreover, a week had passed since the sputtering of





(a) Instability in a probe.



(b) Typical force curve.

**Figure 6.8:** On the left, a screen shot from the ezAFM software program of the instability of the cantilever. Although the graph is inverted from the typical way a force curve is drawn, the instability of the approach to (right to left) and retract (left to right) from the surface. On the right is the curve from the same cantilever three runs prior. The (small) adhesion can be seen as the upward spike on the retraction curve.

the molybdenum cantilever tips to the time they were measured in the AFM. The AFM measurements were taken in normal laboratory air with no special temperature or humidity controls. The implications are: (1) bare molybdenum has poor adhesion with bare metals at room temperature and (2) molybdenum oxide ( $\text{MoO}_3$ ) has strong adhesion on thin layers of metallic oxides. This study tends to confirm the former but other studies would need to be conducted to determine the latter.

2. Both sets of molybdenum data were each collected on a single day. The possibility that there was a systematic error in the preliminary phase seems quite plausible in hindsight. At the time of the measurement, the operator was reasonably experienced in data collection. Two separate cantilevers were used for data collection, so it is not likely to be the effect of a single cantilever.
3. The same setup question could be applied to the final phase where the data was collected in a single day with a single cantilever. The situation is plausible but considered unlikely. The operator had numerous hours in working with the previous 50 nm molybdenum cantilevers for several days. Although mostly unreliable, on a few occasions a single force curve would appear such as seen in figure 6.8b. These occasional curves also showed low values.

**Molybdenum as substrate** An additional factor to take into consideration is how molybdenum as a substrate performed. It is the only element that was both a substrate and tip. The clean bare molybdenum in the final phase showed poor adhesion with niobium and molybdenum. Antimony and tellurium both had moderate adherence. For the non-bare molybdenum substrate of the preliminary phase, only the molybdenum tip showed a strong adherence. This information would point to the low values of the second phase having validity. In evaluating this apparent conflict, it seems that the best information from this work is that bare molybdenum at room temperature in a dry oxygen-free environment exhibits low adhesion with other bare metal structural materials and with silicon carbide. Further investigation into the adhesion forces of molybdenum oxide would be needed to confirm or dispute the results of the preliminary phase.

### 6.2.2.2 Coating Thicknesses

One of the most consistent elements of this study was that of geometry: a nominal 4  $\mu\text{m}$  diameter silica ( $\text{SiO}_2$ ) sphere placed at the tip of an AFM cantilever. One of the least consistent elements was the level of thickness applied to the sphere. Thickness of the coat was a starting concern because it had to be thick enough to overcome any possible bulk force of the silica. Intuitively, 10-30 nm made sense based on Langbein's conclusion where the force of the layer becomes the major factor as the separation distance approaches the thickness of the layer as illustrated in figure 2.3 [39]. At contact, the 10-30 nm coat should be adequate. A second concern was the impact of too large a layer on the sphere and cantilever. Excessive coating could interfere with the geometry or the properties of the cantilever. The third concern was the longevity of the tip. Wearing the noble metal off of the sphere was a risk if the coating was too thin or had poor adherence. Observations and conclusions are presented.

1. Because of the incomplete control of the evaporator process, the first set of tellurium cantilevers had 650-750 nm coats. These cantilevers were used in the preliminary phase. The first set (and only set) of antimony cantilevers had 456-469 nm coats. Better process control was invoked later and the second tellurium cantilevers had 28-32 nm coats. The antimony and second set of tellurium cantilevers were used in the final phase. Because two widely variant thicknesses were observed with tellurium, it appeared that the 20 times difference in coating thickness had little impact on the results. The preliminary results with the heavy coats were comparable to the final results with the normal coat size. Moreover, the antimony cantilevers with the heavy coats appeared to function similarly to the lightly coated tellurium cantilevers on all substrates.
2. The durability of tips appeared to have little impact regardless of the coating depth. There were only a few occasions where a change or degradation of adherence at the time of measurement was thought at first due to a loss or wear of the tip. In two cases, the actual loss of the entire sphere/particle was the mode of failure. In some of the cases, a switch in substrate showed the tip still functioning. There was at least one case where a tip was suspected to have been

worn but confirmation investigation could not be conducted due to breakage of the cantilever upon replacement.

3. A surprising effect of coating was not the actual function of the cantilever but rather a function of the AFM to tune the cantilever. In the case of molybdenum and what is suspected of ruthenium, the thicker 50 nm and 100 nm coats would not tune/align in the ezAFM. The thickness by itself was not an issue as demonstrated by the tellurium and antimony experience, but rather the combination of thickness and material.

### 6.2.2.3 Hastelloy-N

Hastelloy-N was evaluated in this work because it was known to have been fouled by all the noble metals in the MSRE [2], [29]. In evaluation of adhesion of five of the noble metals on other structural metals in comparison with Hastelloy-N, it appears the steel alloys and Ni-201 are at least as strongly adherent if not greater than Hastelloy-N. Molybdenum appeared to be similar to Hastelloy-N in adhesion strength.

In this final phase of the study, antimony, and to a lesser extent tellurium, were found more strongly adherent to Hastelloy-N than the cantilevers with niobium or molybdenum tips. This result is encouraging because it is consistent with the fouling results of the MSRE [8]. More data needs to be collected, but if a trend or correlation can be established, then continuing use of this study's experimental concept and design would be validated.

### 6.2.2.4 Silicon Carbide

SiC was the only non-metal examined in this study. Some of the specific observations, which are shown in figures 6.5 and 6.11 through 6.17 are worth noting.

1. SiC demonstrated the weakest adherence to antimony, which was generally the strongest adhering noble metal.
2. SiC provided the most consistent range of data (smallest standard deviations). The maximum ranges of a tellurium coated tip were the lowest on SiC compared with the other substrates. Specific correlations regarding laboratory AFM-FS data and fouling in the MSR are not established in this work; but if the maximum range of adherence strength data is a more appropriate measure of fouling, then SiC would also be the least fouled with tellurium.
3. Tellurium isotopes are the daughter products of radioactive antimony. Since both are noble in the salt, considering their net effect together from the data collected provides an additional insight. SiC had lower adherence to this pair of noble metals, than did all the other substrates. Figure 6.17 at the end of this section illustrates this observation.

**Table 6.2:** Mean and standard deviation for AFM measurements in the chamber. Tabulated values are in nano-newtons [nN]

[nN]	Niobium		Molybdenum		Antimony		Tellurium	
	mean	stdev	mean	stdev	mean	stdev	mean	stdev
Hastelloy-N	37.4	37.6	31.1	11.6	414.4	59.2	194.0	180.6
SS 316L	166.9	80.5	42.1	8.6	149.8	57.8	372.2	183.6
SS F91	197.4	69.1	45.9	5.4	284.2	74.5	228.1	77.7
Ni-201	397.2	62.6	27.5	9.6	289.8	17.8	224.1	90.9
Mo	17.1	16.9	31.7	11.0	322.3	69.4	161.6	82.6
SiC	122.0	32.5	24.8	5.1	72.6	42.2	193.3	30.9

1. Columns identify the noble metal tips.
2. The rows identify the substrates: Hastelloy-N, SS316L, F91, Ni-201, molybdenum metal and SiC.

### 6.3 Individual Plots by noble metal tip type

The section contains plots by tip type broken out in similar fashion to the summary plots above. The mean is plotted with a 2x standard deviation error bar. Individual force data is overlaid on the plots. A plot is generated for each of the two phases: the preliminary/exploratory phase and the final/chamber phase.

General notes regarding the plots:

1. In the exploratory phase, there were multiple data runs with the same noble metals and substrate combinations. These were combined in a single line in the summary plot. In the individual plots, some separation is presented.
2. In some cases for the exploratory phase, the data seems sparse on the error

bar. This is particularly true for niobium. These were the "all-or-none" runs where there was either no measured adhesion or maximum measured adhesion in any given set of samples. The resultant plot has a mean and a large standard deviation. For these plots, no data was considered an outlier.

## Ruthenium

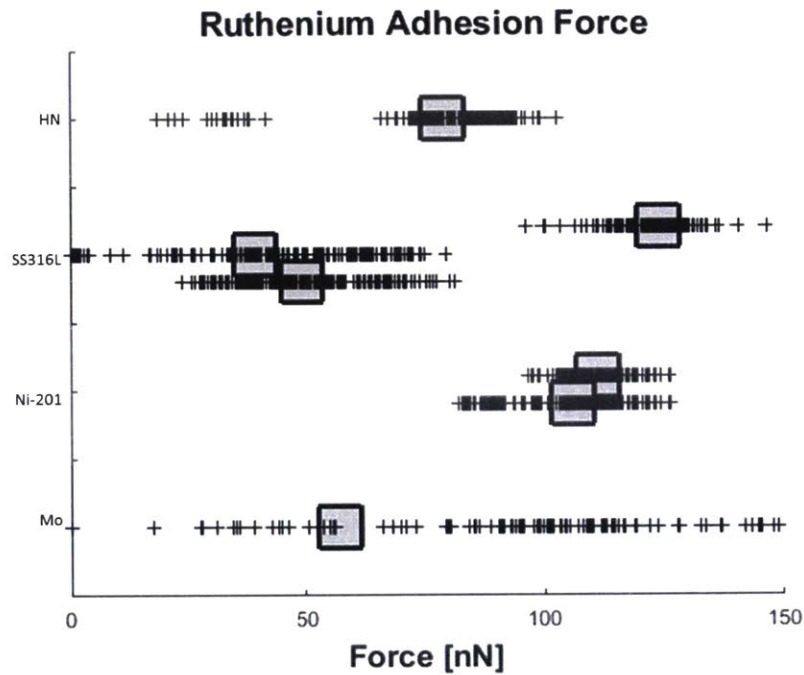


**Figure 6.9:** Exploratory runs. Ruthenium tips on four substrates: Hastelloy-N, SS316L, Ni-201, and molybdenum

# Niobium

The scattered results of niobium during the preliminary phase on SS316L and molybdenum ("all-or-none"), the skewed results on Hastelloy-N, and the concentrated data on nickel was more likely an artifact caused by an understrength cantilever as discussed in section 6.1 above. All of the niobium cantilevers during this stage were of 0.6 N/m spring constant.

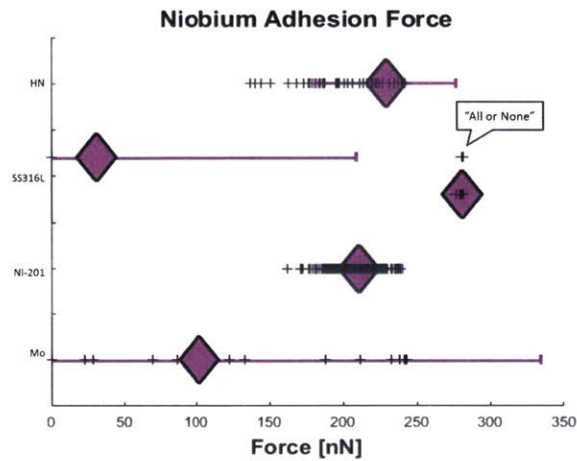


**Figure 6.10:** Exploratory runs. Niobium tips on substrates: Hastelloy-N, SS316L, Ni-201, molybdenum

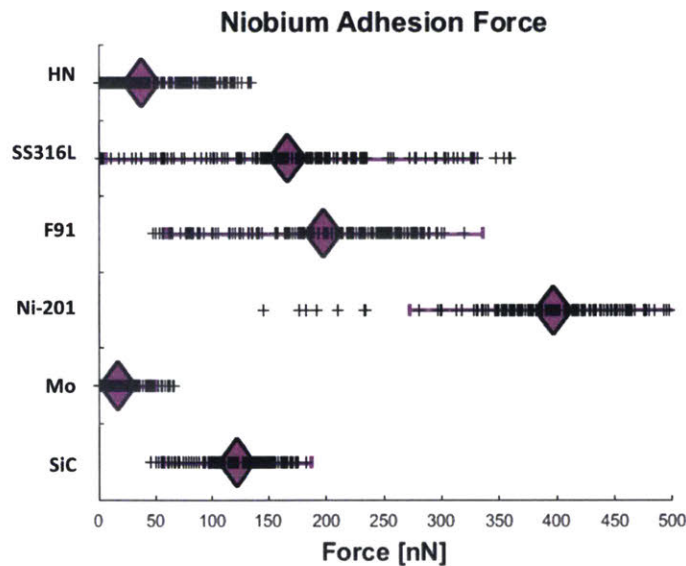


**Figure 6.11:** Chamber runs. Niobium tips on six substrates: Hastelloy-N, SS316L, F91, Ni-201, molybdenum and SiC

# Molybdenum

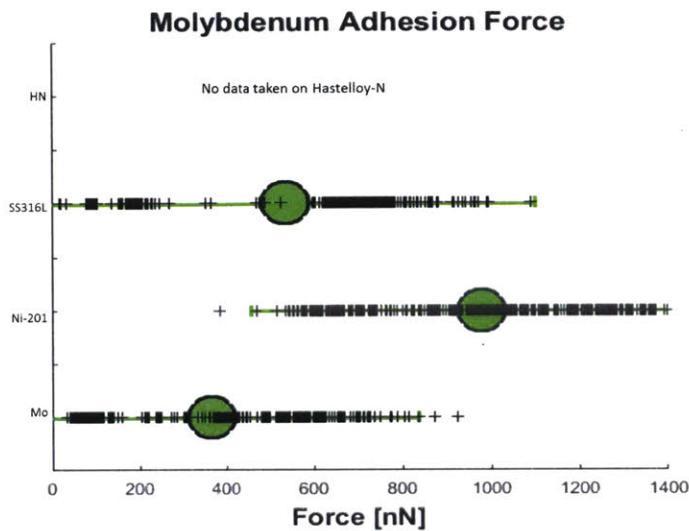


**Figure 6.12:** Exploratory runs. Molybdenum tips on three substrates: SS316L, Ni-201, and molybdenum

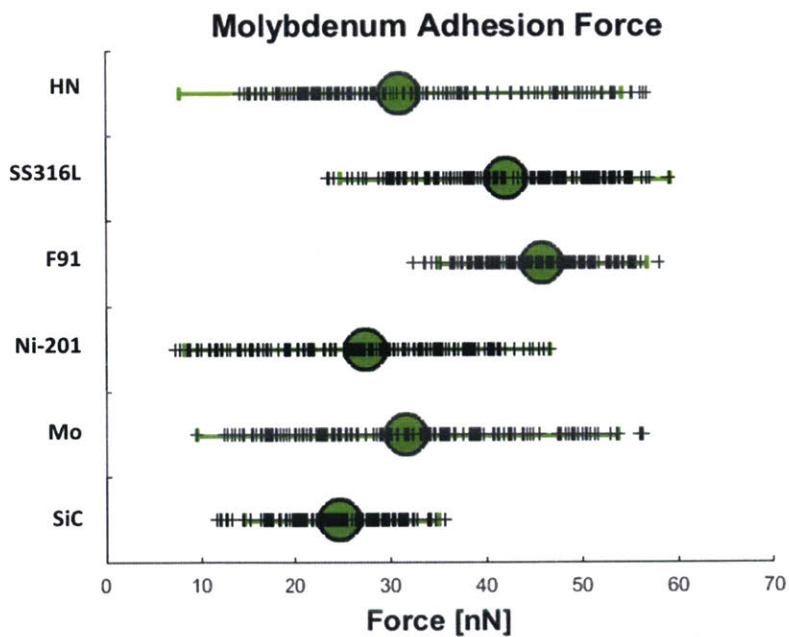


**Figure 6.13:** Chamber runs. Molybdenum tips on six substrates: Hastelloy-N, SS316L, F91, Ni-201, molybdenum and SiC

# Tellurium

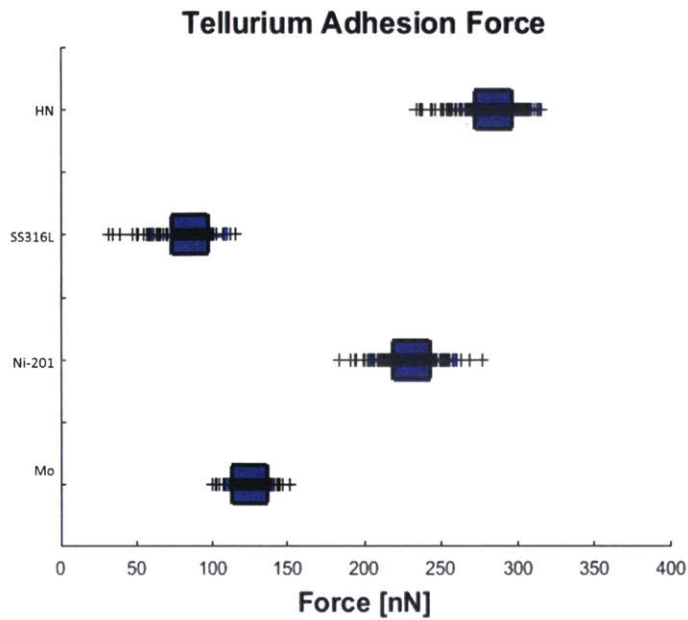


**Figure 6.14:** Exploratory runs. Tellurium tips on four substrates: Hastelloy-N, SS316L, Ni-201 and molybdenum

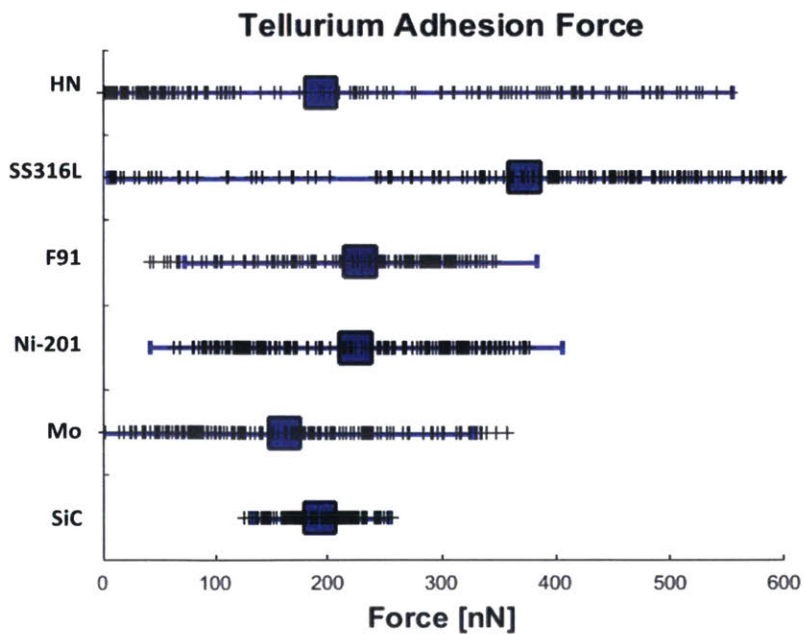


**Figure 6.15:** Chamber runs. Tellurium tips on six substrates: Hastelloy-N, SS316L, F91, Ni-201, molybdenum and SiC



# Antimony

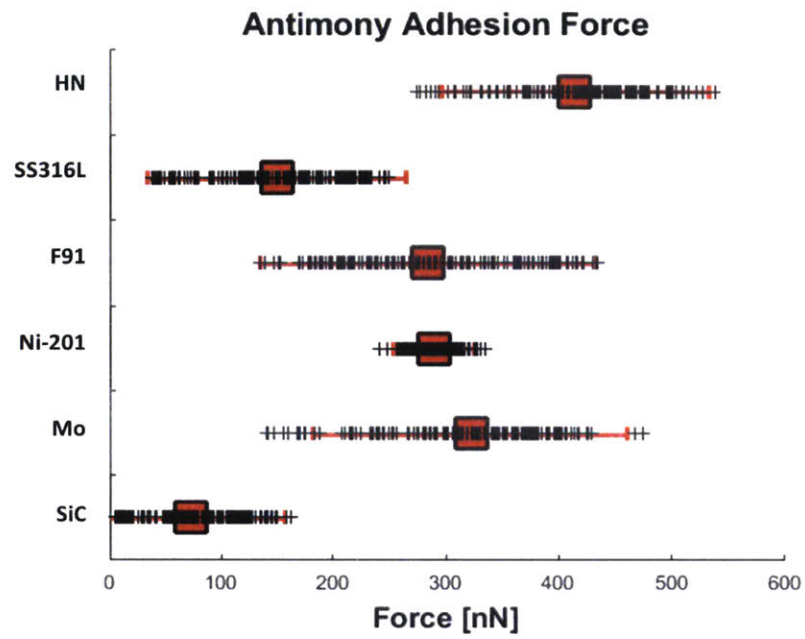


**Figure 6.16:** Chamber runs. Antimony tips on six substrates: Hastelloy-N, SS316L, F91, Ni-201, molybdenum and SiC

# Antimony and Tellurium Combined

Tellurium isotopes are the daughter products of radioactive antimony. Since both are noble in the salt, their net effect together from the data provides an additional insight. SiC had lower adherence to this pair of noble metals, than did all the other substrates.

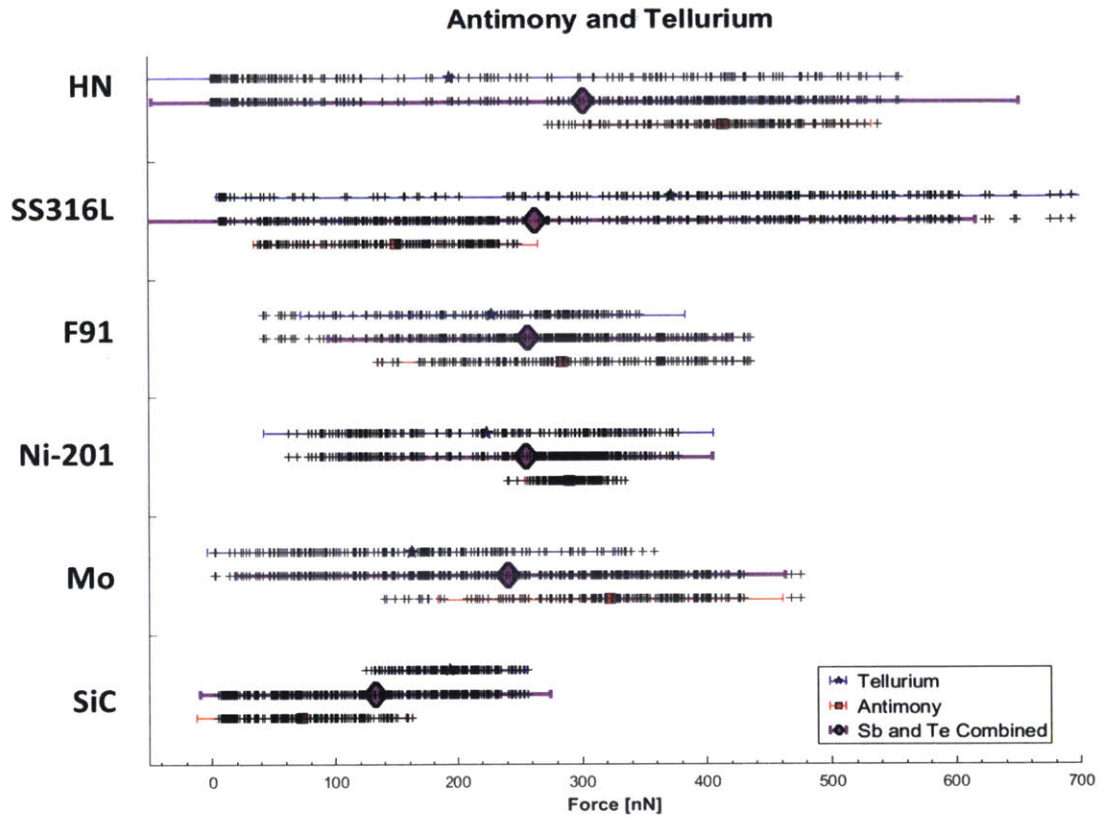


Figure 6.17: Chamber runs. Combined view of antimony and tellurium on six substrates: Hastelloy-N, SS316L, F91, Ni-201, molybdenum and SiC

# Part 7

## Final Thoughts

This study had its origins in the work by colleagues studying the adhesion of corrosion products and mineral oxides in an aqueous environment. The concept is simple: using an AFM, measure the force between a foulant and a surface to help better understand propensity for fouling. For an LWR, this involved aqueous corrosion products on metals with some amount of passive oxidation on the surface. For an MSR, this involved noble metal fission products on bare metal surfaces lacking a passivating corrosion layer. Experimentally, the differences are vast and finding a means of taking those measurements consumed most of the effort of this work. Moreover, in the realm of theory, the differences were also significant. Much of the learning process came from two major course corrections as a result of these disparities.

1. Noble metals versus corrosion products. For the purposes of experimentation, obtaining the specific noble metals in a size and shape conducive for mounting on an AFM cantilever was far more difficult than finding the iron, nickel and chromium oxides used in the LWR study. The challenge was intriguing and it took nearly a year to establish a process for functionalizing the tips. If this study were to be continued, two suggestions are offered:
  - (a) Focus on one or two types of metals to place on the cantilever tips. Having the silica spheres and the cantilevers prepared by the same manufacturers provided consistency. However, having a number of different materials to examine stretched resources and subjected the study to a greater number of variables. Repeating measurements of the same noble metal, prepared similarly on the same machine, with optimized settings for that functionalized cantilever would serve to reduce some of these variables and improve the statistical analysis.
  - (b) The optical properties of metals are quite different than those of the covalently bonded oxides and the determination of van der Waals forces are much harder to theoretically derive. The databases on the refractive and absorption indices or emissivities of metals are sparse in contrast to the large collection of information on oxides. A simplified model for the calculations of the Hamaker constant and the resultant prediction of the van

der Waals force for metals could not be found. The full spectrum analyses, such as those conducted by many others [45]–[47], were beyond the scope of this work. Even so, the spectrum data for the noble metals of interest were non-existent or too sparse to perform such calculations. Focusing on one noble metal may make this problem tractable.

2. Corrosion layers on substrate materials. The bulk properties of materials are the defining factors affecting the forces between particles until the last few nanometers of separation where the properties of the thin surface layers take effect. On contact, the interface between the thin layers could theoretically substantially affect the adhesion force [32], [39]. It was the premise of this study to take advantage of the sputtered thin layer's dominance at contact to measure the force adhesion of the sphere and attribute that force to the material sputtered on the surface. This would be particularly true if the bulk force of silica showed little (or similar) van der Waals properties as the noble metal surface. Under this presumption, an oxide layer on the surface of the substrate, if allowed to grow to tens of nanometers, could also impart a similar affect. This idea led to the construction of the chamber to measure the force on a bare metal surface.

## 7.1 Future Investigations

The goal of this work was to establish a base line for force adhesion at room temperature of noble metal foulants on potential structural or filtering material. Some of the goals were accomplished, but there is much greater work to be done or other avenues to explore.

1. Comparison of adhesion between bare metal and an oxide layer. This study had little data between the two conditions upon which a determination could be made regarding the effect of a corrosion layer on these adhesion forces. An experiment could be better set up by using the same tip on a pre-sputter cleaned and a post-sputter cleaned surface of the same substrate. Measurements could also be done with different oxide thicknesses.
2. Filter materials. This study looked first at structural metals as substrates, but perhaps a more important set of materials to examine would be those that could be used to filter or collect the noble metals. One ceramic material was examined; silicon carbide was found to have fairly low adhesion values. However, other ceramic materials or stable oxides in a molten salt at high temperature that are sufficiently corrosion resistant, may demonstrate the good adhesion properties desired in a collection system.
3. Trigger force and dwell time. The relationship of trigger force and dwell time on adhesion was left unexamined. Although the specific capability of the ezAFM is not built into the software, manipulation of the operator selectable offset and setpoint% values could be used over a single point repeated multiple times to

obtain the data. At the time of this study, this particular type of manipulation was not recognized by the researcher.

4. Coating consistency. Although this study loosely demonstrated various coating thicknesses were not significant factors in adhesion, an insufficient amount of data was collected to bring a firmer conclusion. Using a single type of metal, different thicknesses could be explored and compared.
5. Ionic fluids. The adhesion in an MSR occurs in a fluid medium. The experiment of this study was conducted in nitrogen. Some consideration was made to use an ionic fluid that could be a surrogate at room temperature to that of a molten salt at high temperature. A modicum of effort was applied in finding such a liquid for this study. However, it was realized there are a significant number of ionic fluids in existence and finding one of the correct properties and learning of the potential drawbacks or unintended affects were beyond the scope of this study. A future study could focus on finding such a surrogate, if one exists.
6. A model to assess the experimentally derived results is needed. The nature of the van der Waals forces for metals is based in quantum electrodynamics. Exploring existing Density Functional Theory models to align with the experimental component would be useful for evaluating results.

## 7.2 Future Use of the Chamber

The coupling of an argon ion gun and an AFM worked well to measure dry polished, oxide free metal surfaces in an inert atmosphere. The combination vacuum chamber / glove box also provides a unique capability.

1. The chamber was built for the study of specific noble metal adhesion on bare metal surfaces. However, other adhesion studies on an AFM requiring a clean surface in an inert dry atmosphere could be done. If further use of the AFM in the chamber is desired, one major consideration (if at reasonable cost) would be to obtain an ezAFM head calibrated for air or nitrogen. Useful data may have been obtained from those cantilevers that failed to tune or align in the Aqua ezAFM.
2. The argon ion gun polisher alone would serve other sample preparation needs in the laboratory for other research. Contamination of the surface by laboratory air following mechanical polishing could have those contaminants removed with the argon ion gun and transferred to a small portable inerted vessel positioned in the main chamber.

## 7.3 Positive Impacts of Noble Metal Fouling?

This journey started on the premise that fouling is an undesirable intrusion in our finely engineered thermodynamic reactor machines. From the view of the LWR,

fouling only brings about negative outcomes and are challenges to solve. In an MSR, the negative outcomes such as high radiation and heat on equipment are large and pose substantial challenges to the MSR designer. However, unlike the LWR there are some positive aspects that may be opportunities or positive unintended consequences to consider.

1. **Surface Protection** Noble metals deposited on surfaces may very well provide passive protection against further corrosive attack by the very nature of the metals being noble. Grimes from ORNL suggested passive protection as one possible explanation for lower than expected corrosion rates on some of the MSRE runs [48]. The attack on chromium is diffusion limited by the rate the chromium can diffuse to the surface from where it is oxidized. A noble metal layer would serve to reduce such diffusion and it could be envisioned that at some point in the vessel's history, the entire surface might be passively protected. More importantly may be the ability for a noble metal layer to resist attacks from an impurity such as water, which finds itself in the salt. For an operational reactor versus an experimental one with tight chemistry controls, the tolerance for impurities and corrosion from those impurities are a significant aspect not yet fully explored.
2. **Freeze Protection** Salt solidifying (freezing) at 400 °C to 600 °C poses an entirely different paradigm to a reactor designer. Freezing at the wrong points during operations (or while combating an accident) could very well become a limiting factor. Freezing of the (colder) heat exchanger for example is a form of a loss of cooling. Having substantial decay heat on the surfaces of the heat exchanger might actually be a benefit, which can support unusual circumstances.
3. **Fission Product Extraction** The noble metal  $^{99}\text{Mo}$  isotope has value for medical use and selective extraction of this isotope would be desirable. Because many short and medium lived fission products are retained in a spent fuel rod, the industrial or scientific utility for such products may not have been explored for the basic reason the products are currently largely unavailable. Selective extraction of these materials may provide the wider availability needed to spark innovation.

## 7.4 Final Words

Great credit for the incredible invention of the MSR and the commensurate brilliant research must be given to the men and women of the Oak Ridge National Laboratory. Resurrecting their work and sustaining it in the form of a commercially viable MSR would be a great tribute. It is the hope that this study made some small contribution to that effort.

# Appendix A

## Molten Salt Reactor

This century, renewed interest in the Molten Salt Reactor (MSR) idea has witnessed the growth of reactor start-up companies in the US, Canada, the Czech Republic and Japan, new governmental efforts in China, Russia and in the European Union, and adoption as one of the six advanced technologies announced by the Generation IV International Forum (GIF) in December 2002. Moreover, new MSR related research has blossomed all over the globe [49]. Much of what is discussed in open literature today of these new efforts, takes their start by reaching back to the remarkably comprehensive research already conducted in the MSR Experiment (MSRE) at the Oak Ridge National Laboratory (ORNL) in the latter half of the last century <sup>1</sup>. The salts and structural materials under evaluation by today's worldwide effort largely stem from those which were evaluated by the MSRE project team; and similarly, it is the basis for the materials selected in our fouling study.

### A.1 The Molten Salt Reactor Experiment

As inferred, a discussion on MSRs would be substantially lacking if it does not acknowledge the tremendous body of research and work produced by ORNL<sup>2</sup>. From the late 1950s to the early 1970s, ORNL sequentially ran two similar but different MSR programs. The first was the Aircraft Reactor Experiment (ARE), which ran from 1949 to 1961 with the intent of powering a US Air Force bomber. The ARE culminated in a 2.5 MW<sub>th</sub> reactor, which went critical and operated at various power levels for 9 days in 1954. In 1959, based on the demonstration shown during the ARE, the MSRE project was born. The goal was for commercial power and breeding of fuel versus for powering flight. For the next 25 years, the ORNL team and the MSRE provided much of what we know about MSRs today. The crowning achievement was a small 8 megawatt (thermal) MSR, which operated at power for over 22,000 hours

---

<sup>1</sup>Russia's current MSR program dates back to a secretive time in the 1970s, but political interest waned following the reactor accident at Chernobyl in 1986 and the collapse of the Soviet Union [50].

<sup>2</sup>This summary of the ARE and MSRE is of historical record. Much of this distillation of history is embodied in the memoir-like piece titled "The Molten Salt Reactor Adventure" by H.G. MacPherson the first program manager of the MSR effort [51] and in a ORNL history report titled "An Account of Oak Ridge National Laboratory's Thirteen Nuclear Reactors [52].

in the late 1960s. The reactors were a radical departure from the light water reactors constructed by the US Navy and by the burgeoning international civilian nuclear power industry. The coolant was not water, but a molten salt, and the uranium fuel was not in a solid core matrix, but was dissolved in and circulated with the coolant. While it was not uncommon in the 1950s and 1960s for the US national laboratories to experiment with many types of coolants and fuel configurations, the MSRE stood out as one of the few that could boast successful continuous full power operations.

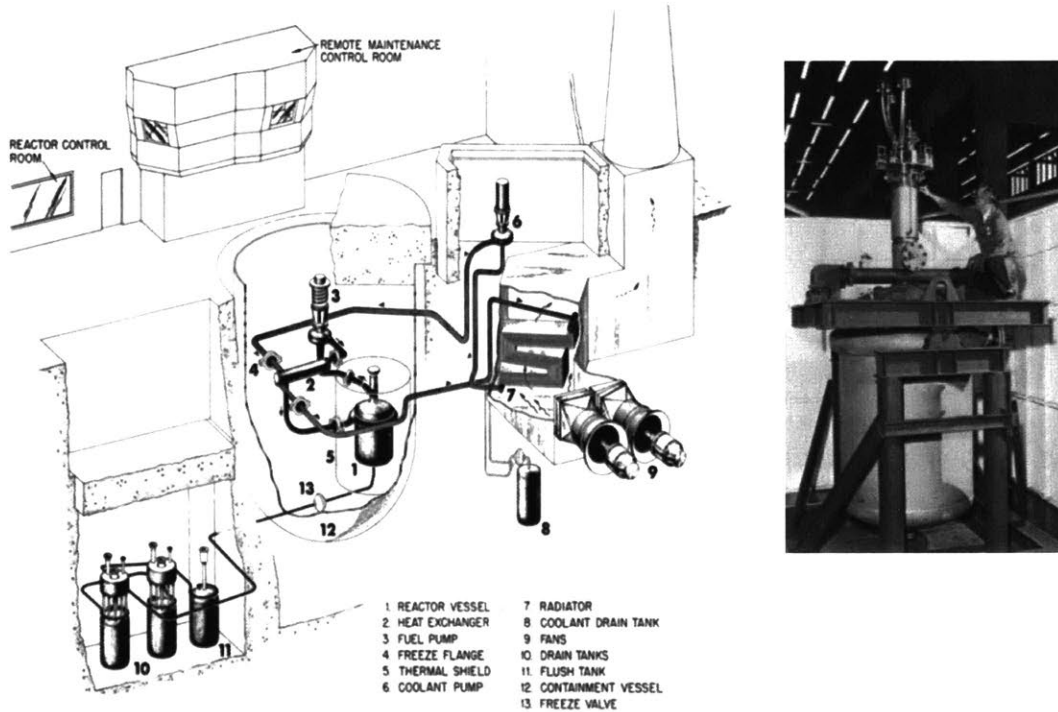


**Figure A.1:** The layout of the Molten Salt Reactor Experiment in this graphic provides a sense of size and compartmentalization needed due to high temperature and radiation. The photograph provides the sense of size. Source: Historic Molten Salt Reactor Experiment Brochure (1965-2015), Oak Ridge National Laboratory, Historic Archives [53]

### A.1.1 Key Aspects of an MSR

The MSRE showcased many of the advantages that a molten liquid fuel salt offers over that of a LWR. For simplicity, this discussion will highlight four aspects of note: operating pressure, operating temperature, fuel mobility and waste disposal.

1. Operating Pressure. From a cost and safety standpoint, an MSR would operate at close to atmospheric pressure, which obviates the need for high pressure systems engineering and directly reduces costs that sturdier or thicker components would demand. Moreover, removing water and steam (under high pressure) also removes the key pathway of radioactive release during an accident. Protective



measures for LWRs require massive and costly containment structures primarily due to the tremendous thermal energy stored in the water/steam system.

2. **Operating Temperature.** The higher operating temperature affords better thermal conversion cycle efficiency, which in turn can improve costs or provide heat needy missions. The high temperature also demands materials and equipment, which can operate in those conditions. Moreover, the higher temperatures, which must be maintained even during shutdown to prevent freezing of the salt, would limit human access for inspections and maintenance.
3. **Fuel Mobility.** The circulating fuel enables greater burn-up, which means a greater utilization/consumption of the fissionable material. Solid fuels are primarily limited because of the buildup of pressure due to fission product gases coinciding with radiation damage to the fuel element structure. The liquid fuel does not retain the gas and is impervious to radiation damage. Thus, the fuel itself can remain in the reactor indefinitely. Moreover, a liquid fuel simplifies refueling and reconfiguration, which can be executed while at power. However, the price of the mobile fuel is mobile highly radioactive fission products and actinides and the need for processing the same. The distributed fission products points directly to the fouling research of this paper.
4. **Waste Disposal.** The advantages/disadvantages of a fluid fuel over that of the current state of solid fuel long term disposition / waste storage is a complex and lengthy topic and far beyond the scope of this appendix. However, one point related to fouling is germane. Fluid fueled reactors present a double-edged sword: (a) the opportunity to selectively extract fission products for use or for a tailored, facilitated disposal pathway; and (b) the challenges of disposing of large reactor components, highly contaminated by fission products and actinides. Knowledge of fouling propensity may inform plans for selective removal mechanisms in the former and decontamination of the latter.

### **A.1.2 Physical Layout**

The layout in figure A.1 of the MSRE paints the picture of the physical challenges of access in an MSR due to high temperature and radiation. The MSRE had two loops much like that of a PWR where molten salt is used instead of water: (1) the fuel salt loop that produced heat through fission in the vessel with a graphite moderator and that delivered its heat through a heat exchanger to (2) a secondary cooling loop of salt that took the heat from the primary loop and discharged the its heat through an air-cooled radiator.

The fuel (primary salt) pump was particularly ingenious. The pump bowl was quite large and served multiple purposes:

- as a surge volume to accommodate the expansion and contraction of the thermal effects of the salt;
- as a volume to allow the collection and disposal of fission product gases; and
- as a well from which to draw salt samples during operation.

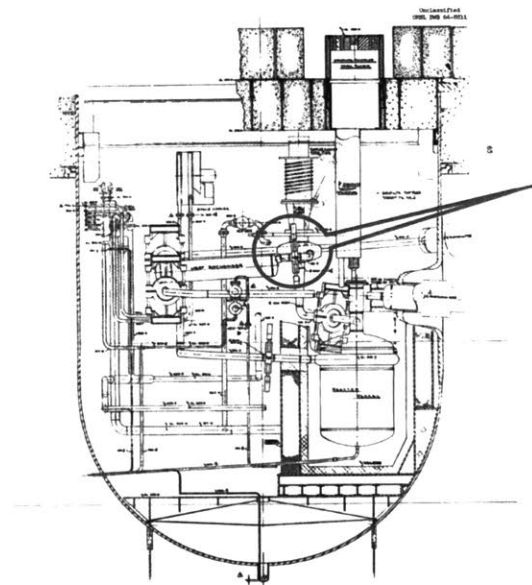


FIG. 5.2. REACTOR CELL ELEVATION.

(a) MSRE elevation view

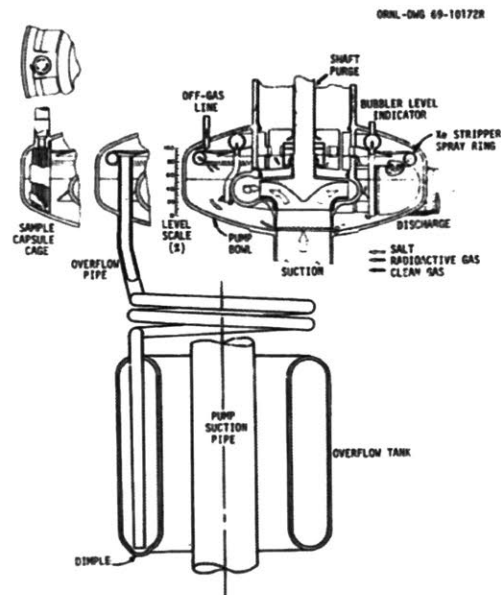


FIGURE 2.5. MSRE FUEL PUMP AND OVERFLOW TANK

(b) MSRE pump

**Figure A.2:** MSRE cutaway view of the reactor cell and pump. In addition to just recirculating (pumping) the salt, the fuel pump served many functions. The pump was the main gateway for sampling and maintaining fuel salt chemistry. It also served as the surge volume for the salt and the high point for the gas sampling system. Source of the (a) cell cutaway is ORNL-TM-0728 [21] and the (b) pump cutaway is ORNL-TM-3884[4].

Below the reactor vessel, the MSRE was equipped with a set of tanks and unique piping system that served as an inventive means for shutdown and emergency conditions. Since the fuel is liquid, the reactor design can take advantage of the fuel's mobility. The fuel could be drained to these tanks if a situation warranted for such things as maintenance or for remote decay heat removal during an emergency far away from the large graphite moderator in the core.

Besides designing and creating an entirely different kind of reactor, finding materials that could sustain high temperature operations in a molten salt environment

was a huge undertaking for the MSRE team. One of the fruits of their labor resulted in a nickel-based alloy then called INOR-8 and currently named Hastelloy-N [54].

The MSRE was constructed largely of just two materials that faced the salt. Hastelloy-N made up nearly all the metal components: the primary heat-exchanger, the vessel and piping. Graphite was the second material and was the central moderator. Hastelloy-N made up approximately one-fourth of the surface area in the reactor while graphite made up the remaining three-fourths of the surface area and was used as the neutron moderator in the central core area of the vessel.<sup>3</sup>

### A.1.3 Gas Management

One additional aspect key to our discussion on fouling is need for a gas management system and a small positive overpressure system with an inert gas such as helium. The gas management system serves several two key tasks. First, the insolubility of fission product gases and low vapor pressures of some of the salt elements such as  $ZrF_4$  requires a system to remove and contain these gases. Second, a surge volume is required such that small temperature changes would not cause destructively high or negative pressure fluctuations in a system with an incompressible fluid such as molten salt. The MSRE used helium to bubble through the salt and maintain a cover gas at five psig (0.33 atm) overpressure. Fission products gases, along with the helium, migrate to high points in the system. The MSRE's pump was located at the high point in the system and served also as the gas trap [21].

Not only did the gas management system transport fission product gases of xenon and krypton out of the salt, noble metals were also swept out on the surfaces of the gas bubbles. While much of the metal did not migrate much past the liquid/gas interface, the metals were located in locations such as the pump bowl where a gas/liquid interface existed.

## A.2 Molten Salt

Although there are as many molten salts as there are salts, the salts being considered for MSRs are relatively few. In the MSRE, the main fuel salt was winnowed down from that universe of many salts by evaluating dozens of properties and aspects. Mechanical features such as temperature of melting and boiling, viscosity, and vapor pressure narrowed the field. Chemical stability in a radioactive environment, and the solubility of uranium and/or plutonium, narrowed the choices further still. Neutron

---

<sup>3</sup>Regarding fouling, surface area was important. Surface areas were calculated to be: 225 m<sup>2</sup> graphite moderator and 79 m<sup>2</sup> on Hastelloy-N, of which the heat exchanger consisted of 32 m<sup>2</sup> and the reactor vessel and piping consisted of 47 m<sup>2</sup>. [2]. Of note, in planning for the future MS breeder reactor (MSBR), ORNL estimated the heat exchanger would have the largest exposed surface area and would be of the largest concern for decay heat and fouling in that reactor. For the 1GWe MSBR design, the surface areas were: 3716 m<sup>2</sup> on the heat exchanger, 3066 m<sup>2</sup> on the graphite moderator and 325 m<sup>2</sup> for vessel and piping [29].

cross-sections for absorption and scattering are of particular significance in a reactor further necking the field down.

### A.2.1 Melting Point – Illustrative of Selection Criteria

Melting point is just one of many important properties of a reactor fuel salt, but it serves as a useful example of how selection of candidate salts are evaluated. Considering  $\text{UF}_4$  melts at  $1035^\circ\text{C}$  and vessel alloys that can sustain long-term reactor operations in a molten salt environment at temperatures greater than  $800^\circ\text{C}$  are yet to be discovered, depression of the melting temperature of a salt with  $\text{UF}_4$  is essential. Figure A.3 is the phase diagram for the mixture lithium fluoride and beryllium fluoride salts. Lithium fluoride alone melts at  $458^\circ\text{C}$  and beryllium fluoride alone melts at  $555^\circ\text{C}$ . Put into the right molar ratios the combined salt (known as FLiBe) can have a melting point at  $360^\circ\text{C}$ .

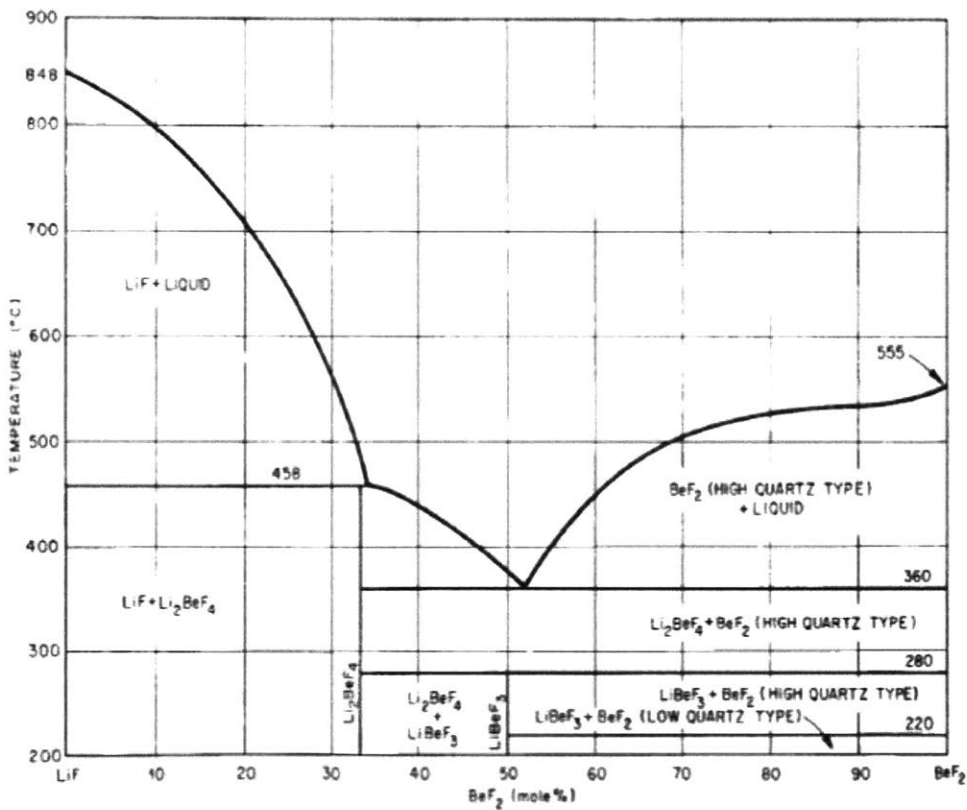


**Figure A.3:** The phase diagram for LiF and BeF<sub>2</sub>. LiF melts at  $458^\circ\text{C}$  and BeF<sub>2</sub> melts at  $555^\circ\text{C}$ . At a molar ratio of 48:52 (LiF:BeF<sub>2</sub>) a eutectic melting point of  $360^\circ\text{C}$  is achieved. Source: W.R. Grimes “Molten-Reactor Chemistry” (1970) [5]

A similar diagram for lithium fluoride and uranium fluoride would result in a eu-

tectic at 490 °C with  $\text{UF}_4$  at 27 mole% [5]. For more than two salts, a ternary phase or melting point diagram is useful. Figure A.4 was constructed when adding  $\text{UF}_4$  to FLiBe [55] [48]. From the diagram, a range of desired melting points can be achieved with the right mixture of salts.

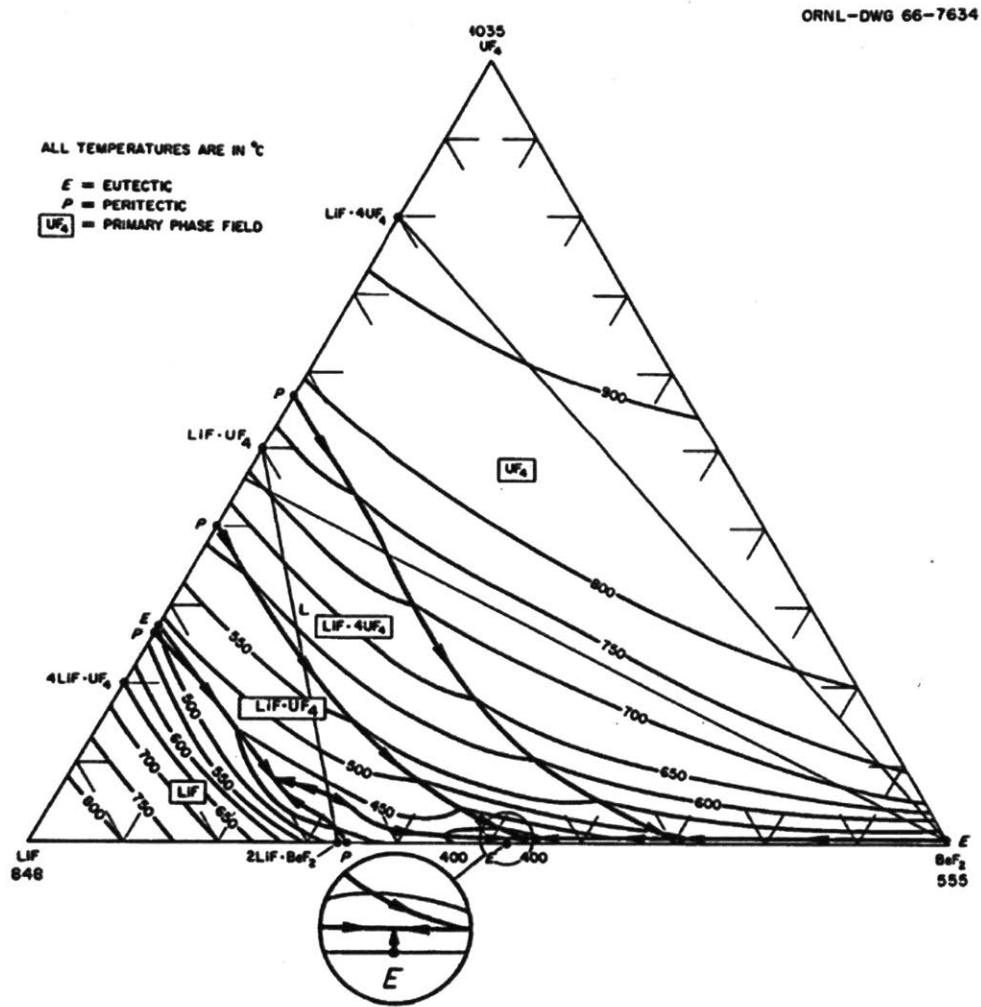


**Figure A.4:** Adding a third element to the diagram, in this case,  $\text{UF}_4$ , a melting point diagram can be constructed. The circled area is the  $\text{LiF}\text{-BeF}_2$  eutectic at 360 °C. Source: J.A. Lane, editor, Part II, chapter 12 “Chemical Aspects of Molten-Fluoride-Salt Reactor Fuels; Fluid Fuel Reactors (1958) pg 577 [55]

## A.2.2 Typical Salt Elements

The MSRE was known colloquially as a “chemist’s reactor” because the chemistry took far more effort in day-to-day operations than the actual operations of the reactor. The ORNL team eliminated many salts in their search. Although not pre-

sumed to be a complete accounting, current MSR designers have primarily reached similar conclusions using similar elemental ingredients. As a molten fuel salt, the halide salts—where the anions are fluoride ( $F^-$ ) and to a far lesser extent, chloride ( $Cl^-$ )—are the focus. Fluorine has a low neutron cross-section for absorption and exists primarily in a single stable isotope and a single valence state of -1. Chlorine is more complex with higher neutron absorption rates, a more active set of isotopes and many valence states. For the cation, many metals are considered for MSRs. (Some acronyms for fluoride salts have been popularized and follow the easiest spelling using elemental symbols).

FLiNaK. The fluoride (F) salt of sodium (Na), potassium (K)

FLiBe. The fluoride salt of lithium (Li) and beryllium (Be)

UF<sub>4</sub>/UF<sub>3</sub>. The fluoride salt of uranium (U) in both its IV+ and III+ valence states.

LiCl-NaCl-KCl-MgCl<sub>2</sub>. The chloride salts of lithium, sodium, potassium and magnesium.

ZrF<sub>4</sub>. The fluoride salt of zirconium (Zr)

ThF<sub>4</sub>. The fluoride salt of thorium (Th)

#### **A.2.2.1 FLiBe and the MSRE**

FLiBe was the primary base salt in the MSRE and is featured predominantly in some of the more mature designs of today's current efforts.<sup>4</sup> FLiBe demonstrated good stability and solubility with the UF<sub>4</sub>/UF<sub>3</sub> fuel and with ThF<sub>4</sub>, which was expected to be used as the future breeding fertile material in the MSBR. FLiBe also was shown to have desirable thermal and nuclear characteristics and is relatively chemically inert and stable.

---

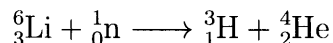
<sup>4</sup>Some designers are also looking at plutonium and chloride salts. Plutonium has very different solubility than uranium in fluoride and chloride salts and offers greater challenges in physical chemistry. Uranium molten fluoride salt is a proven concept. Plutonium chloride reactors are still very much on the drawing board.

Salt Component	Composition		Weight <sup>1</sup> [kg]
	Mole%	Weight%	
LiF	65.0	40.48	2098
BeF <sub>2</sub>	29.1	32.76	1698
ZrF <sub>4</sub>	5.0	20.02	1038
<sup>238</sup> UF <sub>4</sub>	0.61	4.59	238
<sup>235</sup> UF <sub>4</sub>	0.29	2.16	112
Total Weight			5184

1. From ORNL Report 4616 Preparation and Handling Salt Mixtures [56]

**Table A.1:** The Mixture of Fuel Salt in the First MSRE Run

**Lithium** Lithium as a cation is also ideally suited with one major drawback. Lithium (<sup>6</sup>Li) undergoes a neutron interaction and creates tritium and helium



Natural lithium is approximately 92% <sup>7</sup>Li and approximately 8% <sup>6</sup>Li. Enriching lithium to 99.99% <sup>7</sup>Li is expensive and could tack on additional tens of millions of dollars to the cost of a lithium based reactor [57].

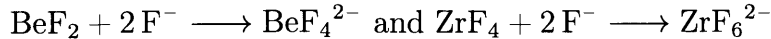
**Beryllium** Beryllium seems to be the ideal additive since it has the best properties to suit both the chemist and the nuclear engineer: melting point suppression, good interaction with fluorides, the ability to move uranium electrochemical potential for corrosion control, and low neutron cross-section.

Beryllium (metal) and to a lesser extent BeF<sub>2</sub> salt, however are quite toxic and therefore, an additional dimension of handling issues is presented.<sup>5</sup> Some reactor designers would prefer to avoid beryllium specifically because of the toxicity.

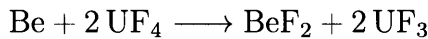
**Zirconium Fluoride** ZrF<sub>4</sub> was added to the FLiBe for the earliest run in the MSRE. As a low neutron absorber, ZrF<sub>4</sub> provided a chemical stability as any oxygen source or water would preferentially create zirconium oxide over that of uranium oxide. Uranium oxides are insoluble. If allowed to precipitate and concentrate, the uranium oxides could create localized fission or criticality where none would be desired.

<sup>5</sup>A good discussion of beryllium fluoride from a nuclear reactor viewpoint is in the Fluoride-Salt-Cooled High Temperature Reactor (FHR) Materials, Fuels and Components White Paper from the FHR Integrated Workshop 3 in 2013. (FHR, 2013)

Moreover,  $\text{BeF}_2$  and  $\text{ZrF}_4$  both form fluoride ionic complexes as Lewis acids that tend to remove "free" fluoride ions and reduce the corrosiveness of the salt [16].



**Uranium** Uranium is added in the U(IV+) valence state as  $\text{UF}_4$ . From the combination of impurity oxidation, corrosion of structural elements and fission  $\text{UF}_4$  is reduced to  $\text{UF}_3$  over time. The ratio of  $\text{UF}_4$  to  $\text{UF}_3$  as a majority constituent sets the electrochemical potential of the salt. Lowering that ratio improves general corrosion, however if too low then the undesirable formation of uranium carbide (UC) would occur and would precipitate the uranium out of the salt. Metallic beryllium was occasionally added to maintain the ratio of these two buffering constituents close to 100:1 [5].



### A.2.3 Molten Salt Properties

Molten salts have a few particular properties that might not at first be obvious but require significant consideration for any molten salt plan. The safety of an MSR takes advantage of the properties of temperature and pressure already discussed. However, molten salts sometimes live in a parallel world from LWRs:

- Freezing. Cold is relative and in an MSR that might be  $<500^\circ\text{C}$ . Designs, plans and vigilance for freezing (and re-melting) are required. Of significance is the consideration for a system to go solid and experience large, destructive pressure changes due to thermal expansion upon melting. Expansion while melting may seem at first abnormal since water expands while freezing. However, water is an oddity of nature in this sense: most materials contract while freezing and expand while melting. Pipe rupture is a well-known catastrophic outcome of a frozen pipe due to water's expansion. The salts involved in an MSR shrink upon freezing and expand upon melting. Thus for an MSR, the greatest risk of bursting the vessel, pipes or other components comes upon melting. Moreover, freezing can occur in the reaches of the plant that are still hot enough to boil water. Blockage of flow or instrument lines by freezing can put the reactor, safety systems or processing system at risk.
- Freezing, part 2. Freezing also makes the MSR self-healing. A leak to the environment would likely cause the salt to freeze that would tend to plug the leak. Similarly, a spill would tend to stop flowing for the same reasons. A spray into the environment would result in freezing and precipitation. Unless the salt and its radioactive elements dissolve into water, an atmospheric spread is halted by the salt solidification (freezing) and the resultant precipitation.
- Hygroscopic. The fluoride molten salts of interest are quite hygroscopic and will absorb moisture if exposed to normal air. Even small amounts of water leads



to the local formation of hydrofluoric acid and many other forms of corrosive attack on plant materials. Moreover, water can react with uranium fluoride to produce an insoluble uranium oxide that will precipitate out of the fluid. Avoiding water/moisture is an important factor.

- Double “Hot”. Because the fuel salt is so radioactive, all operations will need to be done in hot cells with remote operating devices, perhaps robots doing the work. Moreover, because the salt will likely need to be in liquid form, the hot box will be not only radioactively hot, but thermally hot as well. Things that are simple in LWR chemistry for example, might become exceedingly difficult in an MSR processing plant.

### A.3 Molten Salt Sampling in the MSRE

Many of the routine operations in an LWR such as visual inspections, maintenance and sampling, are considerably more difficult in an MSR because of the high temperature and high radiation levels. The ingenuity of the ORNL team to accomplish such tasks was evident throughout the MSRE. A glimpse at the types of surveys, samples and inspections that were conducted in support of fission product determination gives a good example of their inventiveness. Some of those crucial to the knowledge of noble metals are summarized here:

1. Fuel Salt and Flush Salt Direct Sampling. Between runs of the two fuel salts, the MSRE was flushed with a clean salt of similar mixture but without the fuel. The direct sampling of the fuel salt and flush salt provided direct insight to solubility of the various fission products, actinides and corrosion products. These samples helped confirm what was already expected based on the knowledge of the electrochemical and neutronics calculations, but they also led to many new insights. Some of those insights were illustrated by the dual nature of niobium discussed in section 2.2.4.
2. Fuel Pump Sampling [2]. Samples were drawn from the fuel pump bowl via a long sampling tube in which a container of various configurations were lowered into the fuel pump by wire, held for a pre-determined period of time and then extracted. The containers started as open capsules, but became more sophisticated as specific needs were identified. For example, in seeking gas samples an evacuated capsule sealed with a salt plug was designed. The salt would melt inside the chamber after a given time and the gas would enter the capsule. Sometimes this capsule was given an additional outer layer that could be removed after extraction, to be sure any salt splash on the outside did not contaminate the subsequent handling and analysis. It was from this type of pump bowl sampling much was learned about the gas/liquid surface transport mechanism of noble metals discussed in section 2.2.1.
3. In-Core Stringer Samples [2]. Large channels for control rods and instrumentation were constructed in the graphite moderator. One channel, near the center

was used for sampling with a specially configured cylindrical Hastelloy-N basket that could be inserted and retracted during shutdown periods. The basket allowed flow of the salt and the location made it subject to the high neutron flux in the middle of the core. Positioned inside the basket were stringers made of graphite, which included Hastelloy-N connectors, that were used for destructive analysis. It was from the milling of these graphite stringers, the nature of gas penetration discussed in section 2.2.1 was discovered. Moreover, a direct comparison of the deposition on Hastelloy-N and on graphite was evaluated on this in-core sampling system. The general conclusions of the various levels of fouling discussed in section 2.2.3 came primarily from these samples.

4. In-situ Collimated Beam Monitoring [20]. A germanium (Ge) / lithium (Li) detector with a shielded lead collimator was used as a tool during shutdowns as well as during operations of the reactor. The utility was found primarily in monitoring the off-gas system and the heat exchanger. The collimator and detector were positioned above an access port over the shielding blocks above the reactor and was aligned using a laser to pinpoint the axis of the collimator to the specific area to be monitored. The buildup of activity around the heat exchanger baffle plates as discussed at the beginning of section 2.2 was determined primarily by this tool.
5. Direct Analysis of Reactor Components. In the shutdown periods, some direct measurements were made on components of the MSRE, but those components existed in very high radiation fields. In the months and years following the final shutdown of the MSRE reactor, destructive examination of some of the components was undertaken. These samples helped solidify the concepts of fouling discussed throughout section 2.2.

# Appendix B

## Electrochemistry in an MSR

### B.1 Gibbs Free Energy of Fluoride Salts

Reactions are energetically favored if the Gibbs free energy has a negative value. Fluorine is highly reactive (oxidizing) and all the metals in figure 2.1 will become salts in the presence of free fluorine. The value in comparing the Gibbs free energy of fluoride formation represented by figure 2.1 and discussed in section 2.2.2 is the sense of relative activity of elements with respect to each other in a fluoride salt. For example, the Gibbs free energy would suggest chromium would deplete (oxidize and corrode) at a greater rate than iron or nickel. This proved to be true in the MSRE and other experiments. Additionally, the relative activity/nobility of metals with respect to the uranium fluoride pair reflects the fouling in the MSRE. Active elements were salt-seeking (soluble) fluorides and noble elements were (less soluble) foulants [2]. The reaction equations and the methodology for making the calculations are described in section B.1.1 below, but it should be recognized that the graph provides an incomplete story. The underlying calculations assume molar standard conditions at a given temperature, which means a standard presence of both the metal and the fluorine gas. Metals and fluorine gas have very small concentrations (activities) in a salt. Deviations from standard conditions are found in the actual electrochemical potential of the salt and as a result, the behavior of those elements are affected. The discussion of the Gibbs free energy in a reactant limited condition will follow in section B.1.2.

#### B.1.1 Gibbs Free Energy of Fluoride Salt Formation Standard State

A metal "M" reacts with the elemental gas fluorine  $F_2$  in an x to y stoichiometric ratio and creates a fluoride salt  $M_xF_{2y}$ . The basic supporting (reversible) chemical and thermodynamic equations to derive the Gibbs free energy are:



$$\Delta G^\circ = -RT \ln [K] \quad \text{where} \quad K = \frac{[M_x F_{2y}]}{[M]^x [F_2]^y} \quad (\text{B.2})$$

- $\Delta G^\circ$  Equilibrium Gibbs free energy of the reaction for a given temperature [kJ/mole]. This is the value plotted in figure 2.1
- T Temperature in Kelvin [K]
- R Ideal gas constant =  $8.3144 \times 10^{-3}$  [kJ/mole-K]
- K Equilibrium constant [unitless] is the value of the reaction quotient when the reaction reaches equilibrium for a given temperature. The square brackets represent chemical activity of each constituent. For these constituents the concentration molality closely approximates the activity. For the standard conditions  $[M]=1$  and  $[F_2]=1$ .

The values of  $\Delta G^\circ$  per fluoride atom of equation B.1 at 727°C for key fission products, fuel and structural elements were calculated by using HSC Chemistry 6 Software by Outokumpu Research Oy [28]. Results of those calculations were tabulated in table B.1. Figure 2.1 of section 2.2.2 is a plot of the key elements in an MSR.

### B.1.2 Gibbs Free Energy - Reactant Limited Condition

In the conditions of the MSR, given their energetically reactive nature, fluorine and active metals are virtually completely consumed as reactants. As will be later described, the balance between the two stable fluoride salts of uranium  $UF_4$  and  $UF_3$  is key to maintaining the electrochemical potential of the salt. Adding a small amount of uranium or fluorine to the salt affects this balance or ratio between  $UF_4$  and  $UF_3$  by the energetic reactions (B.3 and B.4 below):

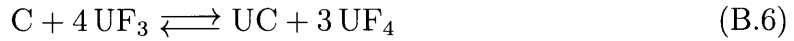


Uranium (metal) will form  $UF_3$  until the exhaustion of the metal and the ratio  $[UF_4]/[UF_3]$  will get smaller. Similarly, adding fluorine (gas) will form  $UF_4$  to the exhaustion of the fluorine, thereby increasing the  $[UF_4]/[UF_3]$  ratio.

Without the presence of fluorine or active metals, the balance reactions of the fission product in the salt has the general form:



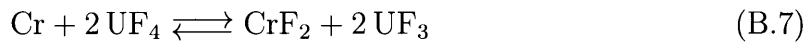
As the  $[UF_4]/[UF_3]$  ratio becomes higher, the salt becomes more oxidizing and more of metal M is corroded or turned into its salt. Conversely, the smaller the ratio, the more reducing state of the salt and equation B.5 tends to the left. It would seem then that a low ratio and a reducing environment are desirable. However, too low of a ratio (reducing conditions) promotes the undesirable creation (and precipitation) of uranium carbide (UC) [48]:



As analyzed by ORNL, the ratio of about 100 provided favorable conditions [29].

**Reactant Limiting Balance Equations** The equilibrium described by equations B.1 and B.2 are not applicable in an operating salt lacking free fluorine. In a reactant limited condition, the reversible reactions are driven by the electrochemical condition of the salt that is driven by the majority salt constituents. In this case, it is uranium fluoride. These equations are expressed similarly as equations B.7 through B.9 and are presented with an example using chromium.

The shift in valence between  $\text{U}^{+4}$  ( $\text{UF}_4$ ) and  $\text{U}^{+3}$  ( $\text{UF}_3$ ) when combined with other elements creates reduction and oxidation (redox) couples. Discussing the corrosion and mass transport of chromium serves as an illustration of the redox reaction in fouling. Chromium is a major alloying element in stainless steel and in nearly all structural materials either used or proposed in a reactor. In the nickel and nickel-molybdenum based alloys examined during the MSRE program, chromium was an ever present alloying agent that served to protect by oxidation and passivation the exposed metal surfaces which did not face the salt. Within the salt however, chromium corroded into a fluoride, and then diffused into the salt. In a clean fuel salt, free from impurities, chromium in fluoridated (oxidized) by the reduction of  $\text{UF}_4$  by the following reversible equation and its temperature related equilibrium equation:



$$\Delta G = \Delta G^\circ + RT \ln Q \quad (\text{B.8})$$

$$Q = \frac{[\text{UF}_3]^2 [\text{CrF}_2]}{[\text{UF}_4]^2 [\text{Cr}]} \quad (\text{B.9})$$

$\Delta G$  Gibbs free energy of the reaction at a given temperature [J/mole].

A greater negative number favors equation (B.7) going to the right.

$Q$  Reaction quotient [unitless]. The square brackets indicate chemical activity each constituent. For these constituents the concentration molality closely approximates the activity. As the reaction goes to the right, the value of  $Q$  becomes larger. Additions of  $\text{UF}_4$  as part of refueling, would push equation B.7 to the right by Le Chatlier's principle increasing the corrosion potential.

Note that  $K$  of equation B.2 and  $Q$  are similar. When a reaction is in equilibrium (forward rate equals the reverse rate) and is in the standard state (solid constituents have activity of one), then

$Q = K$ .

If the activity of chromium is not equal to 1, as it would be in standard conditions, then the reactant limited equilibrium equation B.9, can be rewritten as a balance of ratios:

$$\left(\frac{[\text{UF}_4]}{[\text{UF}_3]}\right)^2 Q(T) = \frac{[\text{CrF}_2]}{[\text{Cr}]} \quad (\text{B.10})$$

The values of K (Q at equilibrium) were calculated by using HSC Chemistry 6 Software [28] at 900 °C and 600 °C for chromium, iron and nickel. Using equation B.10, the metal-fluoride-to-metal ratio (for example, CrF<sub>2</sub>/Cr) is plotted versus the UF<sub>4</sub>/UF<sub>3</sub> ratio in figure 2.2 of section 2.2.2.

For chromium at 600 °C, the reaction constant is  $K = 7.0 \times 10^{-3}$ . If the ratio of UF<sub>4</sub> to UF<sub>3</sub> were 100, as was desired in the MSRE, equation B.10 makes the CrF<sub>2</sub>/Cr ratio 70. In the MSRE, total chromium concentrations were small—on the order of 60 to 90 ppm [58]. For a mid-value of approximately 71 ppm, based on the 70:1 ratio, 70 ppm would be in the form of CrF<sub>2</sub> with a 1 ppm concentration of chromium metal. If the UF<sub>4</sub>/UF<sub>3</sub> ratio were to fall substantially to a value of 1, then the CrF<sub>2</sub>/Cr ratio would drop by four orders of magnitude to  $7.0 \times 10^{-3}$ . The 70 ppm of CrF<sub>2</sub> in the salt would be electrochemically driven to its metal form and become a foulant like the noble metals of this study. These balance equations can be written for all the fission product and structural metals as well and a similar analysis can be conducted.

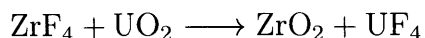
**Fission Products and Mass Transfer** The low power (8 MWth) and relatively short time (2 years) did not create significant amounts of fission products and their respective concentrations in the salt and the effects of saturation were not realized. 3.75 kg of <sup>235</sup>U consumed during the operation of the first batch would have created about 3.75 kg of fission products. The metal-fluoride (MF) to metal (M) ratio and the effects of equations (B.7 through B.9) will become more significant as fission products build. For the MSR to operate at the power and duration of a commercial power plant, the impact on solubility and recrystallization will need to be addressed.

### B.1.3 FLiBe and UF<sub>4</sub>

It might at first seem incorrect to point to UF<sub>x</sub> as the controlling element considering it comprised of only about 1 mole% in the MSRE. The main body of the salt, approximately 95 mole%, was a lithium fluoride (LiF)/beryllium fluoride (BeF<sub>2</sub>) mixture, called FLiBe.<sup>1</sup> As discussed in greater detail in appendix A, FLiBe provided the best mix of neutronic, thermo-hydraulic and chemical properties from a universe of

<sup>1</sup>The constituency of the first batch of MSRE fuel salt was made up of approximately 64 mol% lithium fluoride (LiF), 30 mol% beryllium fluoride (BeF<sub>2</sub>), 5 mol% zirconium fluoride (ZrF<sub>4</sub>) and 0.9 mol% uranium fluoride (UF<sub>4</sub>).

candidate salts. One property of FLiBe that is important in the discussion on electrochemical potentials is the nearly complete oxidation states of lithium and beryllium to their constituent fluoride salt. Lithium and beryllium are among the most active of metals and as such LiF and BeF<sub>2</sub> are among the most stable of the salts. As such, pure FLiBe will not corrode structural metals since the reduction reaction to support the oxidation of the metal is so strongly thermodynamically unfavorable. Zirconium fluoride ZrF<sub>4</sub> was added in the first batch to nearly a 5 mole% constituency to protect against forming insoluble uranium oxide by selectively forming ZrO<sub>2</sub>:



As a fluoride, ZrF<sub>4</sub> was stable in the salt and like other single valence metals participated little in the electrochemical balance of the salt. The remaining majority constituent was uranium fluoride, which because of having two closely coupled fluoride constituents (UF<sub>4</sub> and UF<sub>3</sub>), served as an adequate buffer [59].<sup>2</sup>

---

<sup>2</sup>The value 0.9 mole% was for UF<sub>4</sub> in the first batch using 32% enriched uranium fuel where 2/3 of the uranium was <sup>238</sup>U. In the second batch, undenatured (90%) <sup>233</sup>U was used as the fuel and as such UF<sub>4</sub> only comprised of 0.15 mole% of the salt [17]. The lower uranium fluoride concentrations made balancing the UF<sub>4</sub>/UF<sub>3</sub> ratio and control of the electrochemical potential difficult. In the end, the second batch experienced wider electrochemical swings and existed in a more oxidizing state than the first batch. This unintended consequence was fortunately experienced in an experimental reactor and much was learned from that issue.

**Table B.1:** Gibbs free energy of fluoride formation at 727°C (1000 K)

Element	Fluoride Salt	$\Delta G$ per mole metal [kJ/mole]	$\Delta G$ per mole F [kJ/mole]
Ruthenium	RuF <sub>5</sub>	-685.0	-137.0
Silver	AgF	-149.0	-149.0
Tellurium	TeF <sub>4</sub>	-633.8	-158.5
Palladium	PdF <sub>4</sub>	-321.5	-160.8
Rhodium	RhF <sub>2</sub>	-357.3	-178.6
Technetium	TcF <sub>3</sub>	-581.8	-193.9
Hydrogen	HF	-218.7	-218.7
Molybdenum	MoF <sub>3</sub>	-683.3	-227.8
Antimony	SbF <sub>3</sub>	-726.3	-242.1
Nickel	NiF <sub>2</sub>	-501.4	-250.7
Tin	SnF <sub>2</sub>	-535.4	-267.7
Iron	FeF <sub>2</sub>	-569.7	-284.9
Niobium	NbF <sub>5</sub>	-1471.8	-294.4
Chromium	CrF <sub>3</sub>	-933.1	-311.0
Chromium	CrF <sub>2</sub>	-649.9	-324.9
Plutonium	PuF <sub>4</sub>	-1545.1	-386.3
Zirconium	ZrF <sub>4</sub>	-1581.3	-395.3
Uranium	UF <sub>4</sub>	-1621.7	-405.4
Uranium	UF <sub>3</sub>	-1279.6	-426.5
Beryllium	BeF <sub>2</sub>	-874.1	-437.0
Europium	EuF <sub>3</sub>	-1320.9	-440.4
Promethium	PmF <sub>3</sub>	-1343.3	-447.8
Thorium	ThF <sub>4</sub>	-1799.9	-450.0
Plutonium	PuF <sub>3</sub>	-1359.2	-453.1
Rubidium	RbF	-458.2	-458.2
Cesium	CsF <sub>2</sub>	-463.4	-463.4
Potassium	KF	-466.7	-466.7
Sodium	NaF	-472.3	-472.3
Neodymium	NdF <sub>3</sub>	-1434.9	-478.3
Gadolinium	GdF <sub>3</sub>	-1450.3	-483.4
Yttrium	YF <sub>3</sub>	-1479.8	-493.3
Samarium	SmF <sub>2</sub>	1009.6	-504.8
Lithium	LiF	-520.2	-520.2
Barium	BaF <sub>2</sub>	-1046.3	-523.2
Strontium	SrF <sub>2</sub>	-1048.3	-524.1

The values of  $\Delta G^o$  were calculated by using HSC Chemistry 6 Software by Outokumpu Research Oy [28].



# Appendix C

## Decay Heat Calculations

A major energy source, known as decay heat in reactors is generated from the decay of an amalgam of radioactive materials created primarily in the fuel substrate. The major contributors to decay heat are fission products such as cesium, xenon and iodine and activated actinides such as plutonium and americium. Other sources of decay heat include the fuel itself and activation of materials used in the reactor. In general, these mechanisms are well understood—the production and losses are simply described—but not easy to calculate.

Production comes from three main sources: (a) as directly yielded from fission; (b) as a decay of an isotope that was created in one of these three prescribed ways; and (c) as a transmutation of an isotope that has absorbed a neutron. There are over 200 isotopes with significant contributions to decay heat and each has its own set of equations. The general form of the basic balance equations are the production and removal terms for an isotope  ${}^A_ZX$  with atomic weight A and number of protons Z and with N number of atoms, denoted as  $N_X$ :

$$\frac{dN_X}{dt} = \underbrace{\sum_j \sum_k \gamma_{j,k} \Sigma_{j,k}^f \phi_k}_{\text{fission}} + \underbrace{\lambda_{(X-1)} N_{(X-1)}}_{\text{decay of parent}^1} - \underbrace{\lambda_X N_X}_{\text{decay of } {}^A_ZX^2} - \underbrace{\sum_k \Sigma_k^a \phi_k}_{\text{transmutation of } {}^A_ZX} \quad (\text{C.1})$$

Note 1 There may be more than one parent isotope as will described in the fourth example below.

Note 2 There may be more than one decay mechanism, particularly for metastable isotopes.

$\frac{dN_X}{dt}$	Rate of change of isotope $N_X$ [atoms/s].
$\sum_j, \sum_k$	Fission is a function of type of fuel and energy of the neutrons. Denoting $j$ for each type of fuel and $k$ for each energy level of the neutron.
$\gamma_{j,k}$	Yield fraction of isotope $N_X$ as a function of fuel and neutron energy [unitless].
$\Sigma_{j,k}^f$	Macroscopic cross-section [cm <sup>2</sup> ] for fission (f) of fuel $j$ and neutron energy $k$ .
$\phi_k$	neutron flux of energy $k$ [neutrons/cm <sup>2</sup> -s].
$\lambda_{X-1}, \lambda_X$	decay constant of the parent (X-1) and the isotope (X) [s <sup>-1</sup> ].
$\Sigma_k^a$	Macroscopic cross-section [cm <sup>2</sup> ] for absorption (a) of isotope X that results in a transmutation into another isotope.

The complexity of interactions of all the components make calculations inordinately challenging with wide degrees of variance. The most difficult part and key for determining decay heat is to know the numbers and locations of every radioactive isotope and the neutron flux (and energy) at that location.<sup>1</sup> For an actual reactor, this would at a minimum require power history, fuel composition, structural geometry, the composition of structure and temperature profiles of every element's position in the reactor. To make an estimate of that decay heat in this appendix will be to greatly simplify the problem. It helps to look specifically at an MSR and noble metal fission products only. Actinides are exceedingly more difficult to calculate as neutron interactions of activation and fission are major factors. The following are the major simplifications made here.

1. None of the noble metals have a meaningful neutron cross sections with respect to their half-lives and ultimate yields, so burnout and activation can be ignored. A table of the half-lives and thermal neutron absorption cross sections are provided in table C.1. Of note, <sup>105</sup>Rh has a reasonably large absorption cross section, but its half-life is only 35.4 hours and its build-up is small.
2. By assuming a 100% continuous power, the differential equations are greatly simplified because the fission rate,  $\Sigma_{j,k}^f \phi_k$  is set as a constant.
3. Neutron energy is simplified to one-group. Assuming 100% continuous power already provides a constant fission rate. However, by using a simple one-group assumption, the fission yields are also constant.
4. By narrowing the time frame to daily rates over 30 years, the isotopes with half-lives that are significantly shorter than a day can be assumed to have completely decayed to the next generation and the calculations can focus on the half-lives that are in the several hours time frames or more. This substantially simplifies the chains of equations. Similarly, fission cumulative yields, which sum the total of short-lived individual precursor individual yields, use this same logic.
5. The noble metal chains are relatively straightforward beta minus decays or isomeric transitions, with few branches. Tellurium does have several metastable nuclear isomers with some having half-lives greater than their ground state isotope. To handle this challenge, the significant metastable isomers were treated as separate isotopes with their own calculations.
6. <sup>235</sup>U only. A fraction of the power builds over time from <sup>239</sup>Pu. By assuming all fissions are from <sup>235</sup>U, these fuel concentration changes are ignored.<sup>2</sup> The yield curves are nearly the same for two fuels such as <sup>235</sup>U or <sup>239</sup>Pu. However, there

---

<sup>1</sup>Further complicating matters is the probability for absorption, known as the absorption cross-section denoted by  $\Sigma_k^a$  in equation C.1 is not fully known for all energies and isotopes. Filling in the data to this incomplete, yet enormous library is an on-going focus of effort of many nuclear engineers and physicists.

<sup>2</sup>the actinides will fission also, but their contributions are far smaller and can be effectively ignored in this determination.

are some fission products such a rhodium-106 with a 0.4% yield in  $^{235}\text{U}$  and a 4.0% yield in  $^{239}\text{Pu}$ . Determining the decay heat from these isotopes would take a more involved set of calculations and it is acknowledged that the estimates provided here would be inaccurate.

7. Clean core start. Starting with a clean new core removes the uncertainties of having varying quantities of fission products already in the reactor. The assumption of zero initial levels for all fission products at the start provides a baseline for which all the resultant plots can be compared.
8. The last is a gross simplification having to do with the treatment of expended energy from decay. Nominally, some fraction of this decay energy is in the form of kinetically propelled particles such as electron/anti-neutrino pair in a beta decay, an electron in an internal conversion, or an  $\alpha$  particle (helium nucleus) as a part of an alpha decay, as well as the recoil of the decaying isotope. These charged particles interact with the surrounding matter travelling quite short distances and releasing their kinetic energy in a localized region in the form of heat. Most of the remaining energy comes as a cascade of gamma and x-rays, as the excited state of the newly formed daughter isotope transitions to lower energy states, or similarly decays. The photons travel much further before being absorbed in surrounding materials and structures and creating heat. Depending on the container and the assumptions, the charged-particle energy contributes to heat and the photon energy may escape the system entirely. For the fission products, the primary decay is beta decay. A secondary source of particle energy comes from the internal conversions (IC) of metastable isotopes. The  $\beta$  particle from beta decays and the electron from IC can have a wide range of kinetic energy and hence, the local deposited energy can run a wide range. Using the average beta decay energy for the beta decays and evaluating the range of electron energies of an IC provided in the isotope energy libraries, such as the Evaluated Nuclear Data File (ENDF), is a simplification, but provides a fair approximation.

**Simplified Differential Equations** Equation C.1 then becomes a function of fission yield of the parent and the progeny,<sup>3</sup> the decay constants of the parent and progeny, and possibly the decay constant of the grandparent. Once "N" is calculated, mass, activity, total decay heat and decay heat from  $\beta$  particles can be calculated. Some isotopes, particularly the ones with multiple decay pathways, needed additional layers of calculations.

---

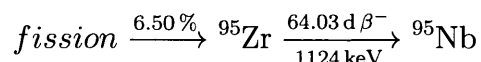
<sup>3</sup>Isotopes transmuting to other isotopes are referred to as parents and daughters. Chains involving a series of these types of pairs invoke additional generational terms such as grandparent and progeny.

## C.1 Decay Heat Calculations at Power from a Clean Core Startup

The equations and calculations for the different isotopes primarily fell into the five main decay types listed below. Example isotopes are used to aid in clarity.

### Type 1: No significant parent accumulation

Example  $^{95}\text{Zr}$ . All of  $^{95}\text{Zr}$ 's precursor isotopes have half-lives less than 11 minutes so their individual contributions to the chain can be ignored as if all of  $^{95}\text{Zr}$  was born directly from fission.  $^{95}\text{Zr}$ 's cumulative yield is 6.50%.  $^{95}\text{Zr}$  beta decays with a half-life of 64.03 days to  $^{95}\text{Nb}$ .<sup>4</sup> Total energy released ( $\Delta Q$ ) is 1123.6 keV. Mean  $\beta$  particle energy ( $\Delta Q(\beta)_{avg}$ ) is 117 keV.



$$\frac{dN_1}{dt} = \gamma_1 F - \lambda_1 N_1 \quad (\text{C.2})$$

$\frac{dN_1}{dt}$	Rate of change of isotope $N_1$ . In this example isotope 1 is $^{95}\text{Zr}$ and isotope 2 is $^{95}\text{Nb}$ [atoms/s].
$\gamma_1$	Yield fraction of isotope $N_1$ . Assumptions 3, 4 and 6: one fuel and one neutron energy [unitless].
$F$	Fission rate. Assumptions 2 and 3 simplify this to a constant.
$\lambda_0, \lambda_1$	decay constant of the parent (0) and the isotope (1) [ $\text{s}^{-1}$ ]. $^{95}\text{Zr}$ has no radioactive parent (isotope 0) (Assumption 4), so $\lambda_0$ is not applicable.
$\Sigma_k^a$	Assumption 1. No significant absorptions.
$\Delta Q$	The total energy released from the beta decay [MeV].
$\Delta Q(\beta)_{avg}$	The average energy of a $\beta$ particle from a beta decay.

- $N_1$ , **number of atoms**. The solution to equation C.2 is:

$$N_1[\text{atoms}] = \frac{\gamma_1 F (1 - e^{-\lambda_1 t})}{\lambda_1} \quad (\text{C.3})$$

---

<sup>4</sup>Another simplification is used here.  $^{95}\text{Zr}$  decays 98.8% of the time to  $^{95}\text{Nb}$  and 1.2% of the time to  $^{95m}\text{Nb}$ , which then by internal conversion (IC) decays to  $^{95}\text{Nb}$  with a half-life of 3.61 days. Because of the small fraction and the much shorter half-life of the metastable state, the simplification is to ignore the metastable form and assume all decays go directly to  $^{95}\text{Nb}$ . The total energy change is the same, however the IC energy of the ejected electron from the metastable state is typically much greater than the average  $\beta$  particle energy. In this  $^{95}\text{Nb}$  case, the fraction is negligible and the difference can be ignored. For some other isotopes, the rough value of electron energy can be obtained from the ENDF database.

- **Mass.** The mass in kg is:

$$Mass(N_1)[\text{kg}] = N_1 \times A_w \times N_{AV} \times 10^{-3} \text{ (g/kg)} \quad (\text{C.4})$$

$A_w$  Atomic weight. 94.908 For  $^{95}\text{Zr}$ .  
 $N_{AV}$  Avogadro's number  $6.02 \times 10^{23}$  [atoms/mole]

- **Activity.** Activity in Bq is  $\lambda N$ , so  $^{95}\text{Zr}$ 's activity is:

$$A_1[\text{Bq}] = (1 - e^{-\lambda_1 t}) \gamma_1 F \quad (\text{C.5})$$

Bq Becquerels where a Bq is one disintegration per second

- **Decay Heat.** Decay heat is activity times energy per decay. The total energy released per decay is  $\Delta Q$ . The local heat can be estimated from the average  $\beta$  energy per decay. The average  $\beta$  energy per decay is typically in the 10 to 30 percent range of the total energy released.

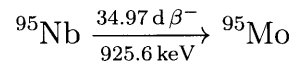
$$\text{Decay heat}[\text{kW}] = A_1 * \Delta Q * 1.602 \times 10^{-16} \text{ (kJ/MeV)} \quad (\text{C.6})$$

and

$$\text{Decay heat}(\beta)[\text{kW}] = A_1 * \Delta Q(\beta)_{avg} * 1.602 \times 10^{-16} \text{ (kJ/MeV)} \quad (\text{C.7})$$

## Type 2: Production by Parent decay $\gg$ fission product yield

Example  $^{95}\text{Nb}$ .  $^{95}\text{Nb}$  has a fission yield of  $1 \times 10^{-4}$  % and is negligible.  $^{95}\text{Nb}$  decays with a half-life of 34.97 days to  $^{95}\text{Mo}$  (stable). Total energy released ( $\Delta Q$ ) is 925.591 keV per decay. Mean  $\beta$  energy ( $\Delta Q(\beta)_{avg}$ ) is 43.43 keV.



$$\frac{dN_2}{dt} = \lambda_1 N_1 - \lambda_2 N_2 \quad (\text{C.8})$$

$\frac{dN_2}{dt}$  Rate of change of isotope  $N_2$ . In this example, isotope 1 is still  $^{95}\text{Zr}$  and isotope 2 is  $^{95}\text{Nb}$ .

$\gamma_2$  Yield fraction of isotope  $N_2$ . In this case, it is so low we can assume negligible.

$\lambda_1, \lambda_2$  decay constant of the parent (1) and the isotope (2). [1/s]

$\Sigma_k^a$  Assumption 1. No significant absorptions.

- **$N_2$ , number of atoms.** Substituting  $N_1$  from equation C.3 of the first example, the solution to equation C.8 is:

$$N_2 = \frac{\gamma_1 F}{\lambda_2} (1 - e^{-\lambda_2 t}) + \frac{\gamma_1 F}{(\lambda_2 - \lambda_1)} (e^{-\lambda_2 t} - e^{-\lambda_1 t}) \quad (\text{C.9})$$

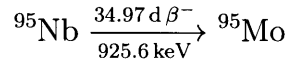
- **Mass.** The calculations for mass in kg are of the same form as Type 1 in the first example.
- **Activity.** Activity in Bq is  $\lambda N$ , so  $^{95}\text{Nb}$ 's activity is:

$$A_2 = \gamma_1 F (1 - e^{-\lambda_2 t}) + \frac{\lambda_2 \gamma_1 F}{(\lambda_2 - \lambda_1)} (e^{-\lambda_2 t} - e^{-\lambda_1 t}) \quad (\text{C.10})$$

- **Decay Heat.** Total decay heat [kW] and decay heat from  $\beta$  [kW] are calculated in the same way as example 1.

**Type 3: Production from decay of a parent with a non-trivial source term. The isotope is stable so there is no loss.**

Example  $^{95}\text{Mo}$ .  $^{95}\text{Mo}$ 's fission yield is insignificant at  $4 \times 10^{-10}$  %.  $^{95}\text{Mo}$  is stable with no decay. The basic differential equation is simple, but the  $N_p$  (parent) reaches back a generation. Mass grows without decay. Total energy released ( $\Delta Q$ ) is not applicable.



$$\frac{dN_3}{dt} = \lambda_2 N_2 \quad (\text{C.11})$$

$\frac{dN_3}{dt}$  Rate of change of isotope  $N_3$ . In this example isotope 1 is still  $^{95}\text{Zr}$  and isotope 2 is still  $^{95}\text{Nb}$ . Isotope 3 is  $^{95}\text{Mo}$ .

- **$N_3$ , number of atoms.** Substituting  $N_2$  from equation C.9 of the second example, the solution to equation C.11 is:

$$N_3 = \gamma_1 F \left[ t + \left( \frac{e^{-\lambda_2 t}}{\lambda_2} - \frac{1}{\lambda_2} \right) - \frac{1}{\lambda_1} + \frac{\lambda_2 e^{-\lambda_1 t} - \lambda_1 e^{-\lambda_2 t}}{\lambda_1 (\lambda_2 - \lambda_1)} \right] \quad (\text{C.12})$$

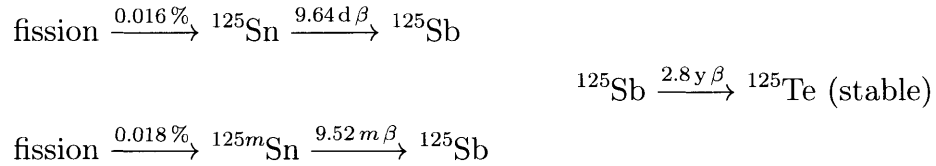
- **Mass.** The calculations for mass in kg are of the same form as Type 1.
- **Activity and Decay Heat.** Since  $^{95}\text{Mo}$  is stable, it has no activity nor decay heat contributions.

**Type 4: Production from the decay of two parents. Both parents are produced from fission.**

Example  $^{125}\text{Sb}$  antimony (Sb) from tin (Sn).  $^{125}\text{Sb}$  has an insignificant fission yield of  $2.7 \times 10^{-5} \%$ .  $^{125}\text{Sb}$  decays with a half-life of 2.8 y to  $^{125}\text{Te}$ . Total energy released ( $\Delta Q$ ) is 766.7 keV. Mean  $\beta$  energy ( $\Delta Q(\beta)_{avg}$ ) is 86.7 keV.

Production comes from  $^{125}\text{Sn}$  and  $^{125m}\text{Sn}$ . The cumulative fission product yield for  $^{125}\text{Sn}$  is 0.016% and for  $^{125m}\text{Sn}$  is 0.018%. Somewhat unusually, the metastable form decays 100% by beta decay rather than isomeric transition of many of the metastable isotopes evaluated in this study. With both forms having similar cumulative yields and both decaying by beta decay sets up a double parent situation.

The half lives are 9.64 days for  $^{125}\text{Sn}$  and 9.52 minutes for  $^{125m}\text{Sn}$ .



The differential equation for noble metal  $^{125}\text{Sb}$  is:

$$\frac{dN_3}{dt} = \lambda_a N_a + \lambda_b N_b - \lambda_3 N_3 \quad (\text{C.13})$$

The supporting equations for the tin parents a =  $^{125}\text{Sn}$  and b =  $^{125m}\text{Sn}$  are:

$$\frac{dN_a}{dt} = \gamma_a F - \lambda_1 N_a \quad (\text{C.14})$$

$$\frac{dN_b}{dt} = \gamma_b F - \lambda_1 N_b \quad (\text{C.15})$$

The solutions for the parents are similar to the  $N_1$  of type 1 above (equation C.3).

$$N_a = \frac{\gamma_a F (1 - e^{-\lambda_a t})}{\lambda_a} \quad \text{and} \quad N_b = \frac{\gamma_b F (1 - e^{-\lambda_b t})}{\lambda_b} \quad (\text{C.16})$$

$\frac{dN_3}{dt}$	Rate of change of the noble metal isotope $N_3$ . In this example, isotope 3 is $^{125}\text{Sb}$ . Parent isotope 'a' is $^{125}\text{Sn}$ and parent isotope 'b' is $^{125m}\text{Sn}$
$\gamma_a$ and $\gamma_b$	Yield fraction of isotope $N_a$ and $N_b$ .
$\lambda_a, \lambda_b$ and $\lambda_3$	Decay constants of the parent 'a', parent 'b' and isotope 3 [ $\text{s}^{-1}$ ].
$\Delta Q$	The total energy released from the noble metal beta decay [MeV].
$\Delta Q(\beta)_{avg}$	The average energy of a $\beta$ particle from the noble metal beta decay.

- **$N_3$ , number of atoms.** Substituting  $N_a$  and  $N_b$  from equation C.16, the solution to equation C.13 is:

$$N_3 = \frac{-(\gamma_a + \gamma_b)F}{\lambda_3} (1 - e^{-\lambda_3 t}) + \left( \frac{\gamma_a F}{\lambda_2 - \lambda_a} \right) (e^{-\lambda_2 t} - e^{-\lambda_a t}) + \left( \frac{\gamma_b F}{\lambda_2 - \lambda_b} \right) (e^{-\lambda_2 t} - e^{-\lambda_b t}) \quad (\text{C.17})$$

- **Mass.** The calculations for mass in kg are of the same form as Type 1 in the first example.
- **Activity.** Activity in Bq is  $\lambda N$ , so  $^{125}\text{Sb}$ 's activity is:

$$A_3 = -(\gamma_a + \gamma_b)F (1 - e^{-\lambda_3 t}) + \left( \frac{\lambda_2 \gamma_a F}{\lambda_2 - \lambda_a} \right) (e^{-\lambda_2 t} - e^{-\lambda_a t}) + \left( \frac{\lambda_2 \gamma_b F}{\lambda_2 - \lambda_b} \right) (e^{-\lambda_2 t} - e^{-\lambda_b t}) \quad (\text{C.18})$$

- **Decay Heat.** Total decay heat [kW] and decay heat from  $\beta$  [kW] are calculated for the noble metal and not the parents. The parent, tin remains in the salt.

## Type 5: Continuation of Type 4

Example  $^{125}\text{Te}$  is a stable noble metal from the decay of  $^{125}\text{Sb}$ .  $^{125}\text{Te}$  has an insignificant fission yield so there is only the parent decay term as a production.  $^{125}\text{Te}$  is isotope 4,  $^{125}\text{Sb}$  is still isotope 3. Isotope 'a' is  $^{125}\text{Sn}$  and isotope 'b' is  $^{125m}\text{Sn}$ .

$$\frac{dN_4}{dt} = \lambda_3 N_3 \quad (\text{C.19})$$

recall  $\lambda_3 N_3$  is the activity of the parent seen in equation C.18.



- $N_4$ , **number of atoms**. Integration of equation C.18 yields:

$$N_4 = (\gamma_a + \gamma_b)F \left( t + \frac{e^{-\lambda_3 t} - 1}{\lambda_3} \right) + \frac{\gamma_a F}{\lambda_a} \left( \frac{\lambda_3 e^{-\lambda_a t} - \lambda_a e^{-\lambda_3 t}}{\lambda_3 - \lambda_a} - 1 \right) + \frac{\gamma_b F}{\lambda_b} \left( \frac{\lambda_3 e^{-\lambda_b t} - \lambda_b e^{-\lambda_3 t}}{\lambda_3 - \lambda_b} - 1 \right) \quad (\text{C.20})$$

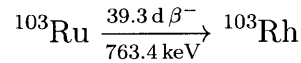
- **Mass**. The calculations for mass in kg are of the same form as in Type 1.
- **Activity and Decay Heat**. Since  $^{125}\text{Te}$  is stable, it has no activity nor decay heat contributions.

## C.2 Decay Heat Following Shutdown

Decay heat persists after the reactor is shutdown from the inventory of radioactive materials present. The calculations for decay heat following shutdown are simplified by removal of the fission source term, but are more complicated because assumption seven—a clean core and no initial fission product concentration—is no longer valid. A determination of the inventory of fission products is required in place of the clean core. For the calculations used in creating the plot of decay heat from  $\beta$  energy in figure 3.6, the initial isotope concentration values were taken from the calculations of the previous section, assuming shutdown occurs at the one year point following operations at 100% power. The shutdown decay heat equations are presented in similar fashion to the decay heat equations presented in the previous section.

**Type 1: Simple Decay** Most of the noble metal fission products were in this category.

Example  $^{103}\text{Ru}$ .  $^{103}\text{Ru}$  decays with a half-life of 39.3 days to  $^{103}\text{Rh}$  (stable). Total energy released ( $\Delta Q$ ) is 763.4 keV per decay. Mean  $\beta$  energy ( $\Delta Q(\beta)_{avg}$ ) is 63.8 keV.



$$\frac{dN_1}{dt} = -\lambda_1 N_1 \quad (\text{C.21})$$

$\frac{dN_1}{dt}$  Rate of change of isotope  $N_1$ . In this example, isotope 1 is  $^{103}\text{Ru}$ .  
 $\lambda_1$  decay constant of  $^{103}\text{Ru}$  [1/s].

- $N_1$ , **number of atoms**. The solution to equation C.21 is:

$$N_1 = B_1 e^{-\lambda_1 t} \quad (\text{C.22})$$

$B_1$  is the value of the number of  $^{103}\text{Ru}$  atoms at the time of shutdown calculated in the first section.

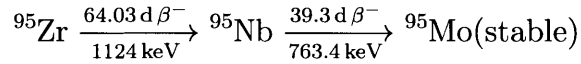
- **Activity.** Activity in Bq is  $\lambda_1 N_1$ , so  $^{103}\text{Ru}$ 's activity is:

$$A_1 = \lambda_1 B_1 e^{-\lambda_1 t} \quad (\text{C.23})$$

- **Decay Heat.** Knowing the activity, total decay heat [kW] and decay heat from  $\beta$  [kW] are calculated in the same way as in example 1 of the previous section.

## Type 2: Production by a Single Parent, Loss by Simple Decay

Example  $^{95}\text{Nb}$ .  $^{95}\text{Nb}$  is produced from the decay of the inventory of its parent  $^{95}\text{Zr}$  at the time of shutdown.  $^{95}\text{Nb}$  decays with a half-life of 39.3 days to  $^{95}\text{Mo}$  (stable). Total energy released ( $\Delta Q$ ) from  $^{95}\text{Nb}$  decay is 925.6 keV per decay. Mean  $\beta$  energy ( $\Delta Q(\beta)_{avg}$ ) is 43.3 keV. The decay energy of the parent isotope  $^{95}\text{Zr}$  is not attributable to  $^{95}\text{Nb}$ .



$$\frac{dN_1}{dt} = \lambda_0 N_0 - \lambda_1 N_1 \quad (\text{C.24})$$

$\frac{dN_1}{dt}$  Rate of change of isotope  $N_1$ . In this example, isotope 1 is  $^{95}\text{Nb}$ .  
Isotope 0 is  $^{95}\text{Zr}$

$\lambda_0, \lambda_1$  decay constants of  $^{95}\text{Zr}$  and  $^{95}\text{Nb}$  [1/s].

- $N_1$ , **number of atoms.** The solution to equation C.24 is:

$$N_1 = \left( \frac{\lambda_0 B_0}{\lambda_1 - \lambda_0} \right) (e^{-\lambda_0 t} - e^{-\lambda_1 t}) + B_1 e^{-\lambda_1 t} \quad (\text{C.25})$$

$B_0, B_1$  are the values of the numbers of  $^{95}\text{Zr}$  and  $^{95}\text{Nb}$  atoms at the time of shutdown calculated in the first section.

- **Activity.** Activity in Bq is  $\lambda_1 N_1$ , so  $^{95}\text{Nb}$ 's activity is:

$$A_1 = \left( \frac{\lambda_0 \lambda_1 B_0}{\lambda_1 - \lambda_0} \right) (e^{-\lambda_0 t} - e^{-\lambda_1 t}) + \lambda_1 B_1 e^{-\lambda_1 t} \quad (\text{C.26})$$

- **Decay Heat.** Knowing the activity, total decay heat [kW] and decay heat from  $\beta$  [kW] are calculated in the same way as in example 1 of the previous section.

### Type 3: Production by a Two Parents, Loss by Simple Decay

Example  $^{125}\text{Sb}$ .  $^{125}\text{Sb}$  is produced from the decay of the inventories of two parents  $^{125}\text{Sn}$  and  $^{125m}\text{Sn}$  at the time of shutdown.  $^{125}\text{Sb}$  decays with a half-life of 2.76 years to  $^{125}\text{Te}$  (stable). Total energy released ( $\Delta Q$ ) from  $^{125}\text{Sb}$  decay is 766.7 keV per decay. Mean  $\beta$  energy ( $\Delta Q(\beta)_{avg}$ ) is 86.7 keV. The decay energy of the parents are not attributable to  $^{125}\text{Sb}$ .



$$\frac{dN_1}{dt} = \lambda_0 A N_{0A} + \lambda_0 B N_{0B} - \lambda_1 N_1 \quad (\text{C.27})$$

$\frac{dN_1}{dt}$  Rate of change of isotope  $N_1$ . In this example, isotope 1 is  $^{125}\text{Sb}$ .  
 Isotope 0A is  $^{125}\text{Sn}$  and isotope 0B is  $^{125m}\text{Sn}$   
 $\lambda_{0A}, \lambda_{0B}, \lambda_1$  decay constants of  $^{125}\text{Sn}$ ,  $^{125m}\text{Sn}$  and  $^{125}\text{Sb}$  [1/s].

- $N_1$ , **number of atoms**. The solution to equation C.24 is similar to the type 2 case with an additional term:

$$N_1 = \left( \frac{\lambda_{0A} B_{0A}}{\lambda_1 - \lambda_{0A}} \right) (e^{-\lambda_{0A}t} - e^{-\lambda_1 t}) + \left( \frac{\lambda_{0B} B_{0B}}{\lambda_1 - \lambda_{0B}} \right) (e^{-\lambda_{0B}t} - e^{-\lambda_1 t}) + B_1 e^{-\lambda_1 t} \quad (\text{C.28})$$

$B_{0A}, B_{0B}$ , and  $B_1$  are the values of the numbers of  $^{125}\text{Sn}$ ,  $^{125m}\text{Sn}$  and  $^{125}\text{Sb}$  atoms at the time of shutdown calculated in the first section.

- **Activity**. Activity in Bq is  $\lambda_1 N_1$ , so  $^{125}\text{Sb}$ 's activity is similar to part 2 with an added term:

$$A_1 = \left( \frac{\lambda_{0A} \lambda_1 B_{0A}}{\lambda_1 - \lambda_{0A}} \right) (e^{-\lambda_{0A}t} - e^{-\lambda_1 t}) + \left( \frac{\lambda_{0B} \lambda_1 B_{0B}}{\lambda_1 - \lambda_{0B}} \right) (e^{-\lambda_{0B}t} - e^{-\lambda_1 t}) + \lambda_1 B_1 e^{-\lambda_1 t} \quad (\text{C.29})$$

- **Decay Heat**. Knowing the activity, total decay heat [kW] and decay heat from  $\beta$  [kW] are calculated in the same way as in example 1 of the previous section.

#### Type 4: Loss by Two Different Decays (Two Daughters)

Example  $^{129m}\text{Te}$ . With a half-life of 33.6 days,  $^{129m}\text{Te}$  decays: 37% by beta decay to  $^{129}\text{I}$ , 63% by isomeric transition to  $^{129}\text{Te}$ . The calculation of N and activity is the same as for Type 1. Determining decay heat and the  $\beta$  energy requires treatment of the activity twice: 37% of activity using the Q values of the beta decay and 63% of activity using the Q values for the isomeric transition. The two terms are summed for a total decay heat value and a total beta decay energy value.

### C.3 Calculations for the Mass of Fission Products

The methodology used for calculating the mass build up of a stable isotope which is born directly from fission, such as  $^{97}\text{Mo}$ , was provided in section 3.3.1. It was also shown that the stable isotopes dominate mass build up. Calculations for the stable noble metal isotopes not directly born from fission such as  $^{95}\text{Mo}$  or  $^{125}\text{Te}$  were calculated in the preceding two sections. Buildup for a radioactive isotope is a plateau based on an production and decay equilibrium.

To determine the mass buildup of other isotopes as well as the noble metals for a 1-GWe MSR as provided in table 3.1 of 3.3.1, the assumptions provided in the calculations of the previous two sections are required with two additional assumptions: (1) all the noble gases can be swept away in a few minutes; (2) non-gaseous fission products with half-lives much shorter than a year have decayed. The calculations then follow the methodology as outlined above.

**Table C.1:** Noble Metal Half-Lives and Thermal Neutron Absorption Cross Sections

Isotope	Half-life	Thermal Neutron <sup>4</sup>
		absorption cross section [barn]
<sup>93</sup> Nb <sup>1</sup>	stable	0.45
<sup>95</sup> Nb <sup>1</sup>	34.97 d	7.0
<sup>95</sup> Mo <sup>1</sup>	stable	13.1
<sup>97</sup> Mo <sup>2</sup>	stable	2.5
<sup>98</sup> Mo <sup>2</sup>	stable	0.128
<sup>99</sup> Mo <sup>1</sup>	66 h	8.0
<sup>100</sup> Mo <sup>2</sup>	stable	0.4
<sup>101</sup> Ru <sup>2</sup>	stable	3.3
<sup>102</sup> Ru <sup>2</sup>	stable	1.17
<sup>103</sup> Ru <sup>1</sup>	39.3 d	72.0
<sup>104</sup> Ru <sup>2</sup>	stable	0.31
<sup>106</sup> Ru <sup>1</sup>	1.02 y	0.2
<sup>105</sup> Rh <sup>1</sup>	35.4 h	13 000
<sup>121</sup> Sb <sup>2</sup>	stable	5.75
<sup>123</sup> Sb <sup>2</sup>	stable	42.7
<sup>125</sup> Sb <sup>1</sup>	2.76 y	1.0
<sup>126</sup> Sb <sup>1</sup>	12.4 d	5.8
<sup>127</sup> Sb <sup>3</sup>	3.84 d	
<sup>128</sup> Sb <sup>3</sup>	9.1 h	
<sup>126</sup> Te <sup>2</sup>	stable	1.04
<sup>127<sup>m</sup></sup> Te <sup>1</sup>	109 d	9.4
<sup>128</sup> Te <sup>2</sup>	stable	0.215
<sup>129<sup>m</sup></sup> Te <sup>1</sup>	33.6 d	1.1
<sup>130</sup> Te <sup>2</sup>	stable	0.29
<sup>131<sup>m</sup></sup> Te <sup>3</sup>	1.35 d	
<sup>132</sup> Te <sup>1</sup>	3.26 d	0

Note 1: From Brookhaven National Laboratory National Nuclear Data Center Evaluated Nuclear Data File (ENDF Retrieval and Plotting Website [60])

Note 2: From National Institutes of Standards (NIST) Center for Neutron Research Interactive Website [61]

Note 3: No data available

Note 4: thermal neutron energy of 0.025 eV

THIS PAGE INTENTIONALLY LEFT BLANK

# Appendix D

## Materials Under Study

### D.1 Fission Products and Structural Materials

Evaluated in this study were fission products and elements corroding from major structural materials whose electrochemical potential in the fuel salt of the MSRE gave preference to existing in its metallic form over that of its fluoride salt. In this appendix, the important properties of the elements and isotopes in support of this work is presented. The descriptions and material properties were obtained from the CRC Handbook of Chemistry and Physics [38] and from Los Alamos National Laboratory's website page titled "Periodic Table of the Elements:LANL" [62]. The key decay equations were developed using data from Brookhaven National Laboratory's Chart of the Nuclides based on the ENDF-VII database [60]

Element	Symbol & Atomic Number	Primary Isotope(s) [Atomic Mass] <sup>1</sup>		No. of Isotopes or Isomers <sup>2</sup>	
		Fission Products	Structural	Natural	Known
Niobium	Nb-41	95	93	1	48
Molybdenum	Mo-42	95,97-101	92,94-98,100	7	37
Ruthenium	Ru-44	101-104, 106	-	7	35
Rhodium	Rh-45	103,105	-	-	52
Antimony	Sb-51	121-123, 125-128	-	2	47
Tellurium	Te-52	126-132	-	8	42
Chromium	Cr-24	-	50,52,23,54	4	24
Iron	Fe-26	-	54,56,57	4	30
Nickel	Ni-28	-	58,60,61,62,64	5	30

1. From IUPAC Technical Report on Isotopic Compositions of the Elements 2013 [63]

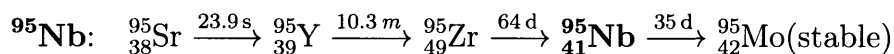
2. From CRC Handbook of Chemistry and Physics [38]

**Table D.1:** Important Isotopes of Key Fission Products and Structural Elements

### D.1.1 Niobium

Niobium exists in valence states 2, 3 and 5 and has only one naturally occurring isotope,  $^{93}\text{Nb}$  and one radioactive isotope  $^{95}\text{Nb}$  of any significant cumulative yield. Electrochemically, niobium existed in the MSRE primarily as a metal when the ratio of  $\text{UF}_4$  to  $\text{UF}_3$  was on the order of 100 or greater [2].

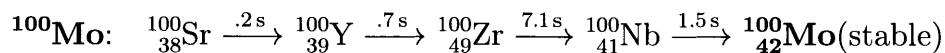
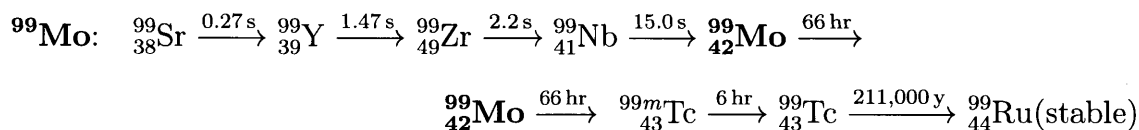
**Key Niobium Decay Chain** Zirconium (Zr), niobium (Nb), molybdenum (Mo), technetium (Tc), ruthenium (Ru), rhodium (Rh), palladium (Pd) and silver (Ag) lie in sequence on the periodic table (40 to 47) and therefore share common beta decay chains.



### D.1.2 Molybdenum

One of the most refractory of elements. With a melting point of 2623 °C, among readily available metals, only tungsten and tantalum have higher melting points. Valence states 2, 3 and 6. Rarely in valence states of 4 and 5. There are over 30 isomers/isotopes, much of which are unstable or radioactive.

#### Key and Typical Molybdenum Decay Chains

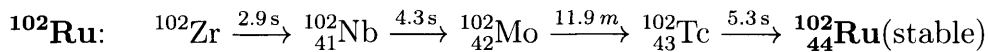
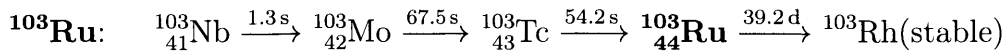


### D.1.3 Ruthenium

Ruthenium is a refractory metal that remains untarnished at normal temperatures. It has a high melting point of 2334 °C. Ruthenium exhibits valence states of 0 through 8, but as a fluoride primarily exists in valence state +5. 35 known isotopes/isomers of which seven are natural. The isotopes  $^{101}\text{Ru}$ ,  $^{101}\text{Ru}$  and  $^{101}\text{Ru}$  are stable.  $^{103}\text{Ru}$  contributes to after shutdown decay heat with a 39.2 day half-life



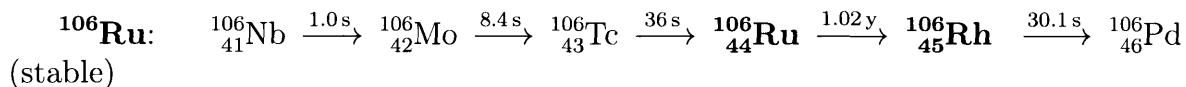
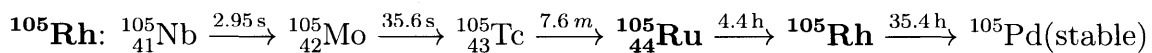
## Key and Typical Ruthenium Decay Chains



## D.1.4 Rhodium

Rhodium is one of rarest of metals. It is one of the noblest of metals and is used in high temperature applications because of its resistance to corrosion at temperature. Melting point of 1694 °C. Rhodium exists in valence states 2, 3, 4, 5 and 6; and has 52 known isotopes/isomers, of which seven are natural.

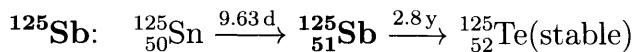
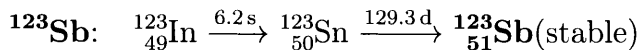
## Key and Typical Rhodium (and Ruthenium) Decay Chains



## D.1.5 Antimony (Sb)

A metal with a low melting point. At 630.6 °C, the melting point is close, if not within the operating temperature of an MSR. At room temperatures, antimony is relatively stable but will burn in air at high temperatures. Antimony exists in valence states of -3, 0, +3, +5. Two naturally occurring isotopes/isomers with 45 recognized radioactive.

**Key and Typical Antimony Decay Chains** Antimony(Sb) and tellurium (Te) are adjacent in the periodic table and share most decay chains.



## D.1.6 Tellurium - Atomic Number 52

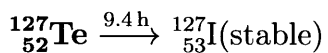
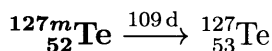
Tellurium (Te) is a silvery-white metalloid with a melting point of 449.5 °C, which is at the lower than the operating temperature of an MSR. There was some belief by chemists at ORNL that tellurium existed as gaseous elemental tellurium in the reactor [2]. Tellurium exhibits a number of different oxidation states primarily -2, +2 and +6 states. Although tellurium is considered one of the noble metals in a molten

salt reactor because it does not readily form fluorides and remains insoluble in the fluoride salt, tellurium's -2 valence state could find it potentially combining with other metals in forming stable tellurides. In combination with nickel and chromium for example, tellurium could exist as NiTe<sub>2</sub> and CrTe<sub>2</sub>. Formation of chromium and nickel tellurides is suggested as one theory for the intergranular cracking found in the MSRE. However, the actual state of tellurium as a metal, as a metal telluride or as a gas was never determined in the MSRE [18]. There are forty-two known Te isotopes ranging 106 to 138 in atomic weight of which 8 are naturally occurring. The stable fission products of interest have atomic weights of 126, 127, 128 and 130.<sup>1</sup>

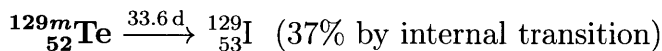
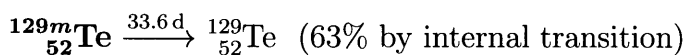
## Key and Typical Tellurium Decay Chains

While most fission products are born with a nucleus in an excited energy state and undergo gamma (or sometimes shell electron) releasing transitions toward ground state, these isomers are normally quite short-lived. Those that exist for longer than a billionth of a second are called metastable. Tellurium is somewhat odd in that many of its isotopes have metastable isomers and also rare is a number of these metastable isomers have half-lives longer than their ground-state isomer.

### <sup>127m</sup>Te and <sup>127</sup>Te



The metastable isomer primarily undergoes isomeric transition to their ground state (but some like <sup>129m</sup>Te will undergo beta decay to a daughter isotope as well):



## D.2 Material Data Sheets for Noble Metal Targets

Copies of the material data sheets for the noble metal targets (Nb, Mo, Ru, Sb and Te) are included as the last pages of this appendix.

---

<sup>1</sup>At the end of the MSRE program, stress corrosion cracking of plant materials was discovered. Investigation pointed to tellurium induced stress corrosion cracking. Recently, investigations have been conducted to overcome this problem. Although this subject is outside of this paper, the Kurchatov Institute believes they found some means of preventing this cracking [64].

## D.3 Substrate Composition

The substrate metals and alloys were all commercially procured. No special requirements were levied on our materials such as special annealing or crystal orientation. From the material data sheets:

- Incoloy 800H
  1. Source: Huntington Alloys Corporation, Huntington, WV
  2. Dated 27 Jan 2016
  3. Major: Fe-Ni-Cr (46.2/30.3/20.3)
  4. Minor/Impurities C(0.08%); Mn(0.9%) Si(0.2%) Cu (0.23%) Al(0.48%) Ti (0.48%) Co (0.2%) S(0.001%)
- F91
  1. Source: Deutsche Edelstahlwerke,
  2. Dated 15 February 2016
  3. Major: Fe-Cr-C (-/8.35/0.093)
  4. Minor/Impurities Si(0.31%); Mn(0.49%) Mo(0.87%) Cu (0.08%) Al(0.008%) P (0.013%) S(0.003%) Nb(0.062%)
- Nickel-201
  1. Source: AIT Allegheny Ludlum, Washington, PA
  2. Dated 23 Apr 2014
  3. Major: Ni (bal (min 99%))
  4. Minor/Impurities C(0.01%); Mg(0.008%) Si(0.05%) Ti (0.001%)
- Hastelloy-N
  1. Source: Haynes International
  2. Dated 17 Jun 2015
  3. Major: Ni-Mo-Cr-Fe (Bal/16.91/6.96/4.24)
  4. Minor/Impurities C(0.060%); Si(0.27%) Cu (0.06%) Al-Ti(0.28%) Ti (0.48%) Co (0.2%) S(0.001%)
- SS316L
  1. Source: NAS
  2. Dated 11/14/2014
  3. Major Fe/Cr/Ni/Mo/Mn/C (Bal/16.7135%/10.0350%/2.0315%/1.2395%/0.0256%)
  4. Minor/Impurities Cu (0.4545%/N(0.0552%), P(0.0295%), S (0.0010)

# Kurt J. Lesker<sup>™</sup> Company

1925 Route 51  
Jefferson Hills, PA 15025-3681 USA  
www.lesker.com

SALES: (800) 245-1656  
(412) 387-9200 Fax: (412) 384-2745

## Material Certification

<b>Material Type:</b> Niobium, Nb		<b>Analysis Type:</b> Typical, PPM by Wt.	
<b>Description:</b> 2.00" Diameter x .125" Thick		<b>Purity:</b> 99.95% EX Ta	
<b>KJLC Part Number:</b> EJTNBXX352A2		<b>Lot Number:</b> 15-SC-012 / VPU133031	
Ag:	Cu: <10	N: 8	Si: <10
Al:	F:	Na:	Sm:
Ar:	Fe: <10	Nb: Matrix wt%	Sn:
As:	Ga:	Ne:	Sr:
At:	Ge:	Ni: <10	Ta: 342
Au:	H: 5	O: 96	Tb:
B:	He:	Os:	Te:
Ba:	Hf:	P:	Th:
Be:	Hg:	Pb:	Ti: <10
Bi:	I:	Pd:	U:
Br:	In:	Pt:	V:
C: 30	Ir:	Re:	W: 53
Ca:	K:	Rh:	Y:
Cd:	Kr:	Rn:	Zn:
Ce:	La:	Ru:	Zr:
Cl:	Li:	S:	:
Co: <10	Mg:	Sb:	:
Cr: <10	Mn: <10	Sc:	:
Cs:	Mo: 11	Se:	:

**Materials Technician:** James McGrath

**Date:** 2/13/2015

# Kurt J. Lesker Company

1925 Route 51  
 Jefferson Hills, PA 15025-3681 USA  
 www.lesker.com

SALES: (800) 245-1656  
 (412) 387-9200 Fax: (412) 384-2745

## Material Certification

<b>Material Type:</b> Molybdenum, Mo		<b>Analysis Type:</b> Typical, PPM by Wt.	
<b>Description:</b> 2.00" Diameter x 0.250" Thick		<b>Purity:</b> 99.95%	
<b>KJLC Part Number:</b> EJTMOXX352A4		<b>Lot Number:</b> 15-SC-193-1 / VPU148005	
Ag:	Cu: <10	N: 30	Si: <30
Al: <20	F:	Na:	Sm:
Ar:	Fe: <40	Nb:	Sn:
As:	Ga:	Ne:	Sr:
At:	Ge:	Ni: <30	Ta:
Au:	H:	O: 60	Tb:
B:	He:	Os:	Te:
Ba:	Hf:	P:	Th:
Be:	Hg:	Pb: <10	Ti:
Bi:	I:	Pd:	U:
Br:	In:	Pt:	V:
C: 50	Ir:	Re:	W:
Ca: <10	K:	Rh:	Y:
Cd:	Kr:	Rn:	Zn:
Ce:	La:	Ru:	Zr:
Cl:	Li:	S:	:
Co:	Mg: <20	Sb:	:
Cr: <10	Mn: <10	Sc:	:
Cs:	Mo: Matrix wt%	Se:	:

**Materials Technician:** James McGrath

**Date:** 12/1/2015

# Kurt J. Lesker<sup>®</sup> Company

1925 Route 51  
Jefferson Hills, PA 15025-3681 USA  
www.lesker.com

SALES: (800) 245-1656  
(412) 387-9200 Fax: (412) 384-2745

## Material Certification

<b>Material Type:</b> Ruthenium, Ru		<b>Analysis Type:</b> Typical, PPM by Wt.	
<b>Description:</b> 2.00" Diameter x .125" Thick		<b>Purity:</b> 99.95%	
<b>KJLC Part Number:</b> EJTRUXX352A2		<b>Lot Number:</b> 197010/P15-0024/25 / VPU141549	
Ag:	Cu:	N:	Si: 88
Al: 13	F:	Na:	Sm:
Ar:	Fe: 32	Nb:	Sn: 9
As:	Ga:	Ne:	Sr:
At:	Ge:	Ni: 29	Ta:
Au:	H:	O:	Tb:
B: 2	He:	Os:	Te:
Ba: 2	Hf:	P:	Th:
Be:	Hg:	Pb:	Ti: 1
Bi:	I:	Pd: 3	U:
Br:	In: 3	Pt: 2	V:
C:	Ir: 56	Re:	W:
Ca: 12	K:	Rh: 51	Y:
Cd: 5	Kr:	Rn:	Zn: 2
Ce:	La:	Ru:	Zr:
Cl:	Li:	S:	:
Co:	Mg: 3	Sb:	:
Cr: 8	Mn: 1	Sc:	:
Cs:	Mo: 21	Se:	:

**Materials Technician:** Laura Philburn

**Date:** 7/28/2015

# Kurt J. Lesker<sup>™</sup> Company

1925 Route 51  
Jefferson Hills, PA 15025-3681 USA  
www.lesker.com

SALES: (800) 245-1656  
(412) 387-9200 Fax: (412) 384-2745

## Material Certification

<b>Material Type:</b> Antimony, Sb		<b>Analysis Type:</b> Typical,% by Wt.	
<b>Description:</b> 2.00" Diameter x 0.125" Thick		<b>Purity:</b> 99.999%	
<b>KJLC Part Number:</b> EJTSBXX502A2		<b>Lot Number:</b> AMX0495 / VPU142561	
Ag:	Cu:	N:	Si:
Al:	F:	Na:	Sm:
Ar:	Fe:	Nb:	Sn:
As:	Ga:	Ne:	Sr:
At:	Ge:	Ni:	Ta:
Au:	H:	O:	Tb:
B:	He:	Os:	Te:
Ba:	Hf:	P:	Th:
Be:	Hg:	Pb:	Ti:
Bi:	I:	Pd:	U:
Br:	In:	Pt:	V:
C:	Ir:	Re:	W:
Ca:	K:	Rh:	Y:
Cd:	Kr:	Rn:	Zn:
Ce:	La:	Ru:	Zr:
Cl:	Li:	S:	:
Co:	Mg:	Sb: 99.999	:
Cr:	Mn:	Sc:	:
Cs:	Mo:	Se:	:

**Materials Technician:** Brian Moninger

**Date:** 8/6/2015



MERELEX CORPORATION • 10884 WEYBURN AVE. LOS ANGELES, CA 90024  
TEL: 310-208-0551 • FAX: 310-208-0351 • EMAIL: orders@americanelements.com

**CERTIFICATE OF ANALYSIS**  
**99.9% (metals basis) Tellurium (Elemental) Sputtering Target**

**Te**

**Product Code: TE-E-03M-ST.2125**

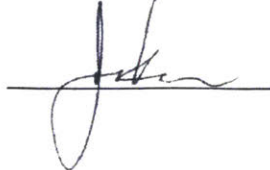
**Lot #: 1706503455-438**

**CAS #: 13494-80-9**

**Description: Diameter: 2.0"; Thickness: 0.125"**

<u>Analysis</u>	<u>ppm</u>
Cu	10
Bi	10
Mg	3
Fe	8
Al	10
S	4

AMERICAN ELEMENTS

By 



# Bibliography

- [1] GIF, *A technology roadmap for generation IV nuclear energy systems*, Dec. 2002.
- [2] E. L. Compere, S. Kirslis, E. Bohlmann, F. Blankenship, and W. Grimes, *Fission product behavior in the molten reactor experiment*, Oct. 1975.
- [3] C. W. Turner, "Implications of steam generator fouling on the degradation of material and thermal performance," in *15th International Conference on Environmental Degradation of Materials in Nuclear Power Systems-Water Reactors*, John Wiley & Sons, Inc., Jun. 26, 2012, pp. 2287–2299, ISBN: 978-1-118-45683-5.
- [4] R. Kedl, *The migration of a class of fission products (noble metals) in the molten-salt reactor experiment*, Oak Ridge, TN, 1972.
- [5] W. R. Grimes, "Molten-salt reactor chemistry," *Nuclear Technology*, vol. 8, no. 2, pp. 137–155, 1970.
- [6] J. Koger, *Evaluation of hastelloy n alloys after nine years exposure to both a molten salt fluoride salt and air at temperatures from 700 to 560 c*, Oak Ridge, TN, Dec. 1972.
- [7] J. DeVan and R. Evans, *Corrosion behavior of reactor materials in fluoride salt mixtures*, Oak Ridge, TN, Sep. 19, 1962.
- [8] W. Grimes, E. Bohlmann, and F. Blankenship, *Reactor chemistry division annual progress report for period ending may 31, 1972*, Oak Ridge, TN, Jul. 1972.
- [9] P. E. MacDonald, V. N. Shah, L. W. Ward, and P. G. Ellison, "Steam generator tube failures," *US Nuclear Regulatory Commission, Washington, DC, Report No. NUREG/CR-6365*, 1996.
- [10] C. Turner, "Fouling of nuclear steam generators: Fundamental studies, operating experience and remedial measures using chemical additives," *AECL Nuclear Review*, vol. 2, no. 1, pp. 61–88, Jun. 2013.
- [11] K. K. Satpathy, A. K. Mohanty, G. Sahu, S. Biswas, M. V. R. Prasad, and M. Sivanayagam, "Biofouling and its control in seawater cooled power plant cooling water system-a review," *Nuclear power*, pp. 191–242, 2010.
- [12] M. E. Walker, I. Safari, R. B. Therogowda, M.-K. Hsieh, J. Abbasian, H. Aras-toopour, D. A. Dzombak, and D. C. Miller, "Economic impact of condenser fouling in existing thermoelectric power plants," *Energy*, vol. 44, no. 1, pp. 429–437, Aug. 2012.

- [13] G. Lefevre, L. Zivkovic, and A. Jaubertie, "Deposition of hematite particles on alumina seal faceplates of nuclear reactor coolant pumps: Laboratory experiments and industrial feedback," *Hemijaska industrija*, vol. 66, no. 3, pp. 291–299, 2012.
- [14] H. Bindra and B. G. Jones, "Deposition of metallic colloids under sub-cooled nucleate boiling," *Colloids and Surfaces A: Physicochemical and Engineering Aspects*, vol. 397, pp. 85–91, Mar. 2012.
- [15] J. Sejvar, "Normal operating radiation levels in pressurized water reactor plants," *Nuclear Technology*, vol. 36, no. 1, pp. 48–55, 1977.
- [16] K. Sridharan and T. R. Allen, "Corrosion in molten salts," *Molten Salts Chemistry*, Elsevier, Oxford, pp. 241–267, 2013.
- [17] M. Rosenthal, R. Briggs, and P. Kasten, *Molten salt reactor program semiannual progress report for period ending february 28, 1970*, Oak Ridge, TN, Aug. 1970.
- [18] H. McCoy and B. McNabb, *Intergranular cracking of INOR-8 in the MSRE*, Oak Ridge, Tennessee, 1972.
- [19] L. F. Melo, T. R. Bott, and C. A. Bernardo, Eds., *Fouling science and technology*, Dordrecht, 1988.
- [20] Houtzeel A. and Dyer F. F., *A study of fission products in the molten-salt reactor experiment by gamma spectrometry*, Oak Ridge, TN, Aug. 1972.
- [21] R. C. Robertson, *MSRE design and operations report part i - description of reactor design*, Oak Ridge, TN, Jan. 1965.
- [22] R. Lindauer, *Processing of the MSRE flush and fuel salts*, Oak Ridge, TN, Aug. 1969.
- [23] R. Briggs, *Molten-salt reactor program semi-annual progress report for period ending july 31, 1964*, Oak Ridge, TN, Nov. 1964.
- [24] H. E. McCoy and B. McNabb, *Post irradiation examination of materials from the MSRE*, Oak Ridge, TN, Dec. 1972.
- [25] J. D. Stempian, *Tritium transport, corrosion, and fuel performance modeling in the fluoride salt-cooled high-temperature reactor (FHR)*, PhD thesis, Cambridge, MA, May 12, 2015.
- [26] B. J. Marsden, M. Haverty, W. Bodel, G. N. Hall, A. N. Jones, P. M. Mummery, and M. Treifi, "Dimensional change, irradiation creep and thermal/mechanical property changes in nuclear graphite," *International Materials Reviews*, vol. 61, no. 3, pp. 155–182, Apr. 2, 2016.
- [27] C. F. Baes, "The chemistry and thermodynamics of molten salt reactor fuels," *Journal of Nuclear Materials*, vol. 51, pp. 149–162, 1974.
- [28] A. Roine, J. Mansikka-aho, J.-P. Kentala, P. Lamberg, T. Talonen, T. Kotiranta, R. Ahlberg, A. Grohn, O. Saarinen, J. Myyri, J. Sipila, and A. Vartiainen, *HSC chemistry 6*, version 6.06, 2006.

- [29] M. Rosenthal, R. Briggs, and P. Kasten, *Molten-salt reactor program semi-annual progress report for period ending february 28, 1969*, Oak Ridge, TN, Aug. 1969.
- [30] M. Rosenthal, R. Briggs, and P. Haubenreich, *Molten-salt reactor program semi-annual progress report period ending august 31, 1971*, Oak Ridge, TN, Feb. 1972.
- [31] J. N. Israelachvili, *Intermolecular and surface forces: Revised third edition*. Academic press, 2011.
- [32] H.-J. Butt and M. Kappl, *Surface and interfacial forces*, ser. Physics textbook. Weinheim: Wiley-VCH, 2010, 421 pp., ISBN: 978-3-527-40849-8.
- [33] H. B. G. Casimir and D. Polder, "The influence of retardation on the london-van der waals forces," *Physical Review*, vol. 73, no. 4, p. 360, 1948.
- [34] H. B. G. Casimir, *Mathematics - on the attraction between two perfectly conducting plates*, Letter, May 29, 1948.
- [35] A. Lambrecht, "The casimir effect: A force from nothing," *Physics world*, vol. 15, no. 9, p. 29, 2002.
- [36] J. N. Israelachvili, "Van der waals forces between particles and surfaces," in *Intermolecular and Surface Forces*, Elsevier, 2011, pp. 253–289, ISBN: 978-0-12-375182-9.
- [37] H. Hamaker, "The london-van der waals attraction between spherical particles," *Physica*, vol. IV, no. 10, pp. 1058–1072, Nov. 23, 1937.
- [38] W. Haynes, Ed., *CRC handbook of chemistry and physics (internet version)*, Boca Raton, FL, 2017.
- [39] D. Langbein, "Van der waals attraction between macroscopic bodies," *The Journal of Adhesion*, vol. V.1, no. 4, pp. 237–245, Oct. 1969.
- [40] T. R. England and B. F. Rider, *Evaluation and compilation of fission product yields, 1993*, Los Alamos, NM, 1993.
- [41] *The future of nuclear power - an interdisciplinary MIT study*, Cambridge, 2003.
- [42] A. Nichols, D. Aldama, and M. Verpelli, *Handbook of nuclear data for safeguards: Database extension, aug 2008*, Vienna, Austria, Aug. 2008.
- [43] Brookhaven National Laboratory, *Interactive chart of nuclides*, Nov. 7, 2016.
- [44] J. A. Thornton and D. Hoffman, "Stress-related effects in thin films," *Thin Solid Films*, vol. 171, pp. 5–31, 1989.
- [45] J. Visser, "On hamaker constants: A comparison between hamaker constants and lifshitz - van der waals constants," *Advances in Colloid and Interface Science*, no. 3, pp. 331–363, 1972.
- [46] L. Bergstrom, "Hamaker constants of inorganic materials," *Advances in Colloid and Interface Science*, vol. 70, pp. 125–169, 1997.

- [47] D. B. Hough and L. R. White, “The calculation of hamaker constants from liftshitz theory with applications to wetting phenomena,” *Advances in Colloid and Interface Science*, vol. 14, no. 1, pp. 3–41, 1980.
- [48] W. Grimes, *Chemical research and development for molten salt breeder reactor*, Oak Ridge, TN, Jun. 6, 1967.
- [49] GIF, *Technology roadmap update for generation IV nuclear energy systems*, Jan. 2014.
- [50] V. M. Novikov, “The results of the investigations of russian research center, kurchatov institute, on molten salt applications to problems of nuclear energy systems,” vol. 346, AIP, 1995, pp. 138–147.
- [51] H. G. MacPherson, “The molten salt reactor adventure,” *Nuclear Science and engineering*, vol. 90, no. 4, pp. 374–380, 1985.
- [52] M. W. Rosenthal, “An account of oak ridge national laboratory’s thirteen nuclear reactors,” *ORNL/TM-2009/181*, August, 2009.
- [53] Oak Ridge National Laboratory, *Molten salt reactor experiment*, Oak Ridge National Laboratory, 2015.
- [54] W. Jordan, S. Cromer, and A. Miller, *Aircraft nuclear propulsion project quarterly progress report for the period ending september 30, 1957*, Oak Ridge, TN, Feb. 4, 1958.
- [55] J. A. Lane and H. MacPherson, Eds., *Fluid fuel reactors*, 1958.
- [56] J. H. Shaffer, *Preparation and handling of salt mixtures for the molten salt reactor experiment*, Oak Ridge, TN, Jan. 1971.
- [57] T. Ault, K. Brozek, L.-C. Fan, M. Folsom, J. Kim, and J. Zeismer, *Lithium isotope enrichment: Feasible domestic enrichment alternatives*, Berkeley, 2012.
- [58] M. Rosenthal, R. Briggs, and P. Kasten, *Molten-salt reactor program semiannual progress report for the period ending february 29, 1968*, Oak Ridge, TN, Aug. 1968.
- [59] M. Rosenthal, P. Haubenreich, and R. Briggs, *The development status of molten salt breeder reactors*, Oak Ridge, TN, Aug. 1972.
- [60] Brookhaven National Laboratory, *Evaluated nuclear data file (ENDF)*, Nov. 7, 2016.
- [61] National Institute of Standards {and} Technology, *Neutron scattering lengths and cross sections*.
- [62] Los Alamos National Laboratory, *Periodic table of elements: Los alamos national laboratory*, 2011.
- [63] J. Meija, T. B. Coplen, M. Berglund, W. A. Brand, P. De Bievre, M. Groning, N. E. Holden, J. Irrgeher, R. D. Loss, T. Walczyk, and T. Prohaska, “Atomic weights of the elements 2013 (IUPAC technical report),” *Pure and Applied Chemistry*, vol. 88, no. 3, Jan. 1, 2016.

- [64] V. V. Ignatiev, A. I. Surenkov, I. P. Gnidoi, V. I. Fedulov, V. S. Uglov, A. V. Panov, V. V. Sagaradze, V. G. Subbotin, A. D. Toropov, V. K. Afonichkin, *et al.*, “Investigation of the corrosion resistance of nickel-based alloys in fluoride melts,” *Atomic Energy*, vol. 101, no. 4, pp. 730–738, 2006.

THIS PAGE INTENTIONALLY LEFT BLANK